

## Final Project Report – Enthalpion Energy Project NV22



**Wideband MT and gravity survey of Newberry Volcano (NV), Central Oregon  
June 19, 2022 – July 20, 2022 (gravity); June 19, 2022 – July 24, 2022 (MT) for  
National Renewable Energy Laboratory,  
DEEPEN Project**

# Executive Summary

## Introduction

This report presents the results of the combined full tensor wideband<sup>1</sup> magnetotelluric (MT) survey and gravity survey acquired by Enthalpion Energy LLC (Enthalpion) and NREL staff on behalf of the National Renewable Energy Laboratory (NREL) DEEPEN Project from June 19<sup>th</sup> to July 24<sup>th</sup> 2022 at Newberry Volcano in Central Oregon. The analysis of these data sets as well as the 3-D inversion (gravity singly, MT singly, and MT and gravity jointly) is also presented here.

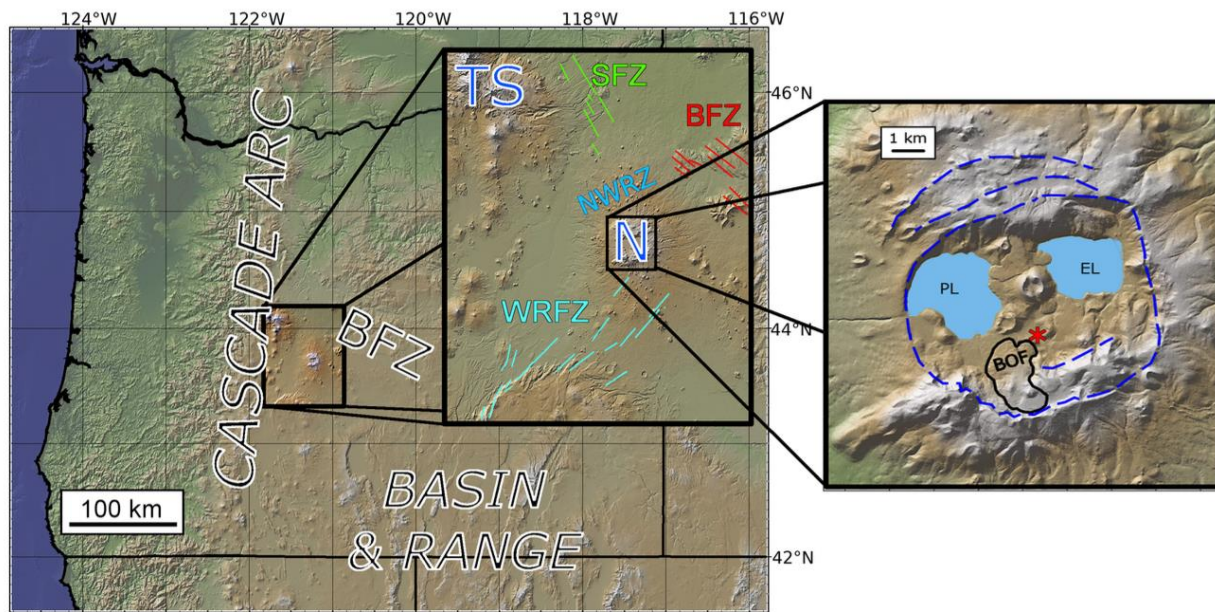


**Figure 1.** Map of Newberry's location at the intersection of major tectonic systems of the western United States. The insets show details of the caldera and Newberry's geographic relationship with nearby fault systems and the Three Sisters cluster of volcanoes in the high Cascades. Faults inferred from topography and mapping (MacLeod et al., 1995). BFZ = Brothers Fault Zone; TS = Three Sisters; SFZ = Sisters Fault Zone; WRFZ = Walker Rim Fault Zone; NWRZ = Northwest Rift Zone; N = Newberry; PL = Paulina Lake; EL = East Lake; BOF = Big Obsidian Flow. Asterisk denotes location of the 932-m-deep USGS Newberry-2 well. Dashed blue line marks caldera rim and fractures from nested collapse structures, inferred from LIDAR topography.

**Figure 1** above is reproduced from Figure 1 of Bowles-Martinez and Schultz, 2000.

A total of 43 wideband MT stations were installed and operated, with inter-station spacing of ~500 m – 2.5 km within the main array of 42 stations installed in the caldera, the south caldera rim and the south flank of the volcano, with the 43<sup>rd</sup> station located approximately 12.5 km to the northwest of Paulina Peak. The 43<sup>rd</sup> station was installed as a remote reference to be used to mitigate potential bias in the MT response functions from the influence of locally coherent magnetic field noise within the main MT station array.

<sup>1</sup> The term “wideband MT” is often referred to by other sources as “broadband MT” or BBMT. Since Enthalpion Energy LLC carries out surveys and modeling that combine multiple geophysical data sets, to avoid confusion with broadband seismic data, since that is defined for a range of frequencies (typically 0.01 Hz to > 25 Hz) that differs from that used in BBMT (typically 10 Hz to > 10 kHz), we use the term “wideband” to refer to MT data in the BBMT range, to distinguish it from the BB frequency range understood by seismologists.

A total of 102 gravity stations were acquired at the south flank of the volcano, 9 gravity stations on the northwest flank and north rim of the volcano, and 122 stations at the south caldera rim and south flank for total of 233 stations. The combined wideband MT and gravity data set is referred to in this document by its Enthalpion Job ID – **NV22**.

For inverse modeling of the resistivity and density structure of the volcano, these data were combined with legacy wideband MT data and gravity data acquired in 2012 and 2014 by Oregon State University with partners National Energy Technology Laboratory and Zonge International, as well as older legacy data released by Davenport Newberry. The legacy data were particularly dense in the west flank area of the volcano, with the new data set reported here greatly increasing the station coverage in the caldera, the south rim and south flank.

## Survey Objectives

The Enthalpion 2022 Newberry Volcano survey (NV22) was designed to improve the spatial resolving power of the subsurface electrical resistivity and density structure as determined by inversion of MT and gravity data, with particular focus on the poorly covered south caldera, south caldera rim and south flank area of the volcano. Previous work at Oregon State University (E. Bowles-Martinez and A. Schultz, 2020) indicated that there was a likely an electrically conductive target that shallowed near the Big Obsidian Flow and that extended beneath the south rim and flank area to depths that were previously associated with partial melt beneath the caldera. The association between that feature and the seismically determined sub-caldera melt body was not established, given the limitations of the existing data set. By expanding the MT and gravity station coverage in this area the conductive feature would be better localized and its significance to evaluation of the geothermal energy potential, as well as to volcanic hazards, could be better assessed. A secondary objective was to obtain additional station coverage in the northern section of the west flank of the volcano, to better delineate the northern boundary and transition to the volcano's northern rift zone of the putative pluton at depths of 3 km beneath the west rim that was previously interpreted as the core of the old volcanic center, and the source of heat for the EGS projects in that area.

<b>Enthalpion NV22 (2022) MT Array</b>	
<b>MT Station grid spacing (nominal)</b>	500-2500 m
<b>MT response frequency bandwidth</b>	440.53 Hz – 0.00067 Hz (0.002 s – 1,489.45 s)
<b>MT Digitizer resolution</b>	32-bit
<b>MT Sample rate</b>	1024 Hz (continuous)
<b>Processing</b>	Robust remote reference processing using cascade decimation and Huber Influence Function weighting following Eisel & Egbert algorithm. Remote referenced using other stations in local array.
<b>Modeling</b>	Single and joint (with gravity data) 3-D inversion of tensor impedance for the electrical resistivity structure using integral equation forward solution including topography.

<b>Enthalpion NV22 (2022) Gravity Array</b>	
<b>Gravity Station grid spacing (nominal)</b>	120-670 m typical along each loop
<b>Number of base stations</b>	7
<b>Observed range in mgal</b>	979881.444 – 980108.636
<b>Free Air Anomaly Range</b>	0.396 – 117.830
<b>Complete Bouguer Anomaly Range</b>	-143.701 – -69.288
<b>Processing</b>	Reduction to Free-Air Gravity Anomaly to correct measured gravity to what would have been measured at sea level, then reduction to Complete Bouguer Anomaly (CBA) to correct for the mass below the measurement point and above the reference mean sea level
<b>Modeling</b>	3-D inversion for density structure of bandpass filtered ( $\lambda = 1 - 35$ km for antialiasing and to remove regional trends) gravity Complete Bouguer Anomaly singly for density structure, and jointly with MT tensor impedance and tipper data for electrical resistivity structure, including topography



# Table of Contents

<i>Executive Summary</i> .....	- 2 -
Introduction .....	- 2 -
Survey Objectives .....	- 3 -
<i>Table of Contents</i> .....	- 5 -
<b>Introduction</b> .....	- 7 -
<b>Field operations</b> .....	- 10 -
<b>Instrumentation</b> .....	- 11 -
<b>Data processing</b> .....	- 15 -
<b>EDI Files and Plots</b> .....	- 22 -
<b>Augmented Survey Data Set</b> .....	- 44 -
<b>3-D inversion of MT and Gravity data</b> .....	- 45 -
<b>Resolution Analysis</b> .....	- 47 -
<b>Horizontal sections of jointly inverted models</b> .....	- 50 -
<b>Vertical sections of jointly inverted models</b> .....	- 54 -
<b>Comparison of separately and jointly inverted models</b> .....	- 58 -
<b>Fit of the jointly inverted models to the data</b> .....	- 61 -
<b>Comparison between jointly inverted models and seismic tomographic Vp model</b> .....	- 82 -
<b>Comparison between jointly inverted models and the surface geologic map</b> .....	- 86 -
<b>Comments on the south rim and flank anomaly and nearby well data</b> .....	- 90 -
<b>Folder Structure of Electronic Data Release Final Product</b> .....	- 94 -
<b>Cloud Access to Final Electronic Data Release</b> .....	- 97 -
<b>Archival Binary Data Available Upon Request</b> .....	- 98 -
<b>References</b> .....	- 99 -
<b>Conclusion and Acknowledgements</b> .....	- 101 -

**Enthalpion Project ID:** NV22

**Survey Name:** Newberry Volcano Wideband MT and Gravity 2022

**Survey Location:** Newberry Volcano, nr. Bend, in Deschutes County nr the intersection with Lake and Klamath Counties, Central Oregon

**Field Mobilization:** 6-18-2022

**Field Operations:** 6-19-2022 to 7-24-2022

**Demobilization:** 7-26-2022

**Survey Methods:** Wideband Full Tensor Magnetotelluric, Gravimetric

**Processing:** RRRMT - Robust Remote Reference; Reduction of gravity data to complete Bouger Anomaly (CBA), removal of regional gravity signature.

**Analysis:** 3-D MT and gravity inversion, each data set singly, and both jointly.

**Client:** National Renewable Energy Laboratory

**Client Address:** 15013 Denver West Parkway, Golden, CO 80401

**Client Representative:** Todd Labosky/CC Amanda Kolker

**Report Contents:** Comprehensive final project report

## Introduction

This report presents the results of the full tensor wideband magnetotelluric (MT) survey and gravity survey acquired by Enthalpion Energy LLC (Enthalpion) and NREL for the DEEPEN Project from June 20<sup>th</sup> to July 24<sup>th</sup> 2022 over an ~86 km<sup>2</sup> area encompassing the caldera and south caldera rim, south flank and a small area in the northwest flank of Newberry Volcano, Central Oregon.

43 wideband MT stations were occupied within this footprint on a nominal ~0.5 – 2.5 km spaced station grid. These stations were designated by station IDs NV22001, NV22002, ..., NV22059. 233 gravity stations were completed during the survey, with 102 gravity stations at the south flank, 9 gravity stations on the northwest flank and north caldera rim, and 118 stations at the south caldera rim and south flank.

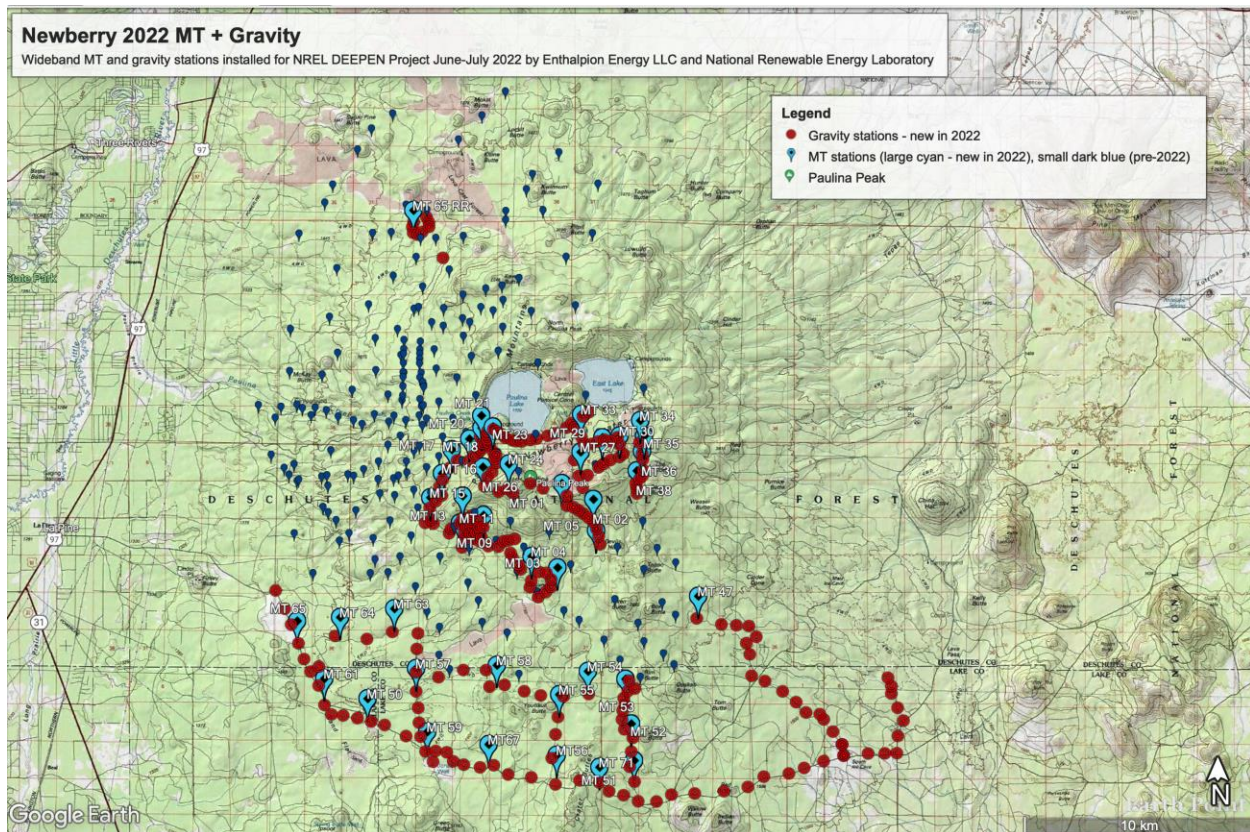


**Figure 2.** NV22 gravity (red markers) and wideband MT array (light blue markers) deployed by Enthalpion Energy LLC and NREL in June-July 2022 with locations overlaid on topography. Locations of wideband MT stations from legacy data sets included in the analysis and modeling within this project are shown with dark blue markers.

This combined data set is referred to in this document by its Enthalpion Job ID – NV22. The final deployment locations seen in Figure 1 represent a subset of stations originally planned in part because of the impact of an outbreak of COVID-19 that halted field operations for 8 of the



34 days allocated to field operations. The final and planned station distribution is summarized as follows (actually installed, originally planned):

	<b>Gravity Stations</b>	<b>Wideband MT stations</b>
• South rim	(122 of 131 gravity stations)	(25 of 35 MT stations)
• South flank	(102 of 118 gravity stations)	(17 of 28 MT stations)
• North Rim	(9 of 90 gravity stations)	(1 remote reference of 7 MT stations)
<b>TOTAL</b>	<b>(233 of 339 gravity stations)</b>	<b>(43 of 70 wideband MT stations)</b>
	(66% of original total target)	(61% of original total target)
	(90% of original south polygon)	(67% of original south polygon)

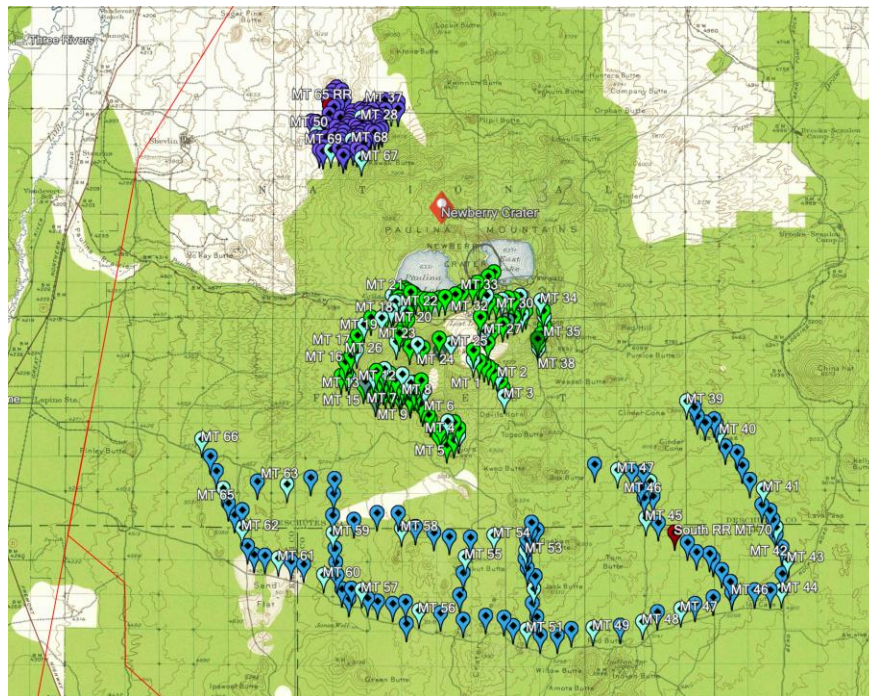


**Figure 3.** Originally planned gravity stations (dark blue symbols) and wideband MT stations (light blue symbols).

A comparison between Figures 2 and 3 shows that good spatial coverage of the southern polygon area (the south caldera, south caldera rim and south flank) was achieved, some gravity coverage in the northwest flank as well as a single MT station was operated in that area, but additional station installations in the area surrounding that MT station were not possible because of the COVID-19 impact on field operations. Operations in that area were further complicated by the poor state of the Forest Service roads along the northwest flank region making truck access difficult-to-impossible. Despite these factors, by focusing our energies on achieving good coverage in the primary southern target areas, we met the primary goal of the field operations.

The lone wideband station in the northwest flank of the volcano, station NV0065 was powered by a combination of batteries and solar panels since it was intended for continuous operation for the duration of the survey period, whereas all other MT stations were powered by 80 Ah lithium-



polymer batteries sufficient for planned run times of ~2-days per station. NV0065 was designed to serve as a remote reference station, sampling the electric and magnetic fields at 1024 samples per second continuously. After several checks on the station showing normal operations, when the station was extracted, the final run collected only 4 days of data before the run terminated prematurely. Fortunately, our survey strategy for the south flank was to install pairs of stations to operate concurrently and separated by the greatest possible distance, each to provide a fallback remote reference for the other stations in the event the northwest flank remote reference station experienced a data drop-out.

For final remote reference processing of the MT data sets, we took advantage of this approach and used the most advantageous station pairs for any given data segment to use for remote reference processing. Each wideband station in the array was paired with another station operating concurrently (either station NV0065, or another concurrently operating station in the array). The paired station provided a remote reference to mitigate the effects on the MT responses in the main part of the array due to incoherent noise in the magnetic field from noise sources local to each MT station. Such incoherent noise sources become most significant in the long-period MT dead band ( $0.1 \text{ Hz} < f < 10 \text{ Hz}$ ) where natural signal levels are low.

For gravimetric measurements long-term base stations were established, designated B1 and B2, and since the distances across the survey array prevented returning to the long-term bases within the required time window in many instances, 5 daily base stations augmented the long-term stations. The daily stations were periodically tied back to the long-term stations to provide a set of closed loops with B1 and B2. The base station locations were:

Base Station ID	Longitude (°E)	Latitude (°N)
B1	-121.273536	43.70971
B2	-121.235453	43.706411
50 – Base for southwest rim	-121.298671	43.689872
145	-121.288916	43.671875
161	-121.262059	43.660785
347	-121.298946	43.774985
210	-121.302624	43.583993

Sets of three gravity measurements were taken at designated base stations within a 2-minute window, then the process was repeated at as many additional survey locations as possible in a path that looped back to the base station for a set of repeat measurements, with the loop to be closed nominally within a time window of 3-hours or less. The seven base stations identified above were distributed to enable the station distribution indicated in Figure 1 to be achieved with optimal use of field crew time.

## Field operations

Field operations for the NV22 survey were the combined efforts of Enthalpion personnel and its contractors from Oregon State University (OSU) and Geosciences Consulting (GC), and NREL personnel. Those participating in NV22 were:

Name	Affiliation	Role
Adam Schultz	Enthalpion Energy LLC	Primary contractor, field operations and data analysis oversight
Amanda Kolker	NREL	NREL DEEPEN PI, Project lead, field operations participant
Alain Bonneville	Enthalpion sub via GC	Gravity field ops and initial data analysis lead
Esteban Bowles-Martinez	Enthalpion via OSU services	MT crew chief, field ops
Xiaolei Tu	Enthalpion via OSU services	Final gravity analysis lead, MT, Gravity field ops; single/joint inversion of MT/gravity data
Taylor Viti	Enthalpion via OSU services	MT/gravity field ops
Hannah Pauling	NREL	MT/gravity field ops; data/model assimilation
Rachel King	NREL intern	MT/gravity field ops

Enthalpion’s typical operational cadence for wideband MT is for each 2-4 person field crew to install 2-3 full tensor plus tipper (2 electric and 3 magnetic field component) wideband MT stations per day and once the initial set of stations is installed, to extract 2-3 stations per day, leaving each station to run (nominally) for 2-days. We established our 2-day cadence for wideband MT as beneficial to achieving high data quality given the variable signal and noise levels seen in the wideband MT spectrum. This is particularly important in areas known to have high noise levels due to power lines, generators, and pumps. For NV22 where gravity and MT survey operations were underway concurrently, we separated into two field crews, one dedicated to wideband MT and the other to gravity measurements. Each crew was transported in a 4x4 pickup truck with locking canopy. Crew members rotated between the two survey parties with each group led by a designated crew chief.

Parts of the NV22 survey arrays were situated within the footprint of the Newberry National Volcanic Monument, an area closed to geophysical exploration and geothermal development for several decades. Enthalpion Energy LLC worked with the Deschutes National Forest, Fort Rock District to secure a “Nominal Effects” letter pursuant to Title 36 of the Code of Federal Regulations, Subpart B, 251.50 (e) which provided the legal basis for the survey to proceed

without the requirement for a special use permit, valid through the end of August 2022. This was made possible by employing the subaerial method of MT deployment, a method developed by Adam Schultz at Oregon State University that arose from discussions with induction coil manufacturer John Saarloos of Geotell, Inc. to enable access to protected sites by eliminating the need to dig holes and trenches to install the MT sensors and equipment. This method is described in the next section of this report.

MT instrumentation and related survey equipment was loaded on two survey vehicles (a  $\frac{3}{4}$  ton long-bed 4x4 diesel pickup truck with canopy for MT and a  $\frac{1}{2}$  ton 4x4 diesel pickup truck with canopy for gravity) in Corvallis, Oregon and arrived at the NV22 survey operations base, a leased residential property in Bend, OR on June 19, 2022. Gravimetric equipment was loaded in Richland, Washington and arrived in La Pine, Oregon on the same day. The crews assembled near La Pine the following morning, all were briefed on safety, field procedures and policies, and on the gravity measurement operations, and an initial base station and measurements were taken. Parallel gravity and MT operations commenced at that point.

Parallel MT and gravity operations continued until 7/20/22 when gravity measurements completed. MT field operations continued until 7/24/22 after which the crew demobilized and returned equipment to the instrumentation depot in Corvallis, Oregon.

## Instrumentation

**MT Receivers:** Six wideband MT systems, leased from the National Geoelectromagnetic Facility at OSU, were installed at the NV22 stations. The data were sampled using 32-bit analog-to-digital (ADC) converters, with a separate ADC dedicated to each sensor channel. The MT data were digitized at a continuous sampling rate of 1,024 Hz for the duration of the station occupations. The use of such high-resolution digitizers (nominally providing 27 noise-free bits of data at 1 Hz) is useful for scenarios where higher levels of in-band electromagnetic noise is expected.

**Magnetic Field Sensors:** A total of 18 wideband induction coil sensors were leased from the National Geoelectromagnetic Facility at Oregon State University for this survey. The response calibration factors obtained for each coil (see Figure 4 for characteristic calibration curves) were applied to the magnetic field data in the data processing steps.

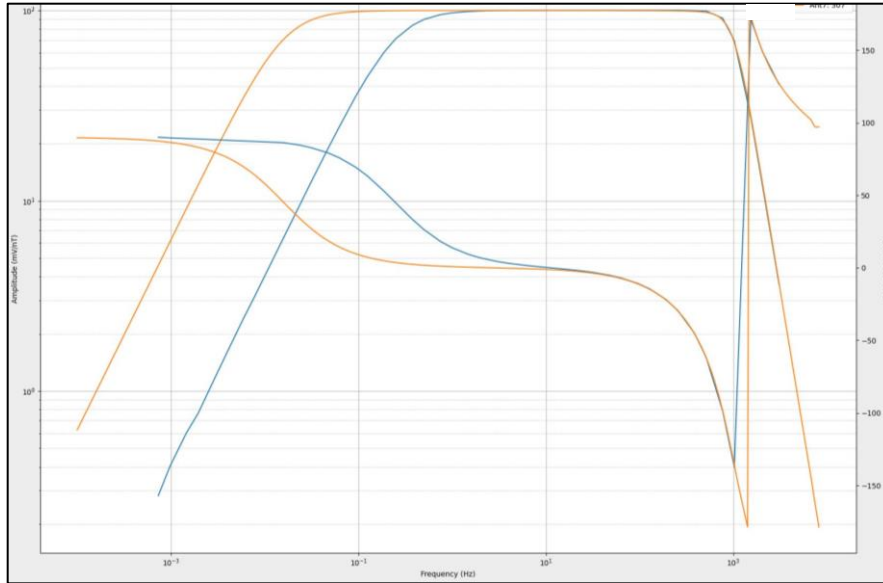


**Figure 4.** Comparison of amplitude and phase response of two models of wideband induction coil sensors. The amplitude and phase response curves for the induction coil sensors used in this survey are shown in blue (the yellow curves are for spare sensors that were not used). The sensors we deployed provide a usable frequency bandwidth from well below 1 mHz to approximately 1 kHz, which exceeds the requirements for high-resolution investigations of the electrical resistivity target features identified for NV22.

Three induction coil sensors were installed at each site, with the coils arranged in a mutually orthogonal configuration. For the tradition method of MT, measurements would be taken in the local geomagnetic coordinate reference frame, with the magnetic  $B_x$ -channel pointing from geomagnetic south to north, the  $B_y$ -channel from geomagnetic west to east, and the  $B_z$ -channel oriented vertically down in the classical geomagnetic right-handed coordinate system. This configuration requires a vertical hole to be augered more than 1-m into the ground to support the vertical magnetic field sensor, and two shallow trenches are required, one pointing geomagnetic north-south, the other east-west, for emplacement of the two horizontal magnetic field sensors. These three sensors provide the full vector magnetic field.

As indicated previously, to be granted access to station locations within the national volcanic monument we used the subaerial method of installation to eliminate the need to dig holes or trenches. In this configuration rather than installing two horizontal and one vertical sensor, the three induction coil sensors are clamped together in a mutually orthogonal configuration at their respective centers of gravity using a non-magnetic clamp. This is illustrated in Figure 5 below.





**Figure 5.** Three wideband induction coil sensors (white tubes approx. 40-in long) are clamped together and placed on the ground as seen on the left-hand side of the photo. A data acquisition system is located ~5m away (shown here surrounded by crew members on the right-hand side of the photo), powered by a lithium polymer battery pack (green Pelican™-style case) shown in the right foreground. A gravity reading is being taken in the left background of the photo.

The clamped induction coils are placed on the ground so that one designated coil is oriented to point to geomagnetic north and the inclination of each of the three coils is measured. Given this information, during data processing the three orthogonal vector components of the magnetic field measurements are mathematically rotated into conventional cardinal geomagnetic  $x=N-S$ ,  $y=E-W$ ,  $z=vertical\ down$  components.

**Electric field sensors:** A crossed dipole array configuration was used, with pairs of grounded electrodes nominally separated by 100-m. Four non-polarizing dual chamber Petiau-style Pb-PbCl<sub>2</sub> gel electrodes were located at the distal ends of the dipoles. One dipole, the  $E_x$  channel, was oriented to local geomagnetic north and the other dipole, the  $E_y$  channel, was oriented to geomagnetic east. The electric field dipole coordinates were maintained to an azimuthal tolerance of  $\pm \frac{1}{2}$  degree and a dipole length tolerance of  $\pm 1$ -m.

Electric field measurements are taken by measuring the potential differences (voltages) between matched pairs of non-polarizing Pb-PbCl<sub>2</sub> electrodes. Rather than being buried in shallow holes to achieve good ground contact with the earth as is done conventionally, for the subaerial configuration the electrodes are installed in burlap sacks filled with wet bentonite. After dampening the ground, these are placed directly on the ground, covered with a plastic tub and a tarp to retain moisture and to minimize the thermal impacts of direct sun exposure that can lead to sensor drift.

By adopting the subaerial method, wideband MT operations have been carried out by Dr. Schultz and his colleagues at Newberry National Volcanic Monument, within Yellowstone National Park caldera, and at Mount Saint Helens National Monument in areas where conventional MT

installations would not have been permitted. The NV22 survey gravity stations were included in the waiver of permitting requirements, and MT and gravity stations were collocated, with the smaller number of MT stations installed at a subset of the larger set of gravity station locations.

There is an impact on signal quality to consider when employing the subaerial MT configuration. One must be mindful of vibrations of the sensors from wind, and in areas with strong winds the coils may be sheltered inside of non-magnetic tents (although this was not generally done for NV22). There is also greater thermal variability (both diurnal variations as well as short-term variations due to varying cloud cover) that can impact electric field measurements and to a lesser extent magnetic field measurements, and ground contact can be poorer in some circumstances than for a conventional installation, potentially increasing noise in the electric field dipole sensors. The consequence of this is a usually modest degradation in signal-to-noise ratio, but we have found this to be a secondary concern for surveys that otherwise would be impossible to permit (as is the case for most of the NV22 station locations), or that would be badly compromised by degraded station sampling had the subaerial method not been available.

Five MT sensors channels were recorded at each location, the channel numbers corresponding to the different field components as follows:

CH1	-	$E_x$
CH2	-	$E_y$
CH4	-	$H_x$
CH5	-	$H_y$
CH6	-	$H_z$

**Gravimeter:** A Lacoste and Romberg Model D gravimeter provided by Pacific Northwest National Laboratory was used for gravity measurements. Gravity measurements were taken at base stations and acquired at successive station locations in a path that defined loops that ended back at the base station within a set time window (generally 3-hours or less). This is an essential part of gravimetric drift removal due to effects such as earth tides. Multiple base stations are also tied through the looping procedure. Each measurement was usually repeated 3 times at each station within a 2-minute window as a check on consistency and to identify and remove outliers.

## Data processing

**Processing methodology and derived data products for MT:** Exploratory data analysis was carried out employing robust single station as well as robust remote reference processing. Inconsistencies in results from some stations were traced to how the magnetic field sensor data measured in rotated, non-horizontal/non-vertical subaerial coordinates were rotated into conventional x,y,z coordinates using field-logged orientation metadata, and an improved algorithm was developed and cross-checked. For final production processing, after rotating the magnetic field into x=north, y=east, z=vertical down cardinal coordinates, statistically robust remote reference processing using paired wideband MT stations as the remote reference was used to produce the MT response data that is provided to NREL in EDI format. The MT response data includes full tensor impedances ( $\mathbf{Z}$ ) and induction vectors, i.e. tippers ( $\mathbf{T}$ ):

$$\begin{bmatrix} E_x \\ E_y \end{bmatrix} = \begin{bmatrix} Z_{xx} & Z_{xy} \\ Z_{yx} & Z_{yy} \end{bmatrix} \begin{bmatrix} H_x \\ H_y \end{bmatrix} + U_E, \quad (1.1)$$

$$H_z = [H_x \quad H_y] \begin{bmatrix} T_x \\ T_y \end{bmatrix} + U_{H_z}, \quad (1.2)$$

where  $U$  represents incoherent noise (the subscript indicating if the noise is taken to be in the electric ( $E$ ) field vector in the case of the impedance estimate, or in the vertical magnetic field ( $H_z$ ) in the case of the tipper estimate), and the elements of the electric ( $E$ ) and magnetic ( $H$ ) field components as well as the impedance ( $Z$ ) and tipper ( $T$ ) are taken to be in the frequency domain, with each frequency representing a band centered on a given frequency and where the impedance and tipper estimates are derived by robustly averaging Fourier spectral auto- and cross-powers over a number of frequencies adjacent to the central frequencies, and over a number of independent estimates of the cross-powers at each frequency obtained from subdivisions of the original time series derived from moving, optimally tapered time windows. The robust Huber-weighted, cascade decimation approach of Eisel and Egbert (2001) was adopted and modified to implement signal processing for NV22.

In addition to the impedance and tipper data contained in the EDI files from NV22, phase tensors were plotted during the inversion process. The MT phase tensor is written as:

$$\Phi = Re(\mathbf{Z})^{-1}Im(\mathbf{Z}) = \begin{bmatrix} \Phi_{xx} & \Phi_{xy} \\ \Phi_{yx} & \Phi_{yy} \end{bmatrix}, \quad (2)$$

where  $Re$  and  $Im$  are the real and imaginary components, respectively, of the complex-valued impedance tensor  $\mathbf{Z}$ . The ellipticity ( $\Phi_{max}$  and  $\Phi_{min}$ ) of the phase tensor and its skew angle ( $\beta$ ) are invariant parameters, insensitive to near-surface (galvanic) distortion effects, that can be used to determine the dimensionality of the regional impedance tensor as well as the direction of

geoelectric strike (it is exists<sup>2</sup>). Parameters  $\alpha$  and  $\beta$  are calculated from the phase tensor elements:

$$\alpha = \frac{1}{2} \arctan \left( \frac{\Phi_{xy} + \Phi_{yx}}{\Phi_{xx} - \Phi_{yy}} \right), \quad (3)$$

$$\beta = \frac{1}{2} \arctan \left( \frac{\Phi_{xy} - \Phi_{yx}}{\Phi_{xx} + \Phi_{yy}} \right). \quad (4)$$

If the regional resistivity structure is 1-D,  $\Phi_{\max} = \Phi_{\min}$  (i.e. a defining a circle rather than an ellipse), and if the regional structure is 2-D,  $\Phi_{\max} \neq \Phi_{\min}$ ,  $\beta=0$  and  $\alpha$  is the azimuthal angle of the major axis of the phase tensor ellipse. The geoelectric strike direction (defined for 2-D structures) is the azimuthal angle  $\alpha-\beta$  (with  $90^\circ$  ambiguity that is usually resolved by reference to the tipper strike).

**Signal bias and frequency selection for inversion:** The raw MT response data was centered on 51 frequency bands from 440.53 Hz to 0.00043Hz (period bands centered from 0.002 s to 2,340.57 s). During processing 60 Hz powerline noise was identified and removed to the greatest extent possible through zero-phase high quality factor notch filtering. Additionally, deviations from the MT source signal plane wave assumption underlying natural source MT data processing, due to Schumann Resonances in the ionospheric waveguide near 8-9 Hz, can appear in some data, although such effects are not a significant issue in the NV22 data set.

Stations in the NV22 array are located between 9 and 33 km from high voltage AC electric power transmission lines to the west running roughly parallel to US Hwy 97 through La Pine, Oregon, and the NV22 stations are located approximately 25 to 45 km from the high voltage DC power transmission line to the east that runs from the Columbia River to the north, down to Southern California (see Figure 5 below).

---

<sup>2</sup> A regional strike direction is undefined for 1-D and 3-D data. Data from the NV22 sites generally shows significantly 3-D structural effects based on phase tensor analysis, reinforced by examination of tipper vectors and diagonal elements of the impedance tensor.



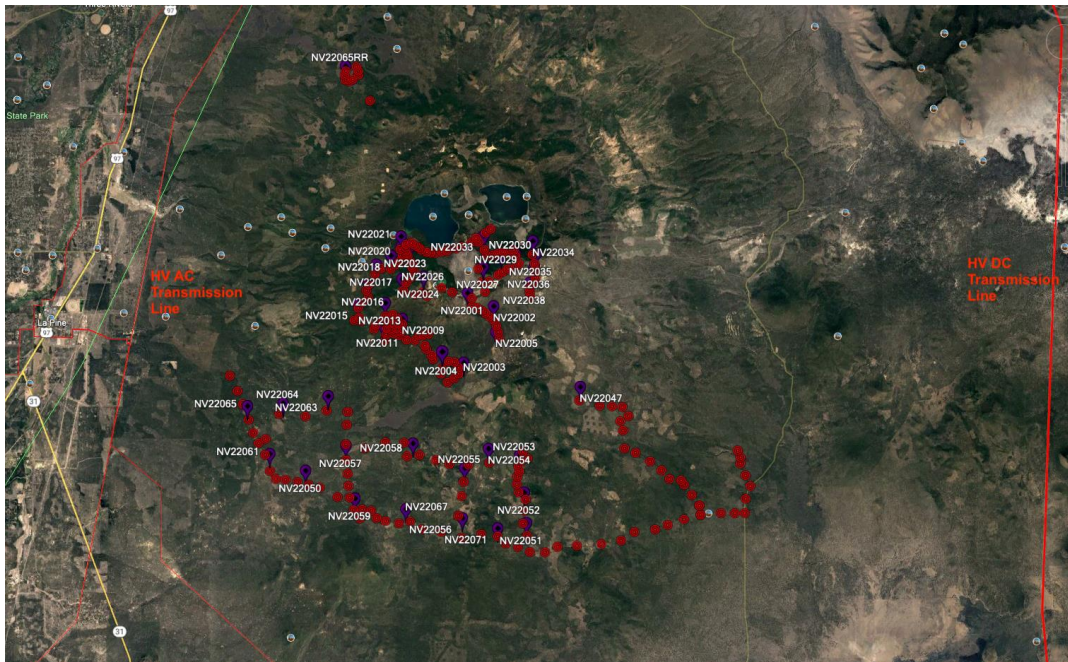


**Figure 6.** NV22 wideband MT stations marked in purple, gravity stations in red, and high-voltage electric power transmissions lines shown as red lines to the east and west of NV22.

High-voltage transmission line bias due to geomagnetically induced currents in the grounded transmission lines, as distinct from the 60 Hz powerline fundamental frequency mentioned previously, can be particularly evident in the “long-period MT dead-band” from approximately 0.1 Hz to 10Hz, where natural MT signal levels are low. In the dead-band, the signal detected at a given site from the geomagnetically induced currents in the transmission lines can dominate over the actual MT signal – i.e. the signals induced in the resistivity structure below ground. Unlike most locally generated electromagnetic noise such as magnetic and or electric field noise from power distribution lines, pumps, electric fences, electrical/electronic appliances and devices associated with residential areas etc. that is incoherent with the MT signal at distances of tens of km (the basis of remote reference processing), geomagnetically induced currents in the grounded high-voltage transmission lines may be coherent across the scale length of the MT array if the transmission lines are sufficiently close.

This poses challenges to removal of this bias since it typically defeats MT remote reference processing algorithms if remote reference data from stations within the footprint of strong powerline signals are used. This has been an issue at survey locations in the Great Basin where high-voltage AC and DC transmission lines are in close proximity to MT survey arrays. In such cases we have employed multiple remote reference stations hundreds of km from the MT array to remove the biasing effects of transmission lines since the transmission line signals are attenuated at such distances.

For the NV22 data set, at tens of km we are a reasonable distance from the transmission lines, but not so far that all bias due to geomagnetically induced currents in those lines can necessarily be ignored. This may be particularly true for the subaerial mode of MT we’ve used here which has a somewhat lower signal-to-noise ratio in the long-period dead-band.

Fortunately, there are characteristics of geomagnetically induced transmission line signals that make it possible to identify and mitigate this bias. Transmission line bias leads to a zero-phase lag between the electric and magnetic fields across a wide frequency band at each MT station. This is atypical of most MT data, and it leads to an also atypical flat 45° slope in the  $\log_{10}(\text{apparent resistivity})$  vs  $\text{Log}_{10}(\text{period})$  curves within the impacted frequency band. The width of the frequency band impacted by transmission line bias shrinks with distance from the transmission line, with the rate of attenuation depending on the elevation of the line above the ground as well as the electrical resistivity structure below ground. These characteristics make it possible to detect the signature of this source of signal bias, and to use a more distant remote reference station to mitigate it effectively, since at distances of many hundreds of km the magnetic fields induced by transmission line currents become incoherent with those measured in the MT array.

Examination of the processed MT responses for NV22 show little evidence of systematic transmission line bias; rather we see at many stations the effects of low signal levels within the long-period dead-band (discussed below), as well as the impacts of unidentified noise sources, but these are not attributed to transmission line effects.

At some stations data quality remained high through the entire frequency band, while at other stations data quality was adversely impacted by noise to varying degrees particularly within the “long-period MT dead-band” between 0.1 – 10 Hz where natural MT signal levels are very low. We expected to see larger confidence limits and rougher response functions in the dead-band when using the subaerial configuration. The signal-to-noise ratio decreases in the dead-band are sometimes limited to only one of the two principal impedance tensor elements, i.e.  $Z_{xy}$  or  $Z_{yx}$ , while at other stations such effects are seen across both elements. Plots of the MT responses described above appear in a later of this report (scaled into apparent resistivity and phase, as well as induction vectors and phase tensors) and a summary of the data quality as evidenced in the apparent resistivity and phases for the two principal elements of the impedance tensor is found in the table below.

Station ID	Data quality high across all frequencies	Data quality high outside of dead band	Data quality high except at indicated periods	Comments
NV22001	X			
NV22002		X		Zxy most impacted
NV22003	X			
NV22004		X		Zxy most impacted
NV22005			X	T > 300 s
NV22009		X		Only Zyx impacted
NV22011		X		Minor impact only on Zyx
NV22013		X		Impact mainly on Zyx
NV22015	X			
NV22016	X			
NV22017	X			
NV22018				
NV22020		X		
NV22021		X		Zyx mainly impacted

NV22023	X			
NV22024	X			
NV22026			X	T<100 s for Zxy, no impact on Zyx
NV22028		X		Only Zyx impacted
NV22029		X		
NV22030		X		Zxy mainly impacted
NV22031		X		Zyx mainly impacted
NV22034		X		Zyx mainly impacted
NV22035		X		Zyx mainly impacted
NV22036	X			
NV22038		X		Zyx mainly impacted
NV22047	X			
NV22050		X		
NV22051		X		
NV22052		X		Zyx mainly impacted
NV22054	X			Slightly noisy in deadband
NV22055		X		
NV22056		X		Zyx mainly impacted
NV22057			X	T > 1 s
NV22058	X			
NV22059			X	T > 10 s
NV22061			X	T > 0.3 s
NV22063		X		Only Zyx impacted
NV22064		X		
NV22065		X		Mainly Zxy impacted
NV22067		X		
NV22071		X		

Taking the data quality information shown above into account, the MT response data were resampled onto 39 frequency bands. Following resampling, prior to inverting the data for the electrical resistivity structure, response data near 8 s period found to be consistent with bias from non-plane wave effects from the Schumann resonances of the ionospheric waveguide were notched out; responses in the long-period dead-band that were excessively rough or with excessively large uncertainties were also discarded. After resampling and down-selection, the number of frequency bands used for the inversion of these data varied between 39 at some stations (e.g. NV22003) and 12 (at NV22026).

The geographic location of each of the NV22 wideband MT stations acquired during 2022 is found in the table on the following page.

### Enthalpion Job# NV22 MT station locations

Name	Longitude (deg E)	Latitude (deg N)
NV22057	-121.3128511	43.60715803
NV22059	-121.306798	43.5825819
NV22067	-121.2738634	43.57773199
NV22056	-121.2373139	43.57362012
NV22071	-121.2144192	43.56892367
NV22051	-121.1958451	43.57154628
NV22052	-121.1974141	43.58580077
NV22050	-121.338874	43.59539332
NV22061	-121.3621343	43.60313534
NV22065	-121.3768079	43.62547196
NV22064	-121.3536822	43.62694681
NV22063	-121.3246137	43.63035889
NV22053	-121.200486	43.60317594
NV22054	-121.2206724	43.60619317
NV22055	-121.2360085	43.59711586
NV22065RR	-121.3148396	43.7850118
NV22058	-121.269523	43.60848462
NV22047	-121.1615073	43.63539241
NV22023	-121.2718103	43.70102239
NV22021	-121.2780643	43.70537918
NV22020	-121.2779302	43.70058917
NV22018	-121.2844935	43.69632171
NV22017	-121.2939221	43.69215538
NV22027	-121.2247057	43.69130462
NV22001	-121.2348007	43.67909814
NV22026	-121.2772484	43.68542845
NV22024	-121.2632685	43.68666986
NV22016	-121.2991224	43.68290915
NV22015	-121.3053841	43.67350602
NV22034	-121.1926723	43.70355485
NV22035	-121.1905829	43.69748036
NV22036	-121.1916862	43.69157924
NV22038	-121.1945354	43.68405059
NV22033	-121.2243987	43.70593651
NV22030	-121.2037701	43.69760336
NV22029	-121.2130382	43.69690266



NV22002	-121.2178489	43.67295622
NV22005	-121.2163367	43.66083534
NV22013	-121.2880277	43.67419293
NV22009	-121.2768499	43.66671761
NV22011	-121.2894689	43.66368107
NV22003	-121.2370412	43.64643287
NV22004	-121.2509704	43.65079109

## EDI Files and Plots

EDI files for the NV22 stations are provided in the **MT Response Data/MT\_Original** folder in the electronic distribution of the final product release. Each file contains full tensor impedances, tippers and error estimates for the frequency bands indicated. These responses are from robust remote reference processed data using a paired station in the array and the contain the full set of periods (1/frequencies) resulting for the robust signal processing methods used. As noted later in this report, the EDI files for the MT responses for the periods actually used in the single and joint inversions are found in the **MT Response Data/MT\_PickedForInversion** folder.

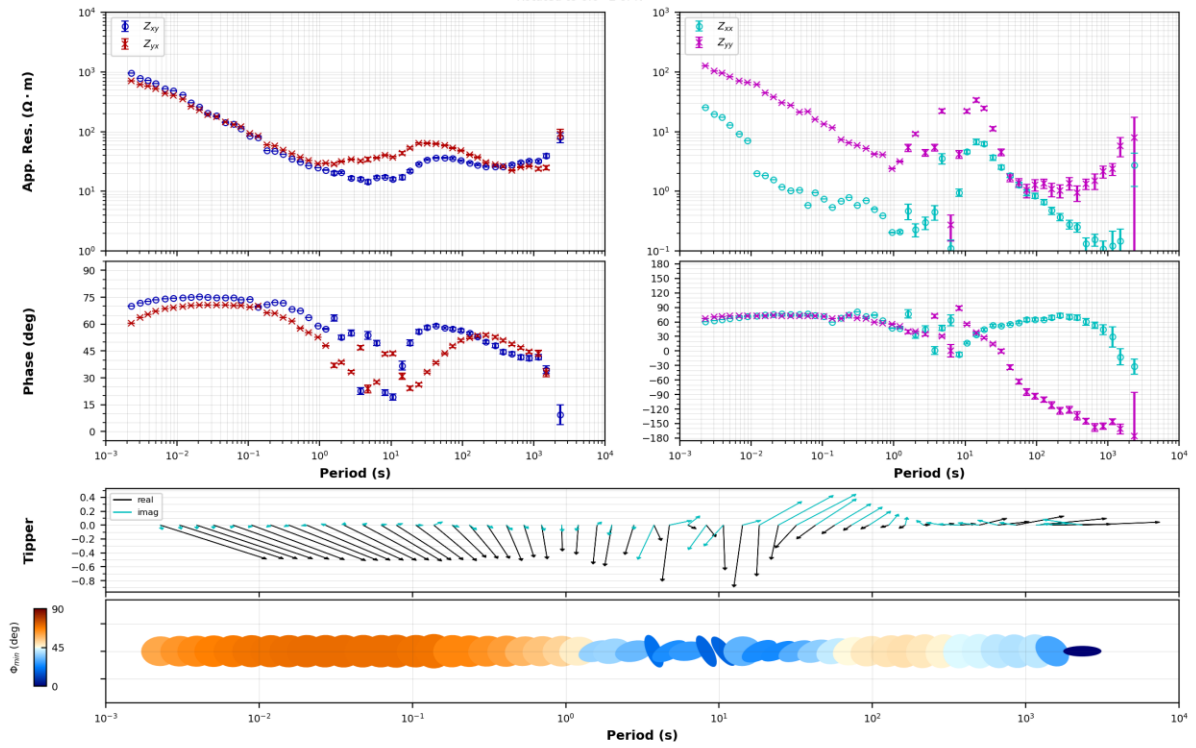
Plots of the robust remote reference processes MT responses for the four impedance tensor elements, scaled into apparent resistivity and phase, as well as tippers (displayed as vectors) and phase tensors are provided in .png format in the **MT Response Data/MT\_Original/images** folder in the electronic distribution of the final product release. Copies of these plots are found in the pages following. Please note that the response functions as plotted have been rotated into geographic coordinates, where the  $x$  direction is geographic north,  $y$  is geographic east, and  $z$  is positive downward.

(remainder of page left blank)

Oregon State University

**NV22001**  
Rotated to 0.0° E of N

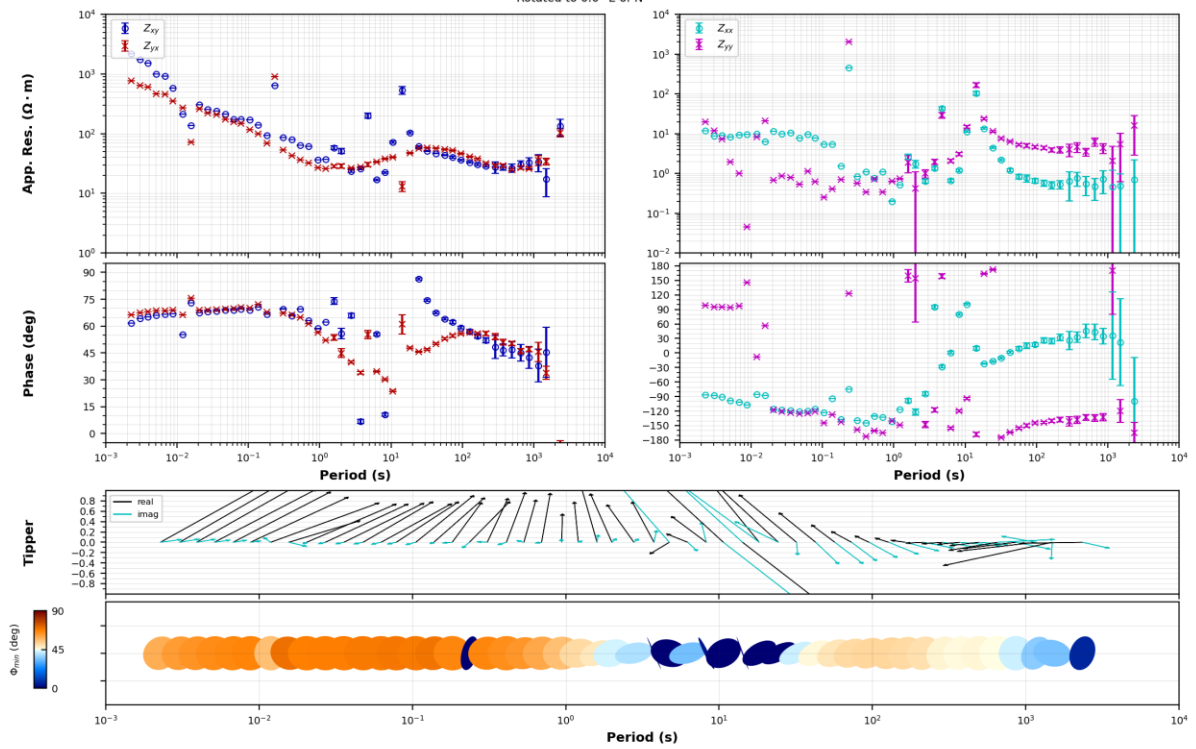
Enthalpion Energy LLC

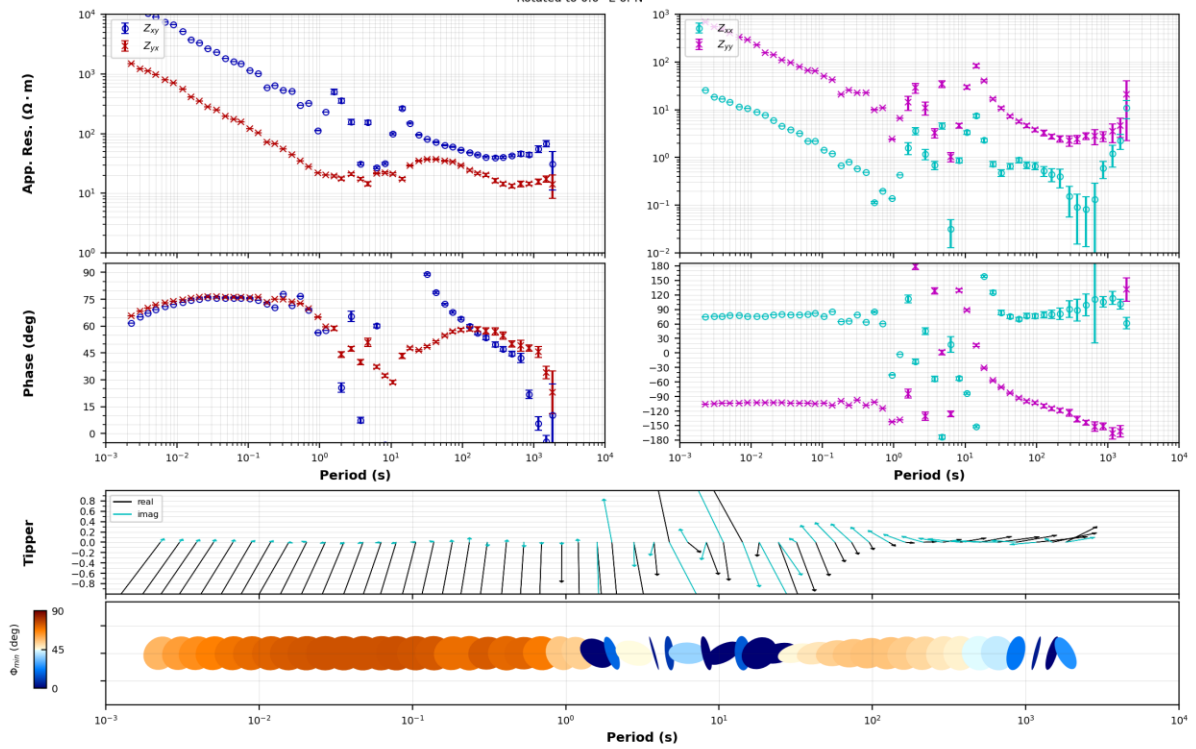
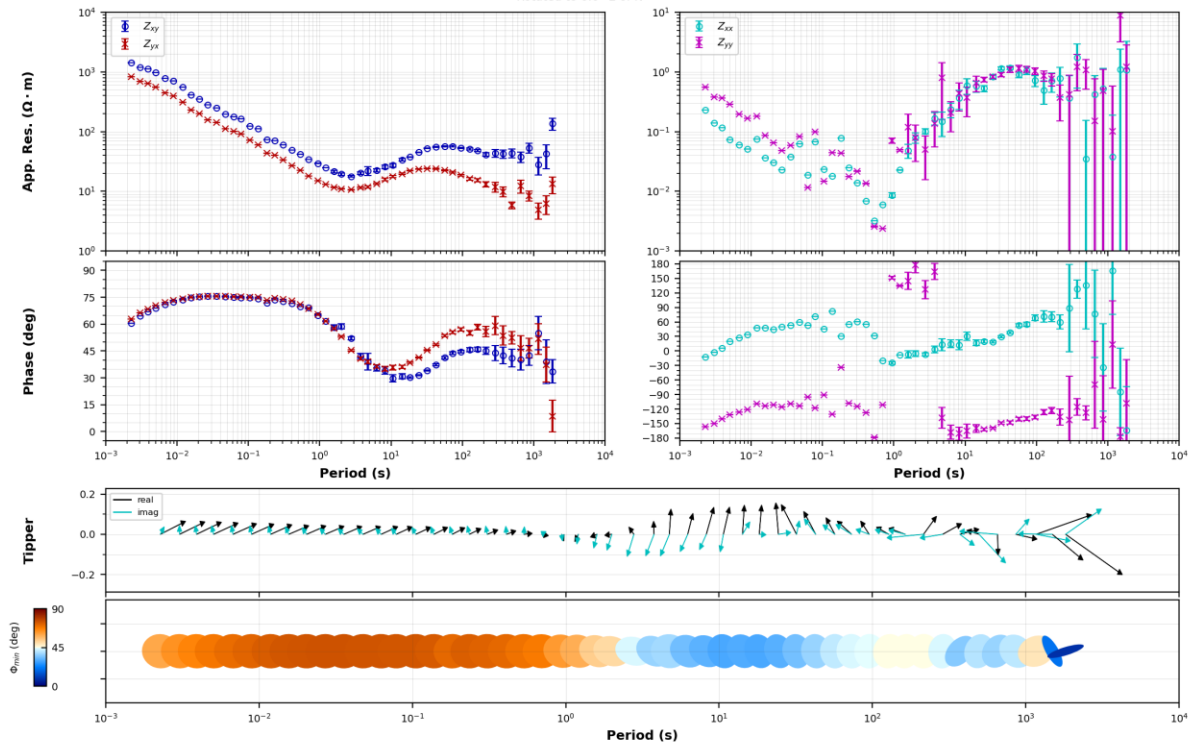


Oregon State University

**NV22002**  
Rotated to 0.0° E of N

Enthalpion Energy LLC

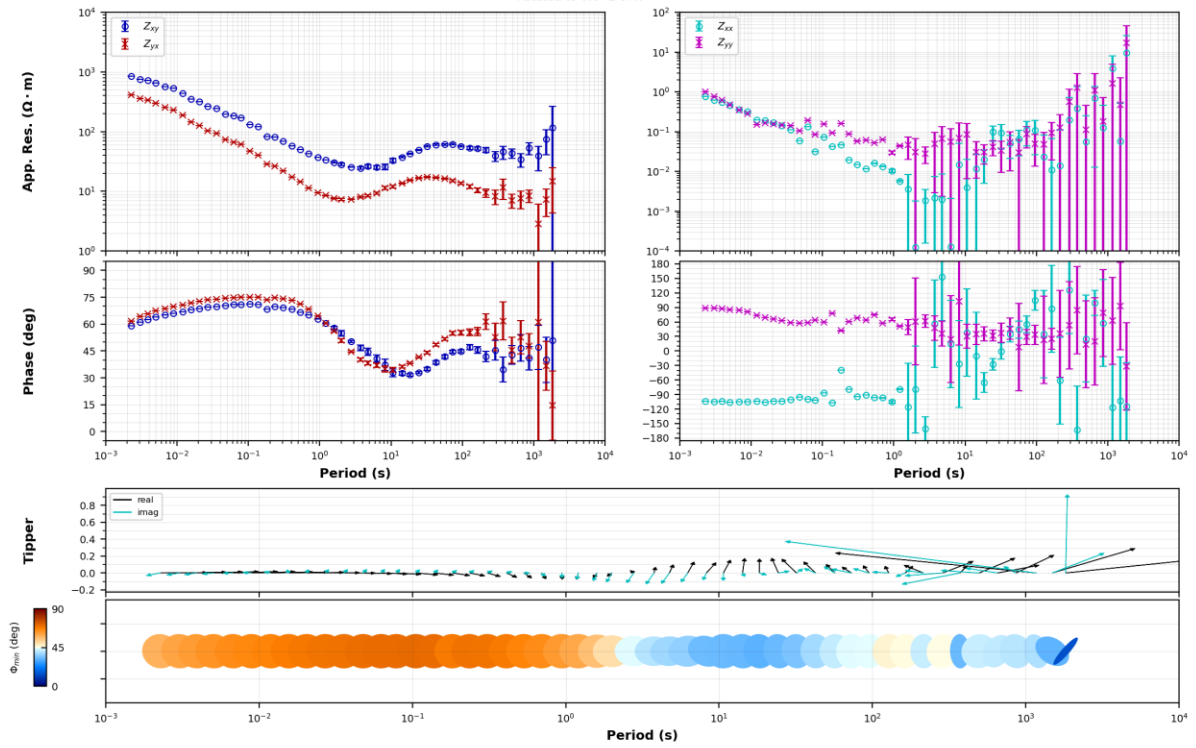




Oregon State University

**NV22005**  
Rotated to 0.0° E of N

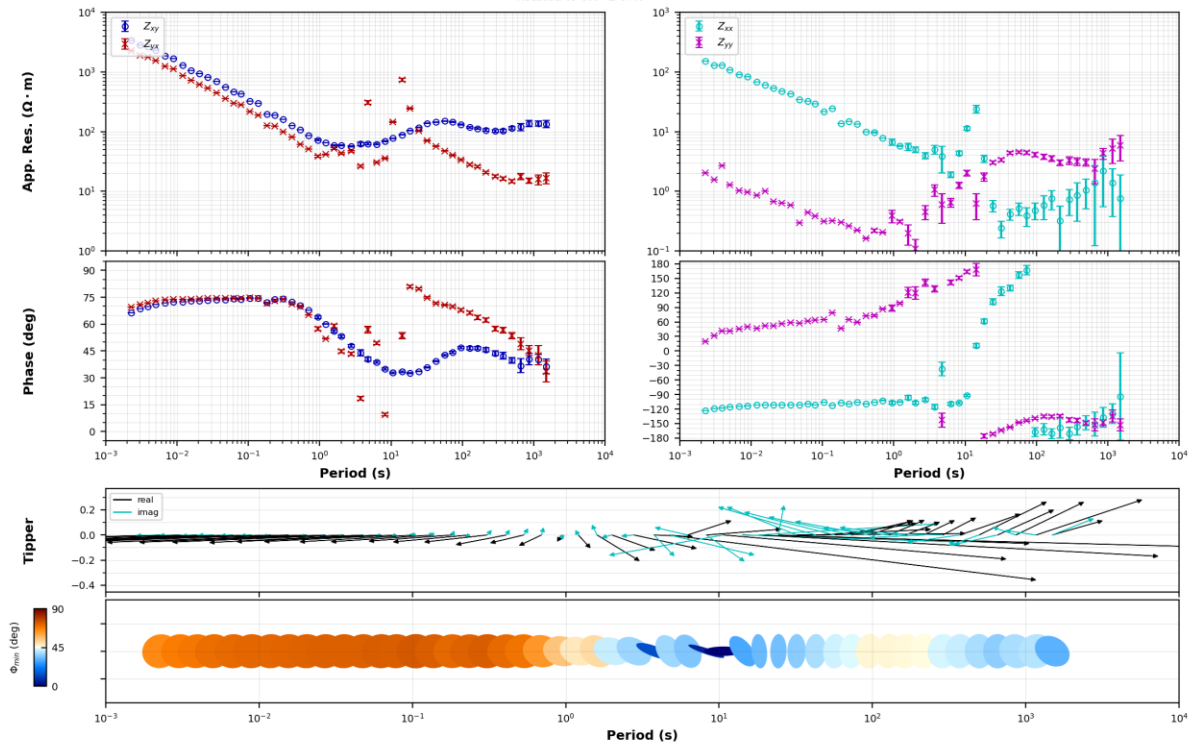
Enthalpion Energy LLC



Oregon State University

**NV22009**  
Rotated to 0.0° E of N

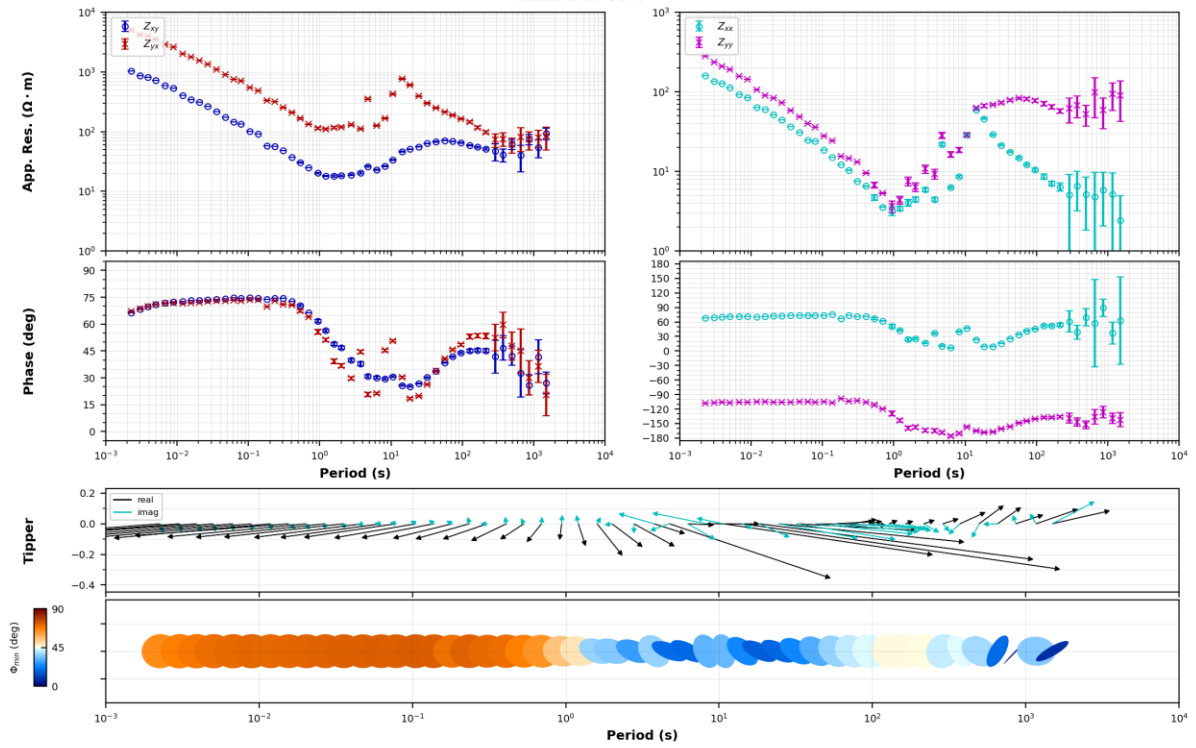
Enthalpion Energy LLC



Oregon State University

**NV22011**  
Rotated to 0.0° E of N

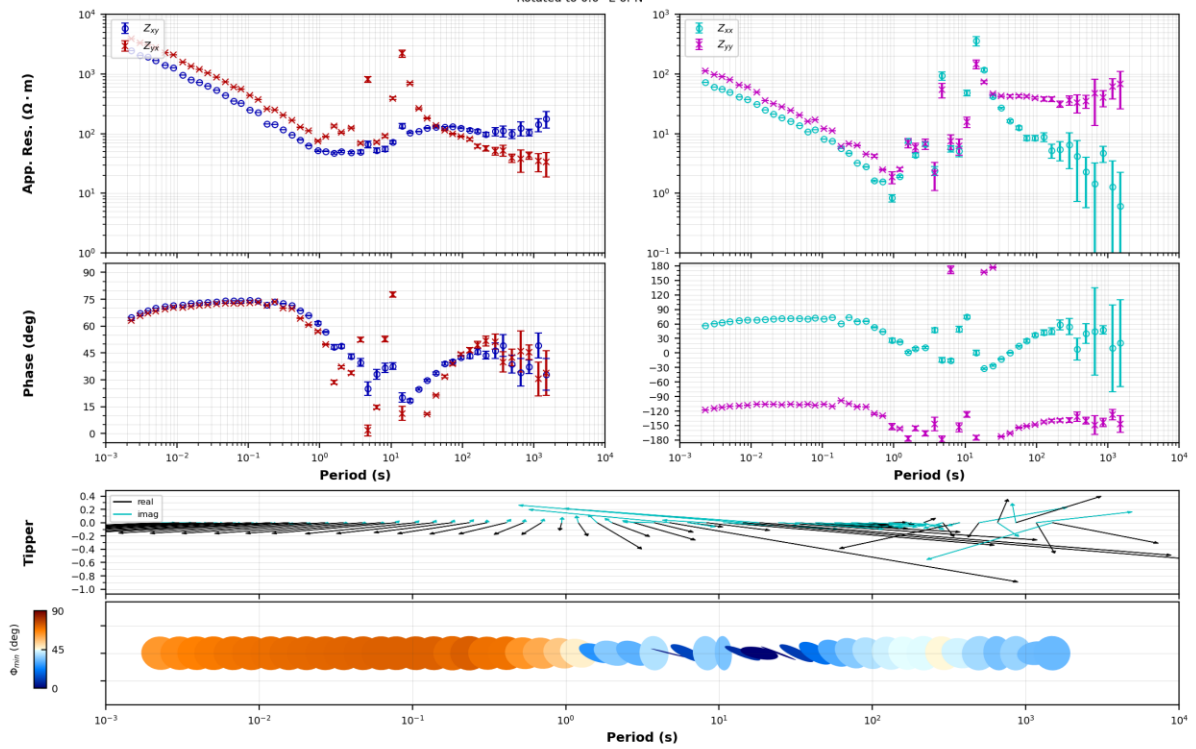
Enthalpion Energy LLC



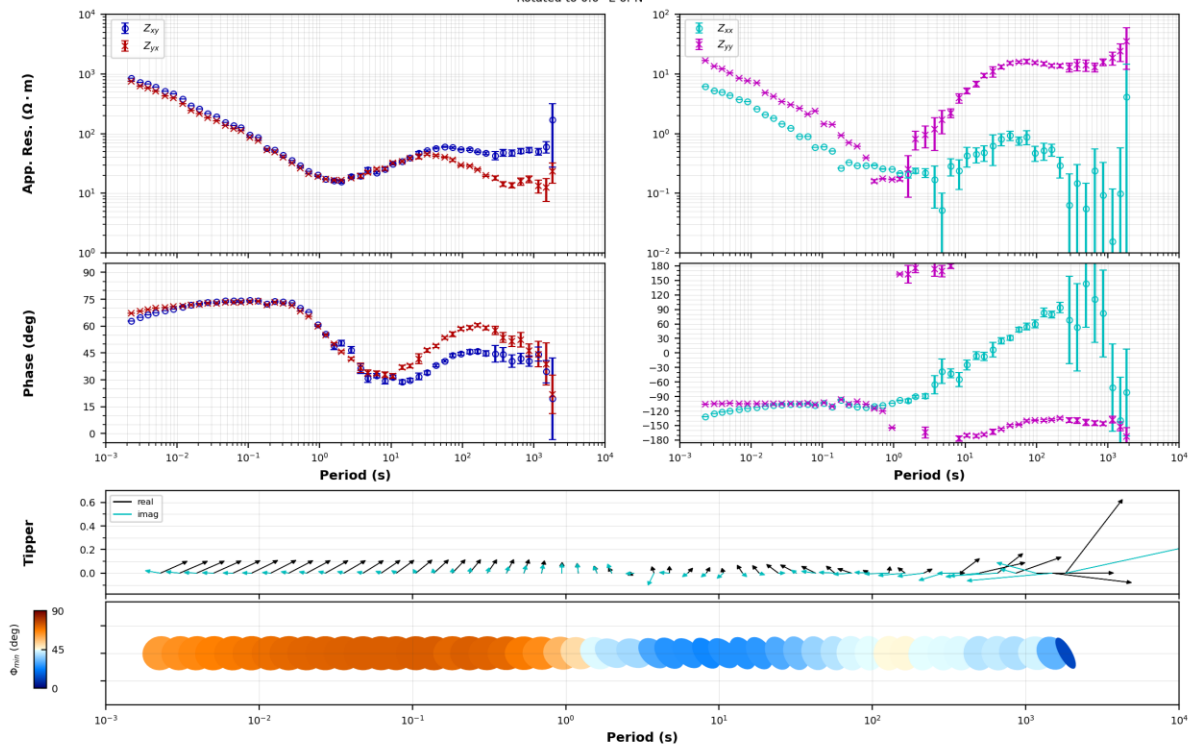
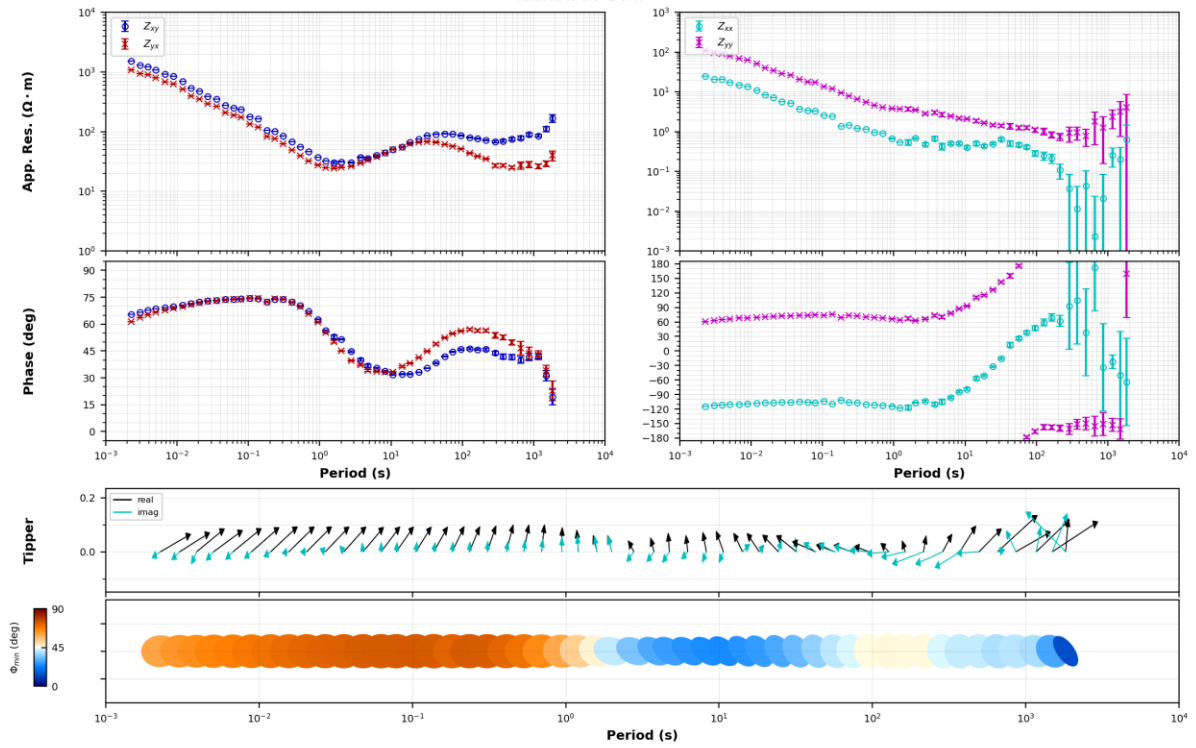
Oregon State University

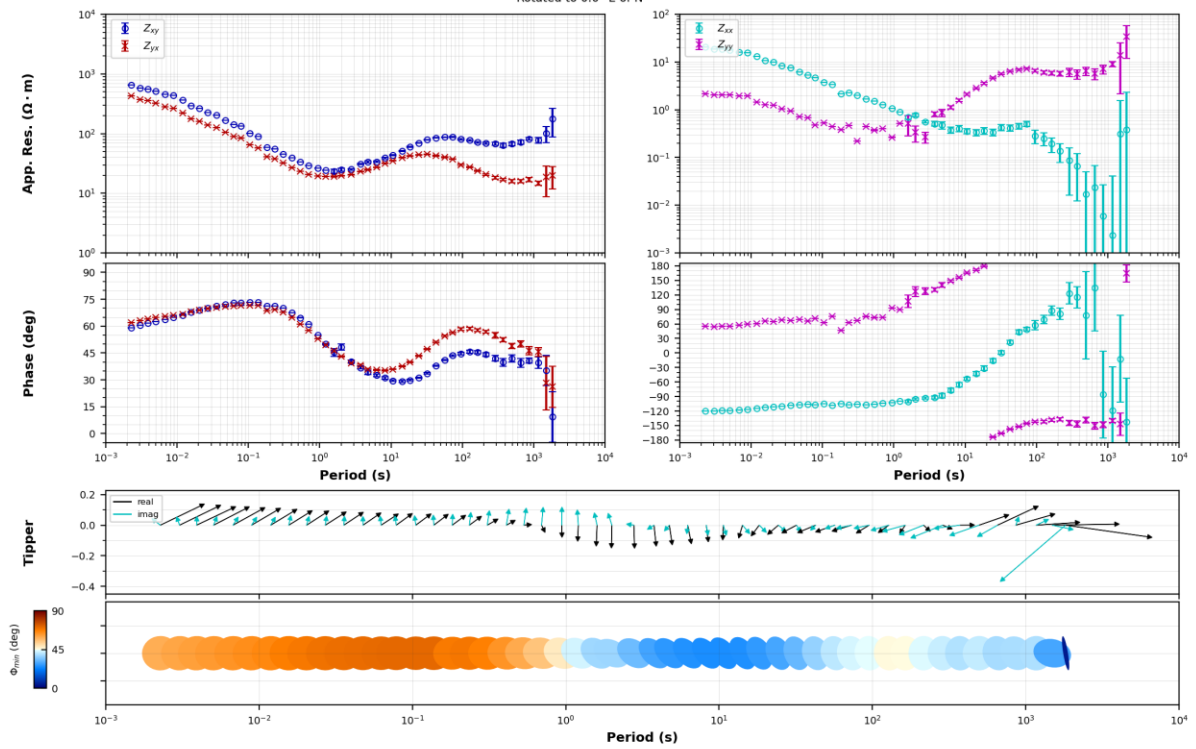
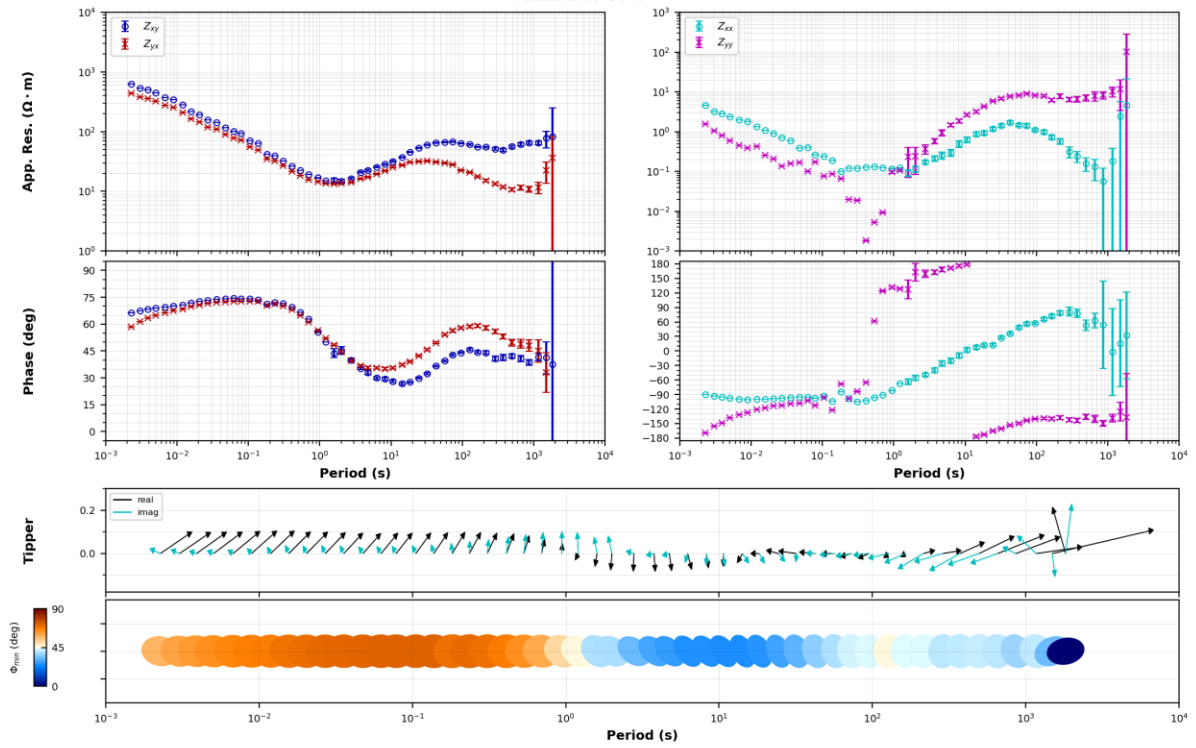
**NV22013**  
Rotated to 0.0° E of N

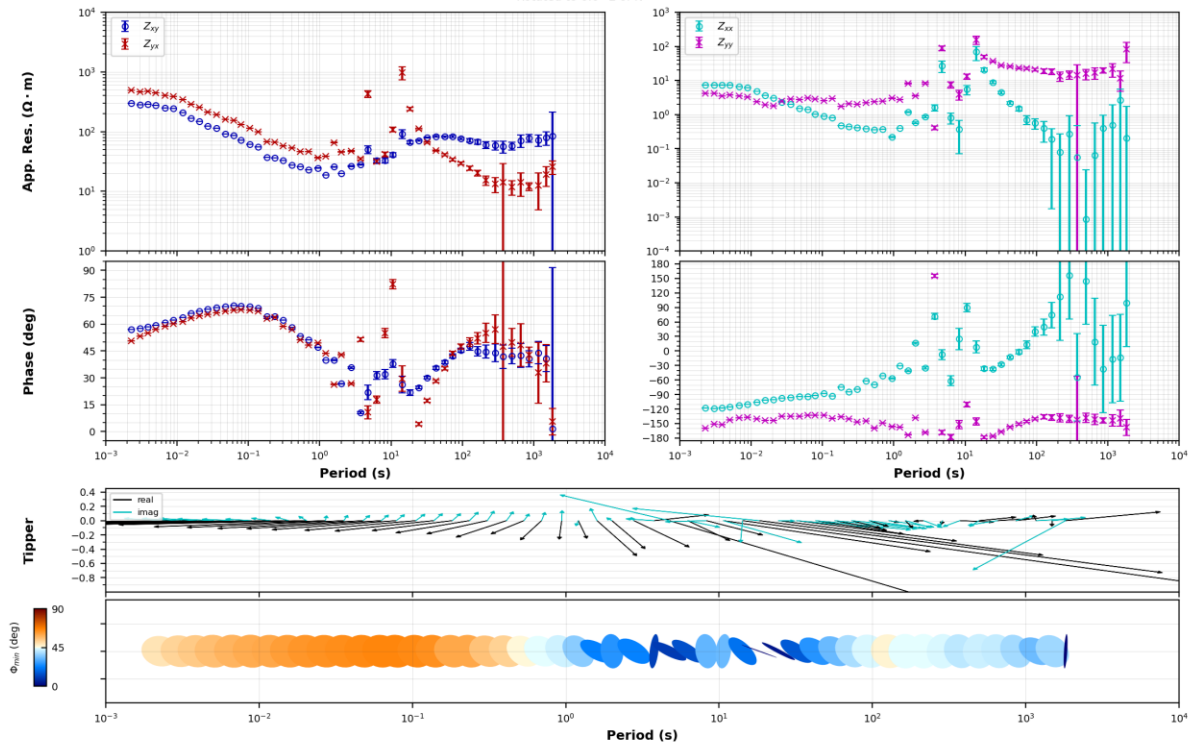
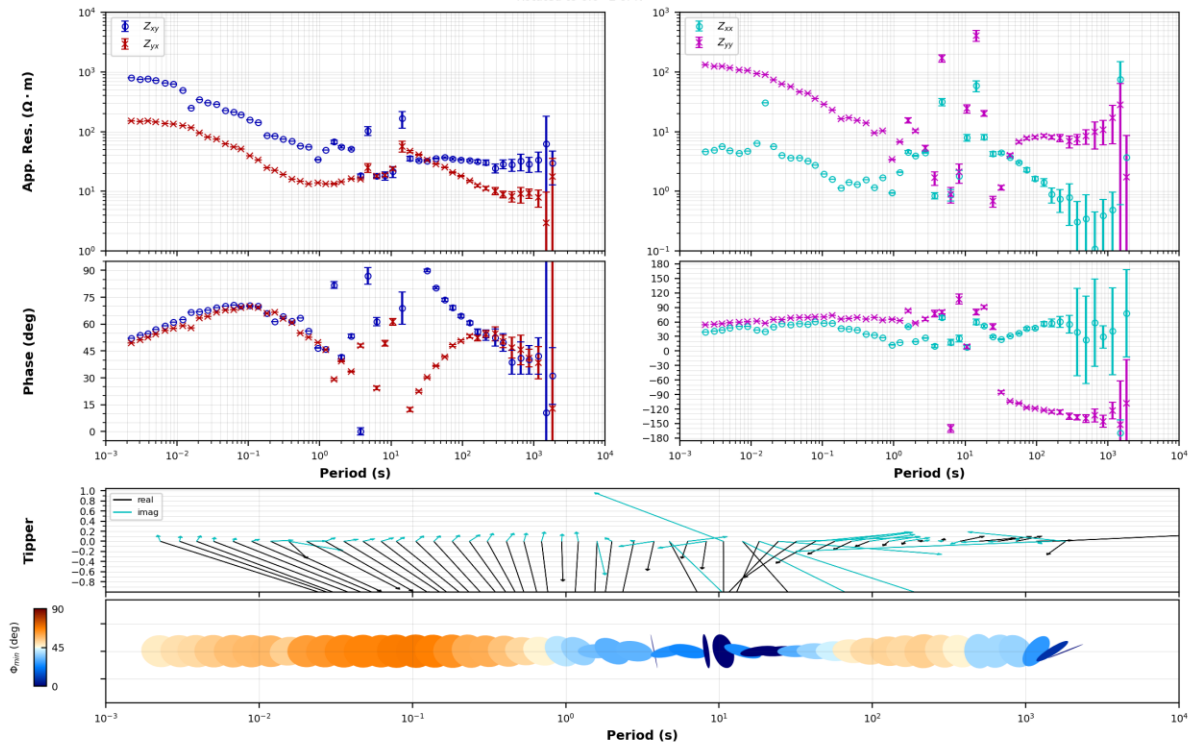
Enthalpion Energy LLC

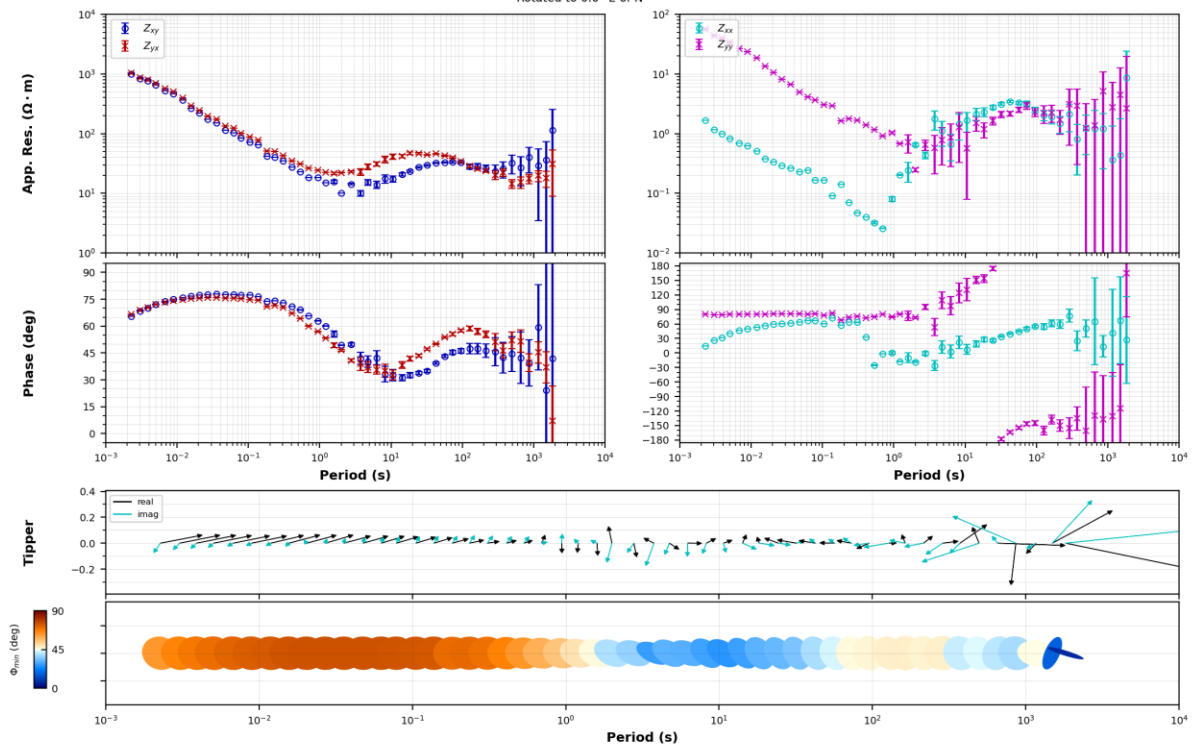
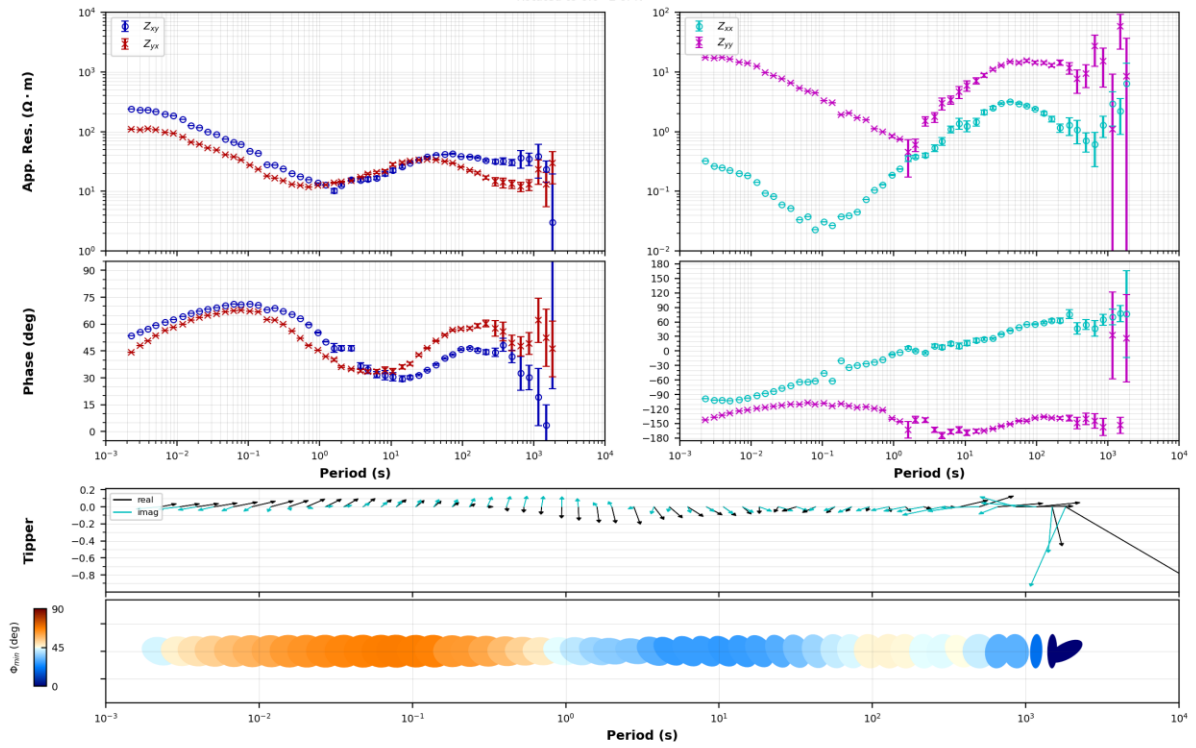


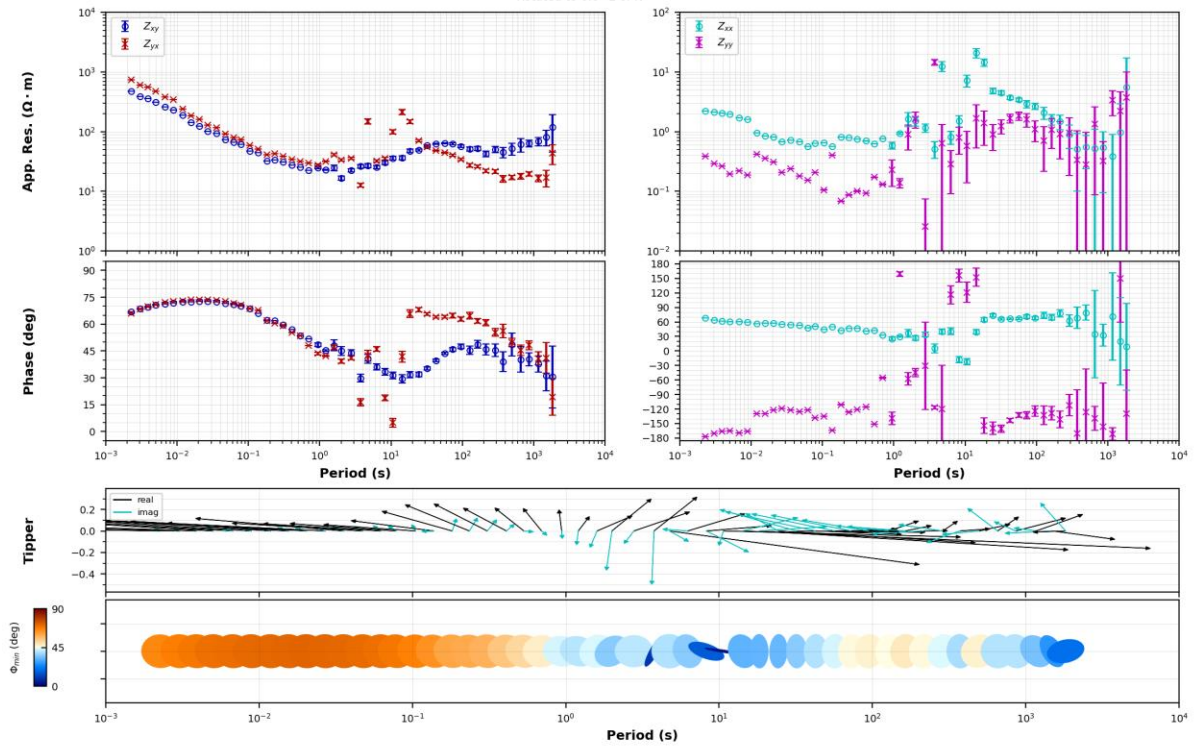
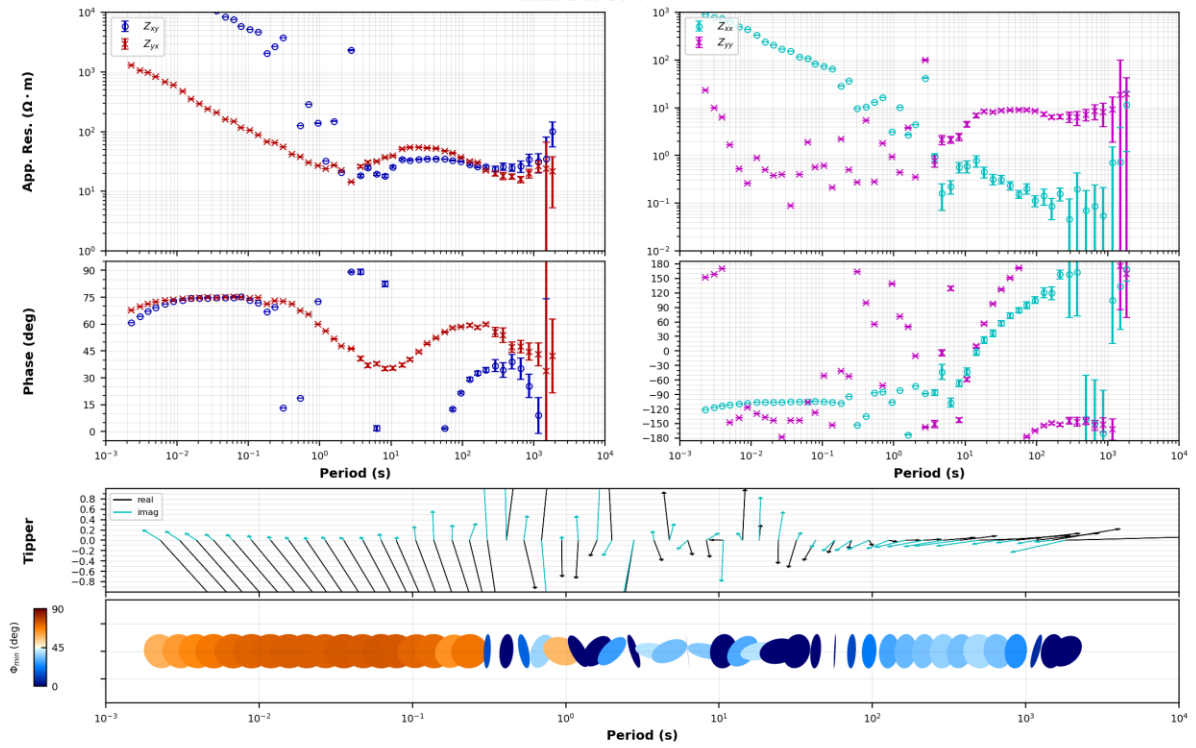




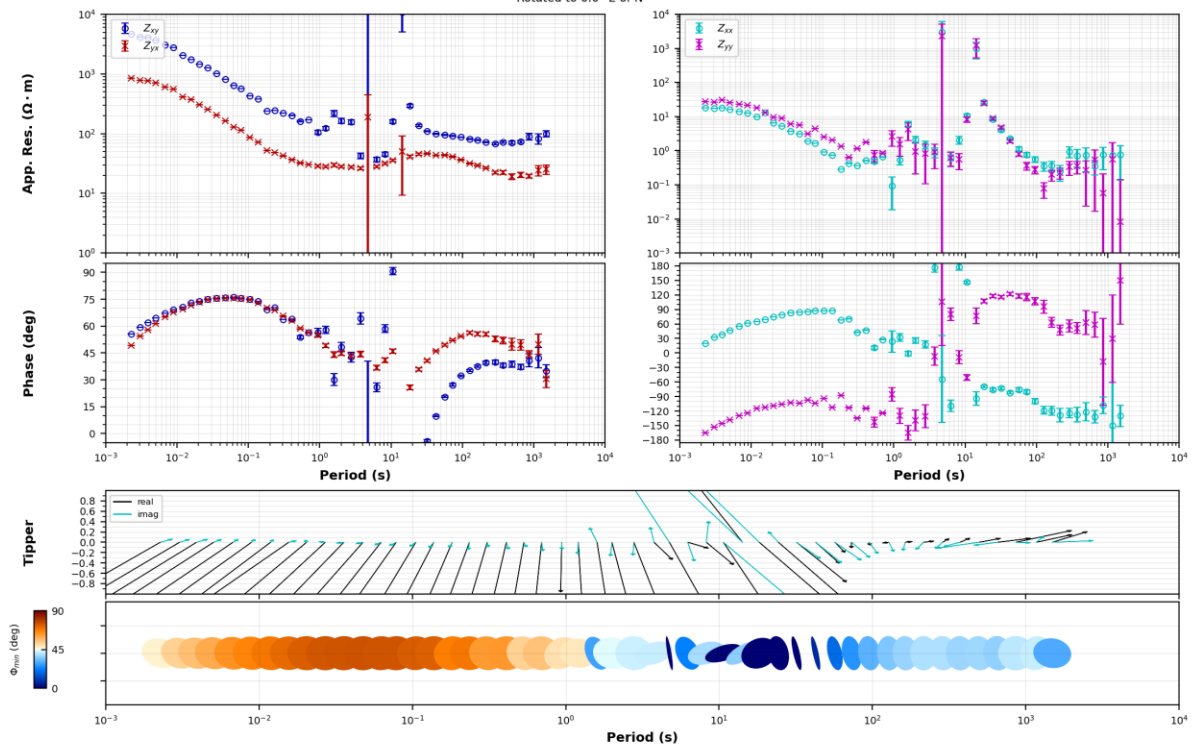
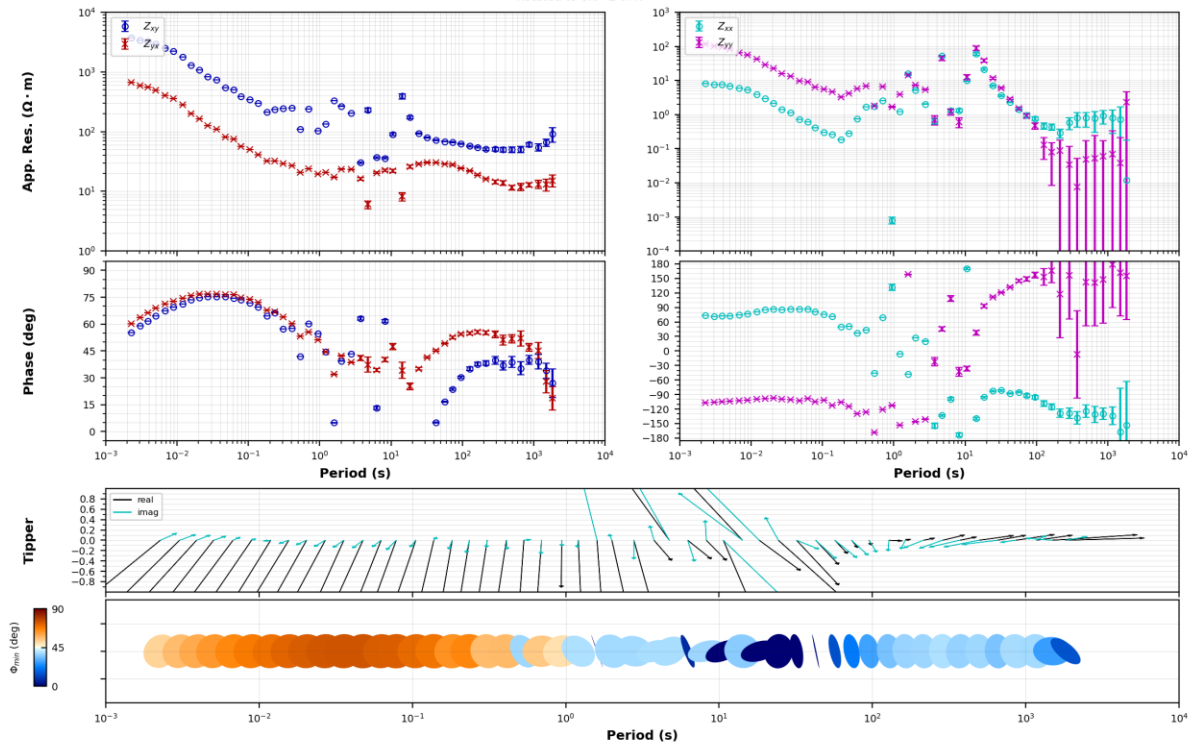




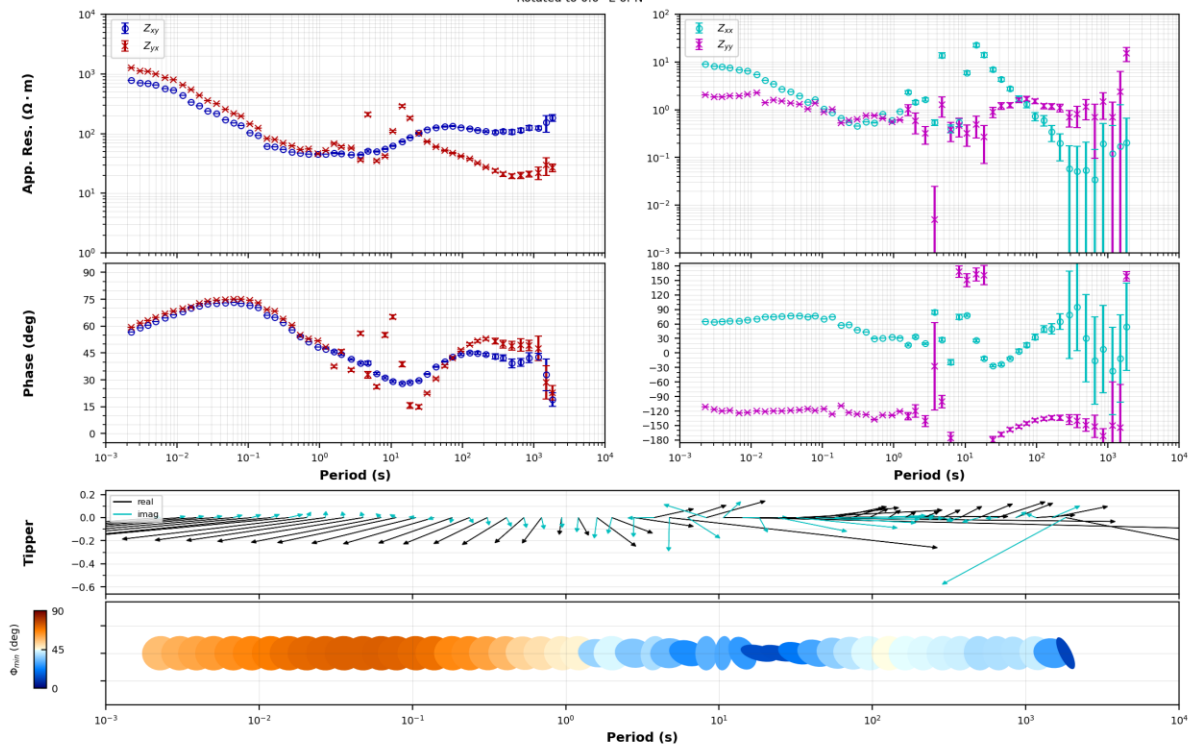
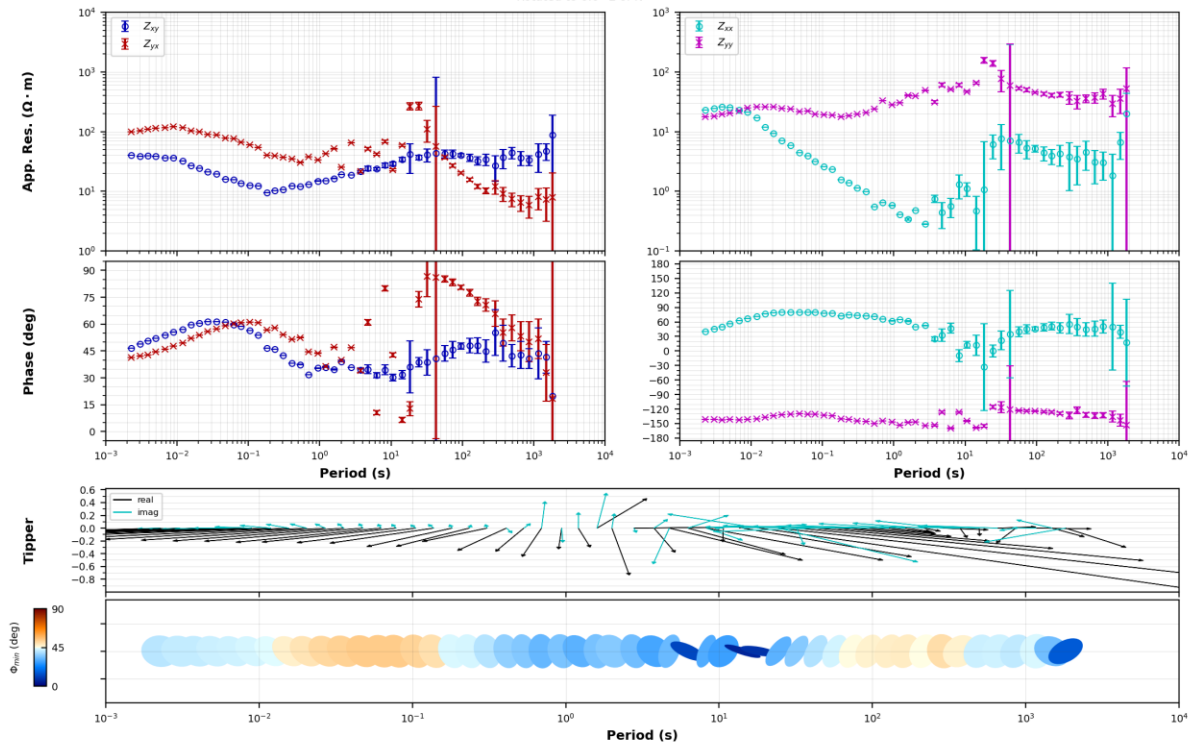








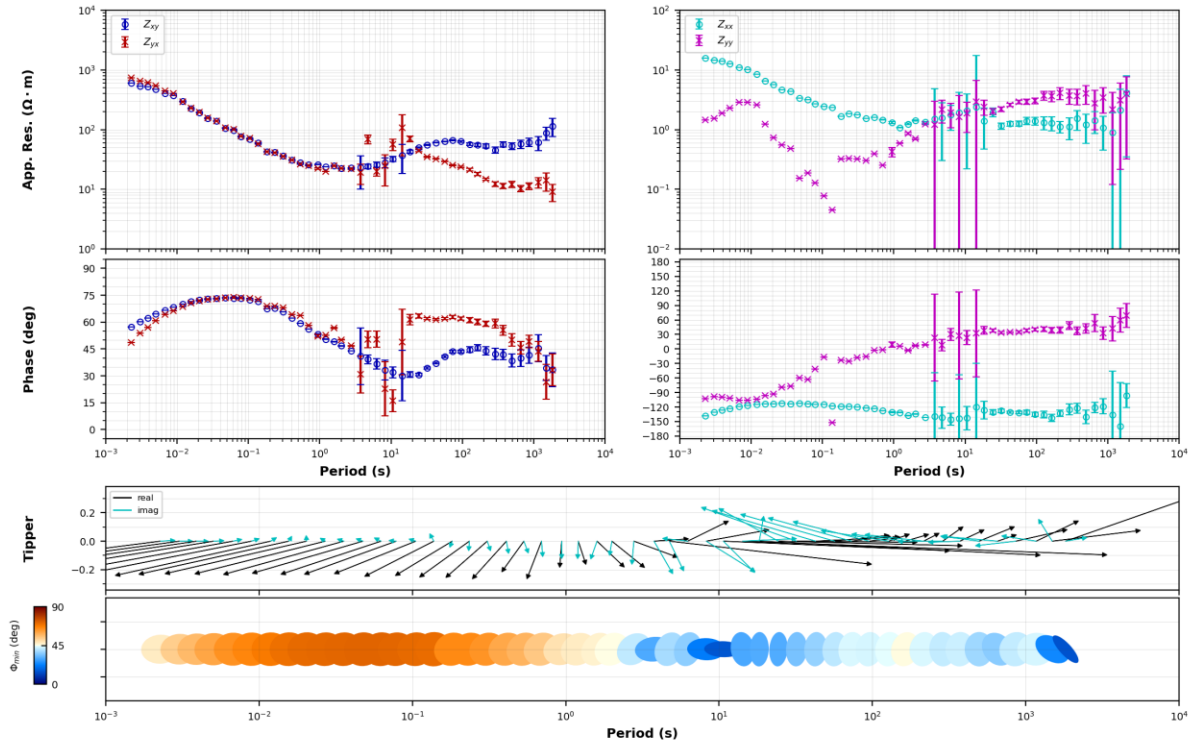




Oregon State University

**NV22035**  
Rotated to 0.0° E of N

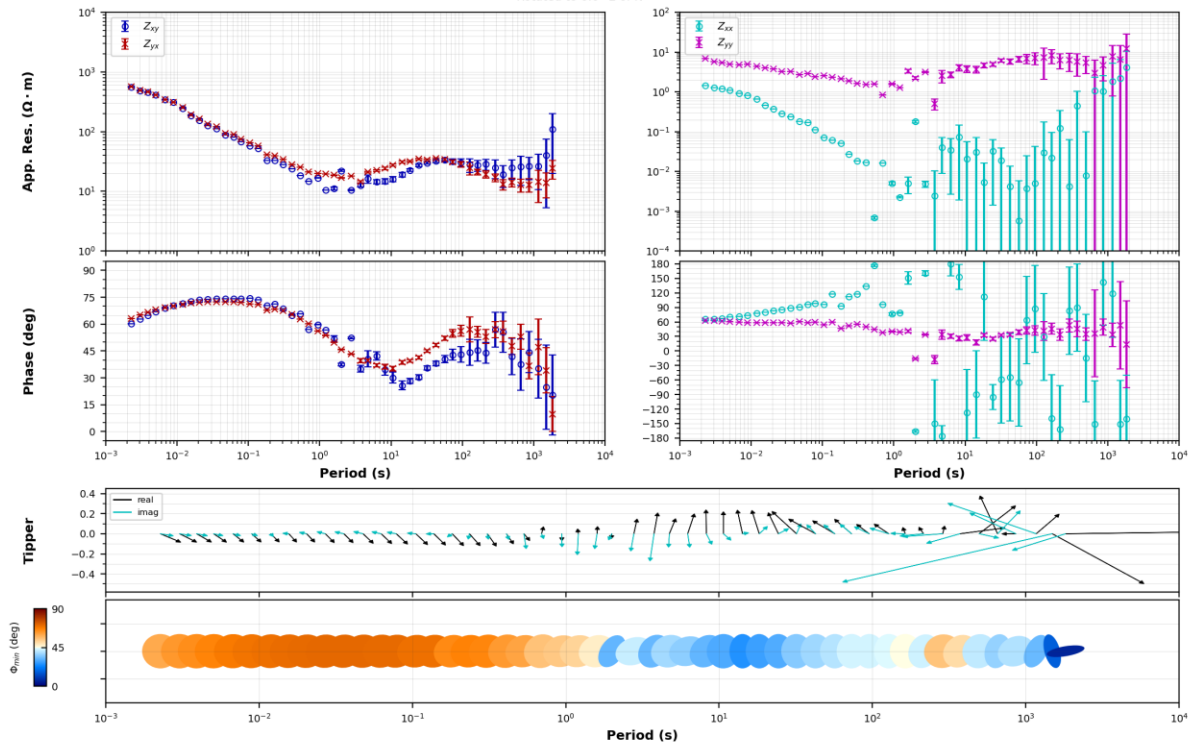
Enthalpion Energy LLC

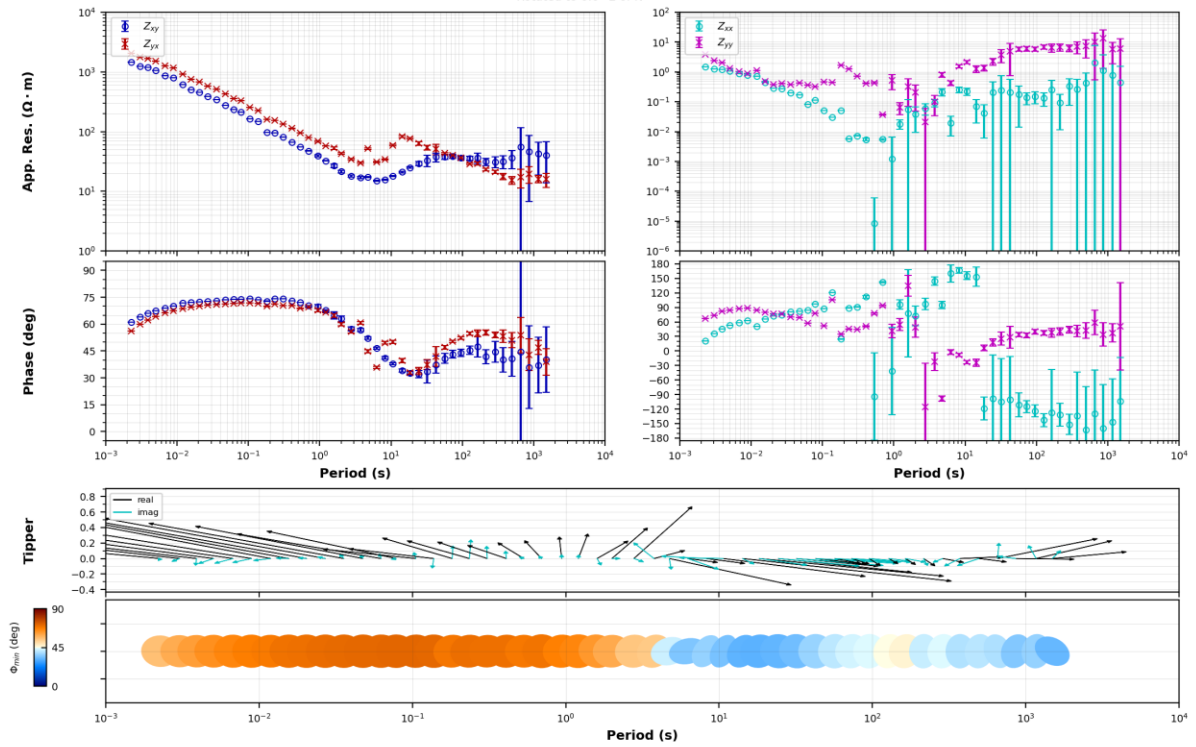
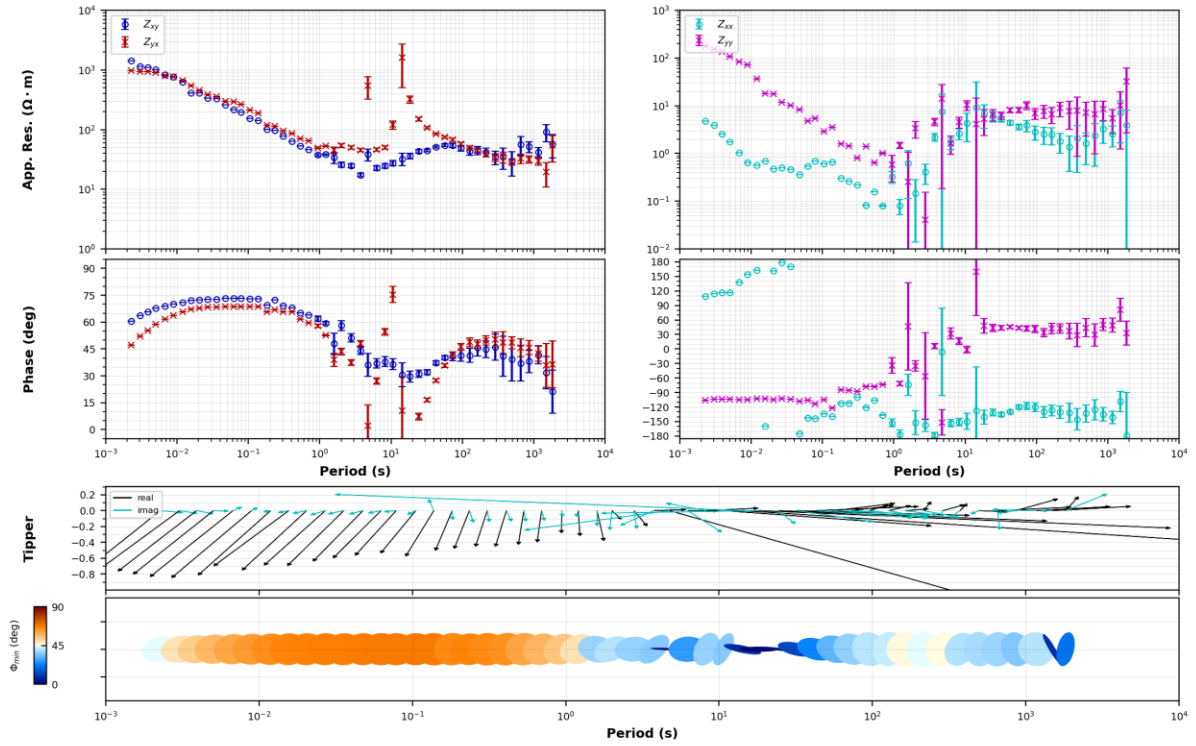


Oregon State University

**NV22036**  
Rotated to 0.0° E of N

Enthalpion Energy LLC

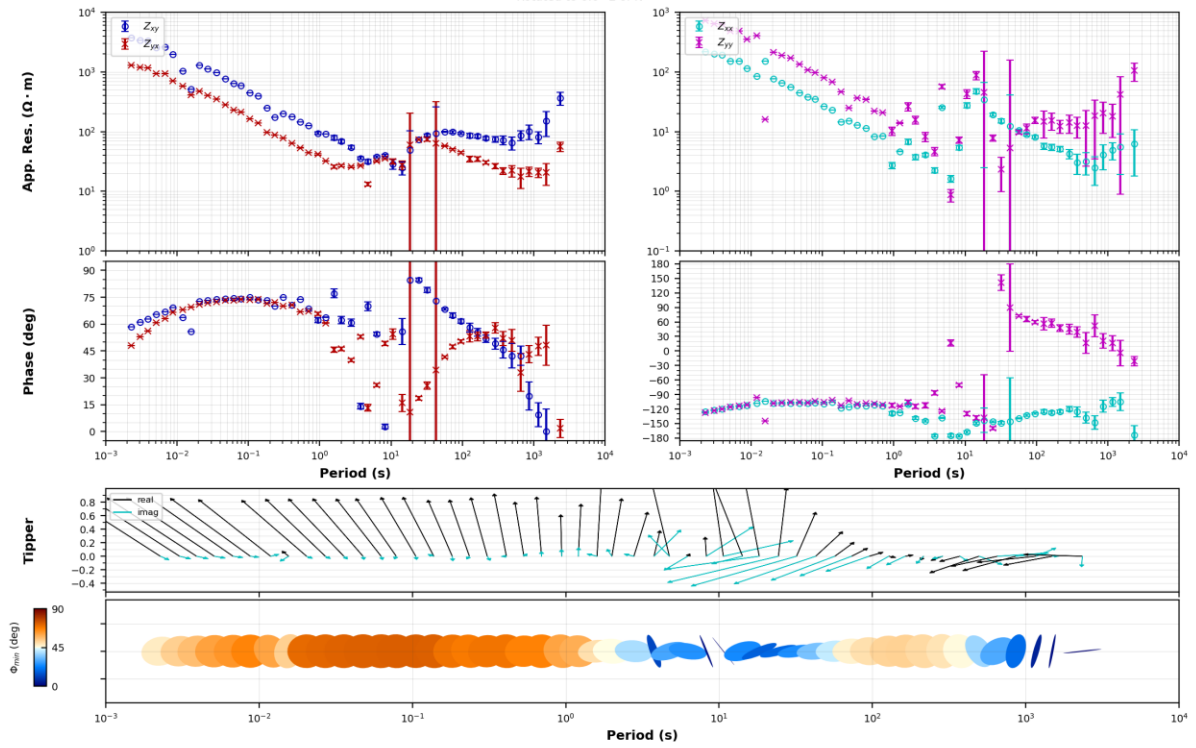




Oregon State University

**NV22050**  
Rotated to 0.0° E of N

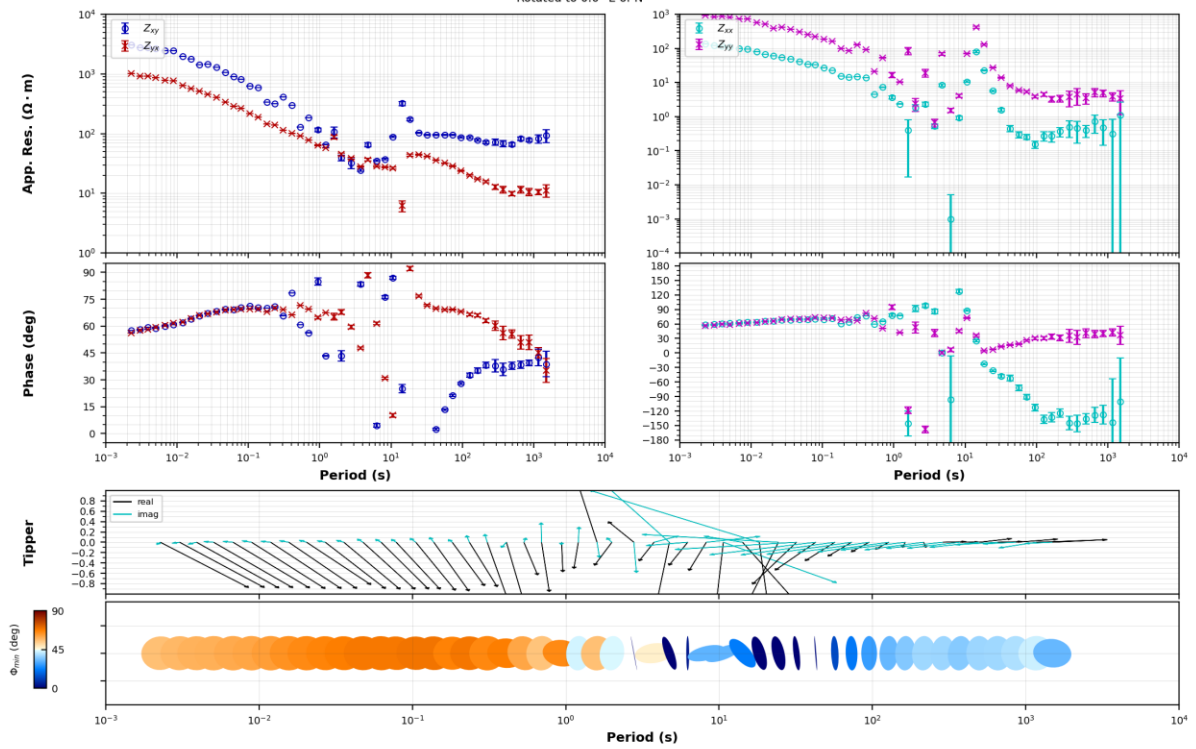
Enthalpion Energy LLC

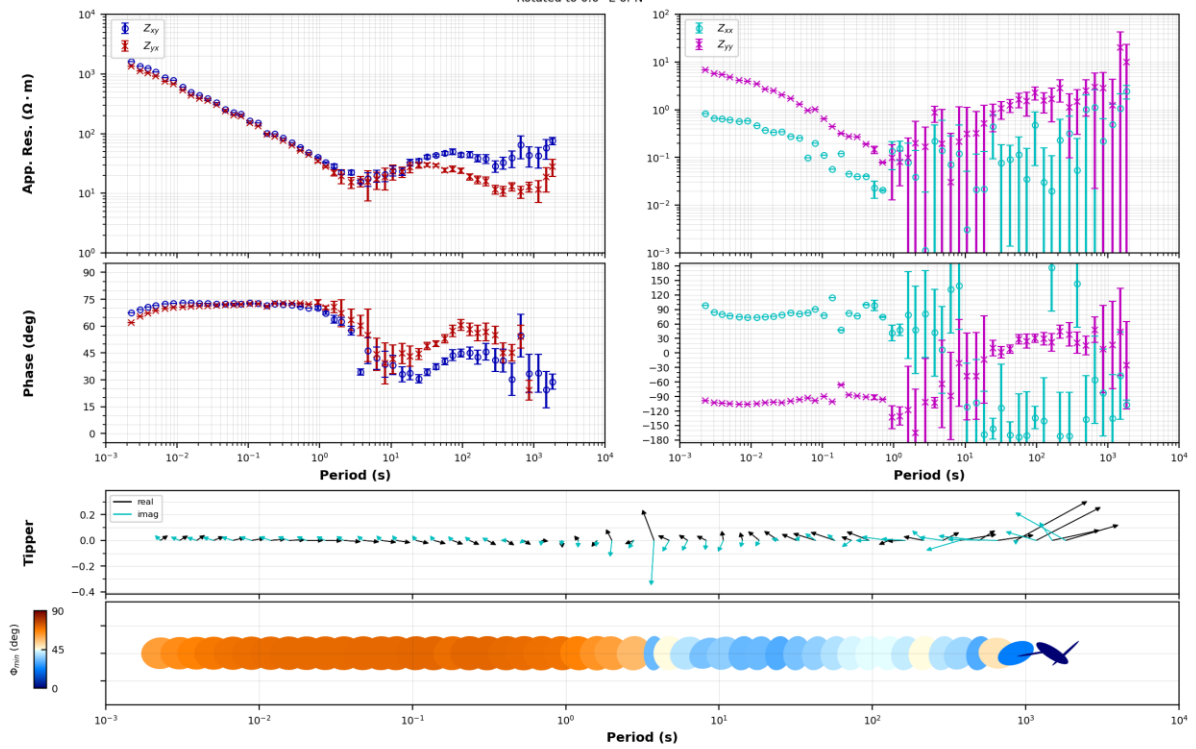
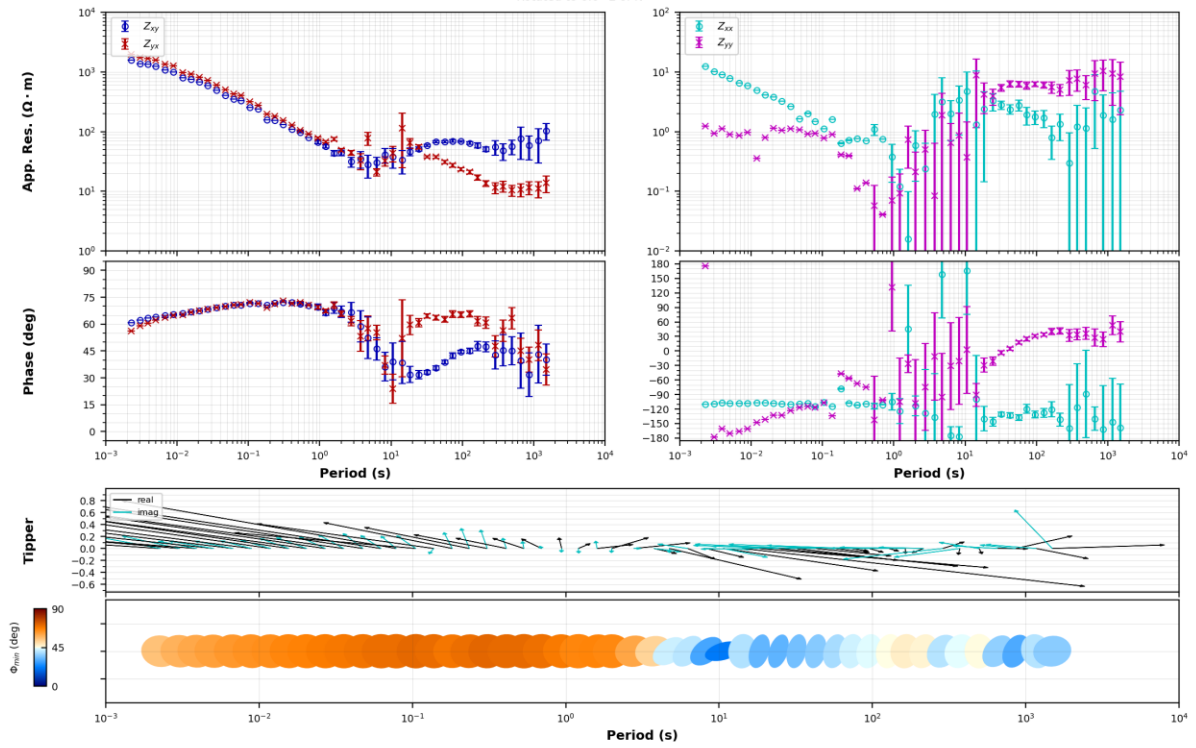


Oregon State University

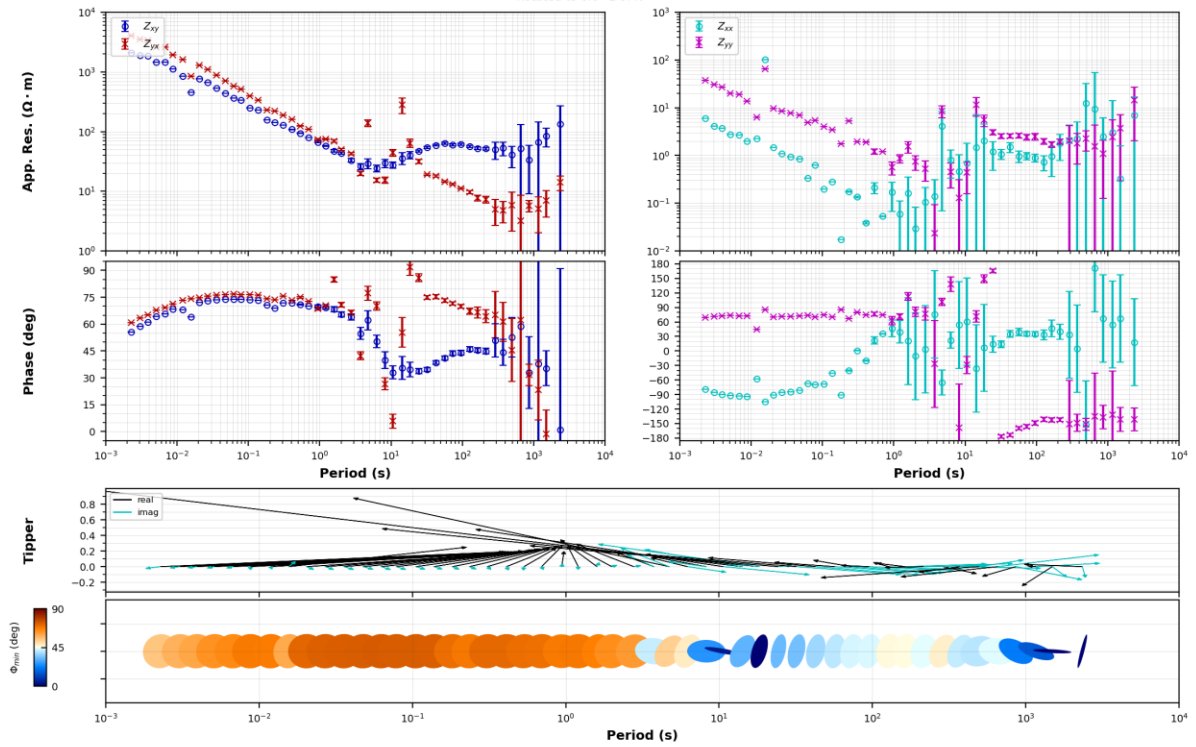
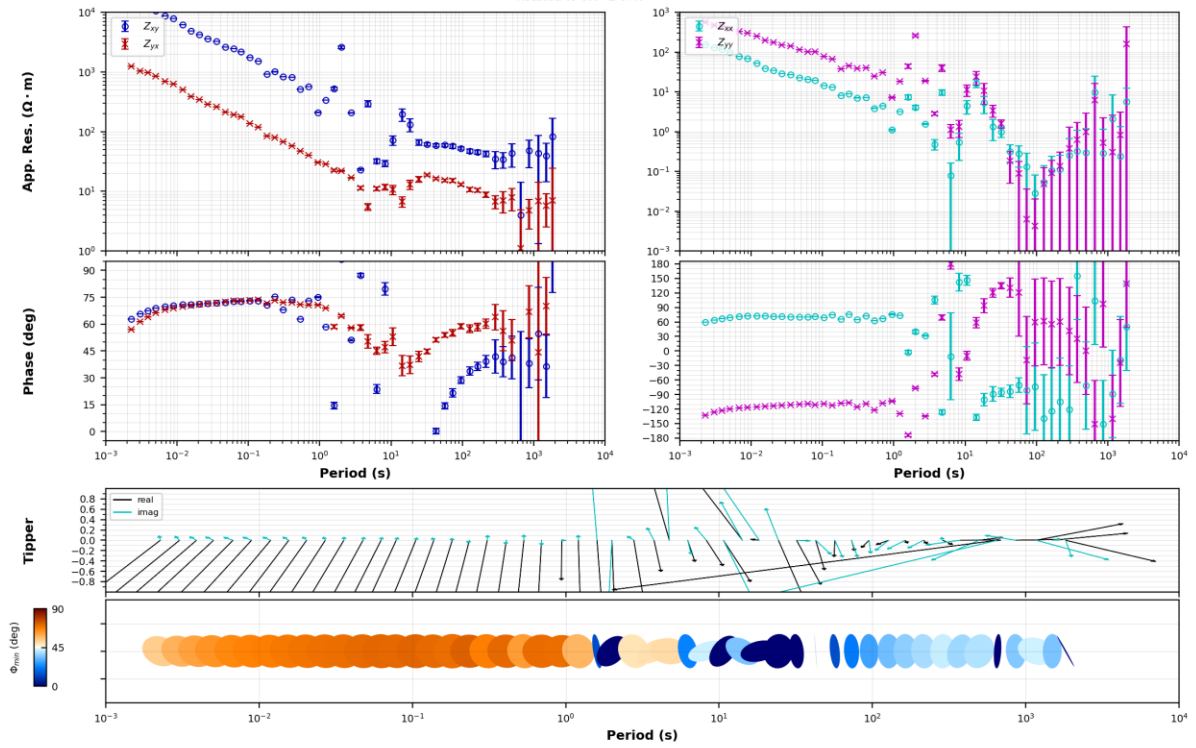
**NV22051**  
Rotated to 0.0° E of N

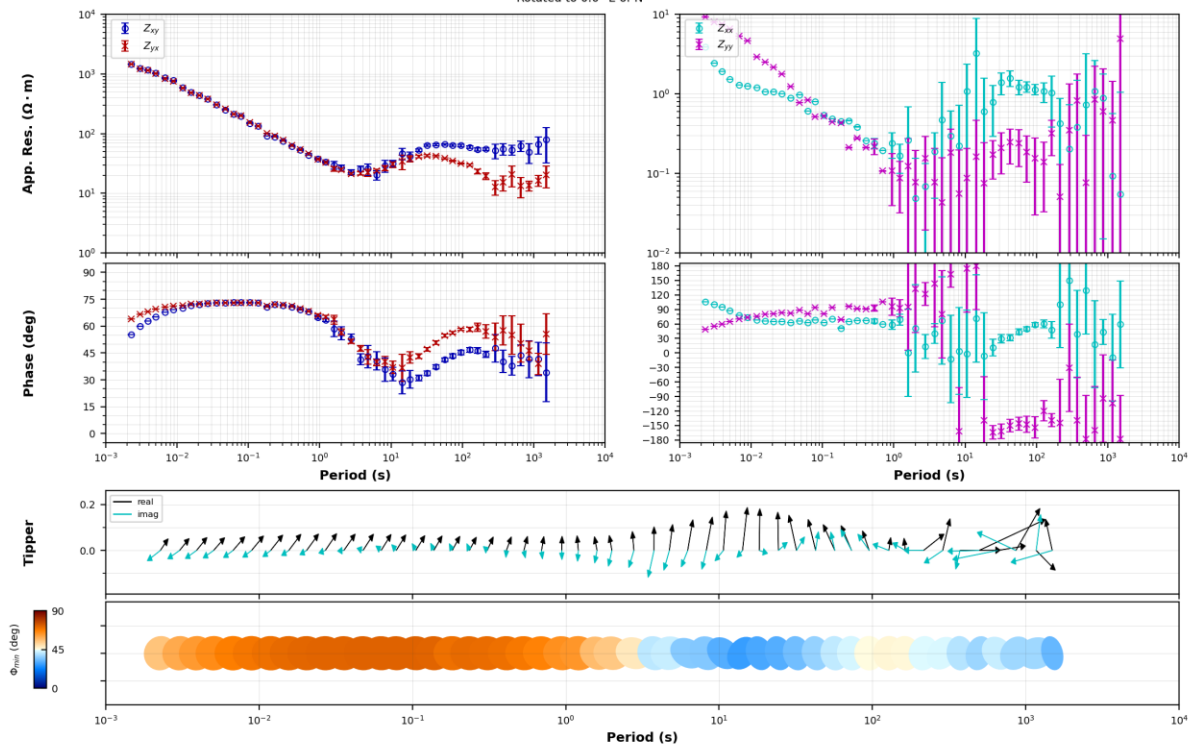
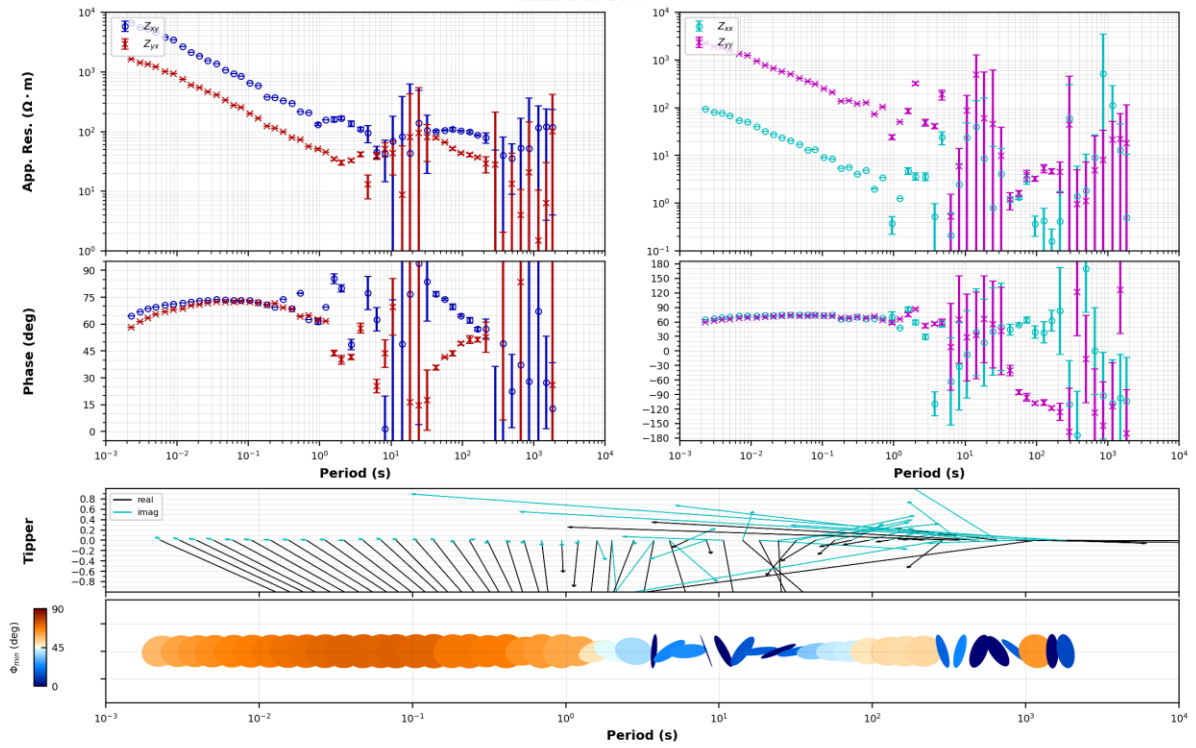
Enthalpion Energy LLC







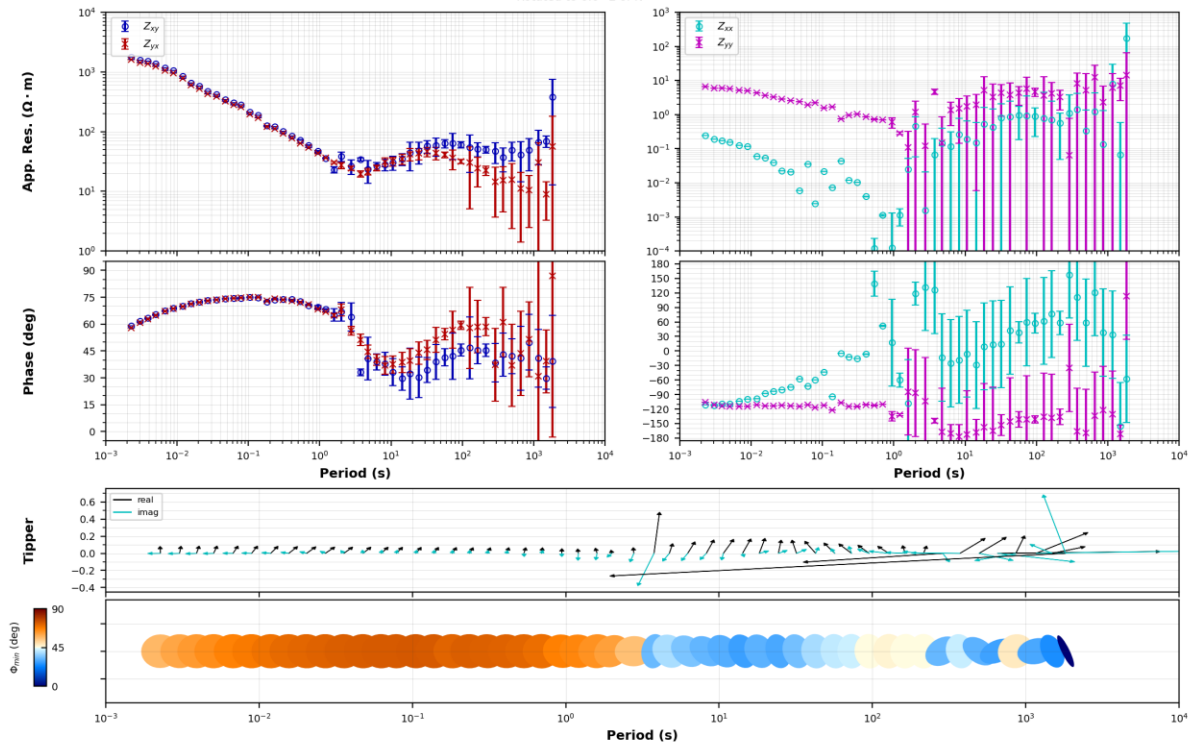




Oregon State University

**NV22059**  
Rotated to 0.0° E of N

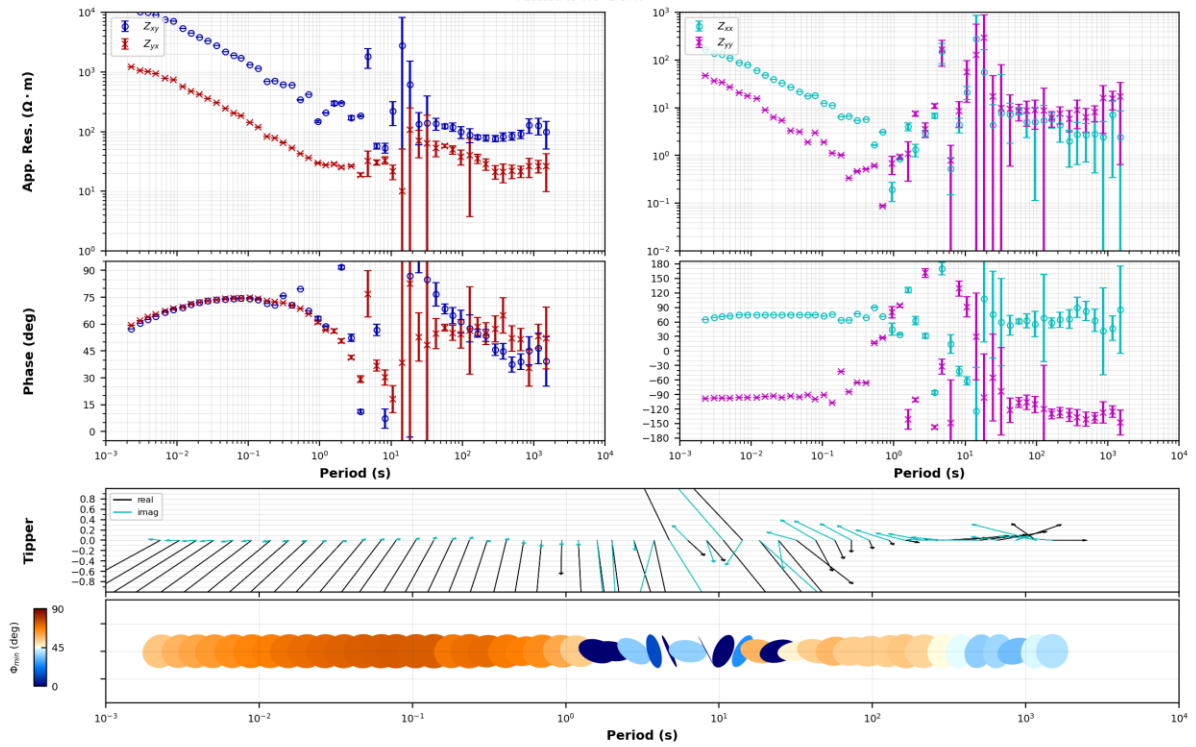
Enthalpion Energy LLC

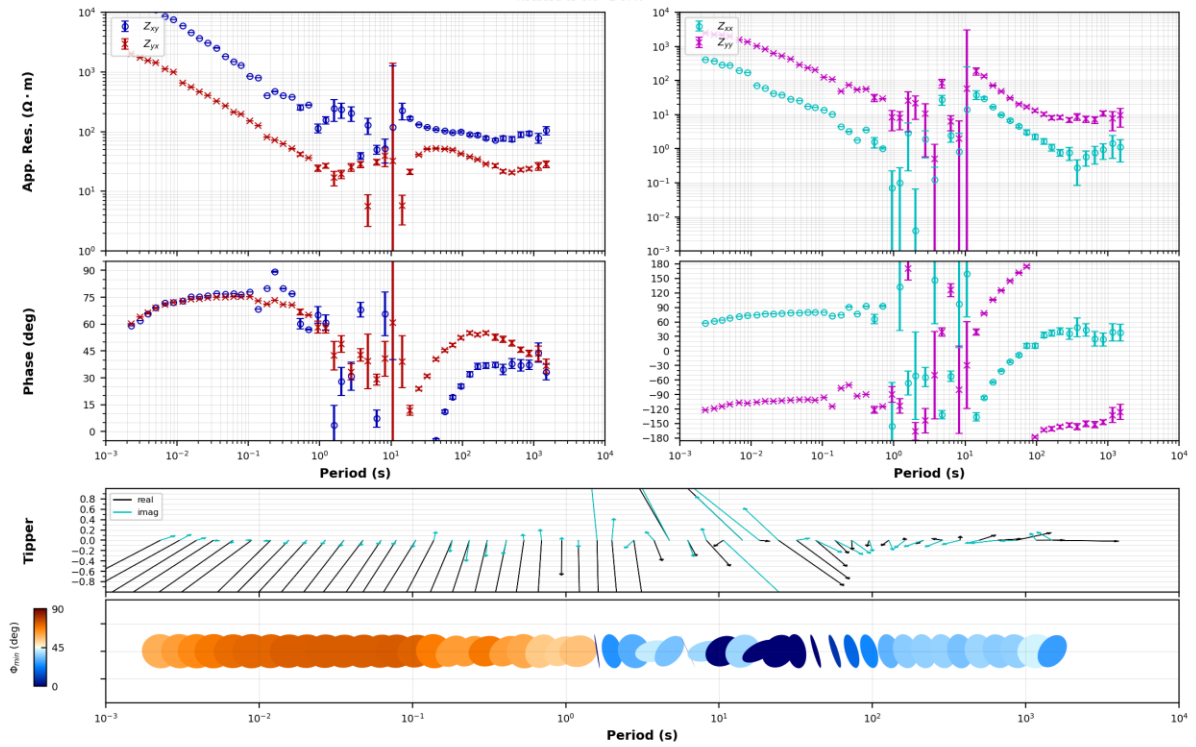
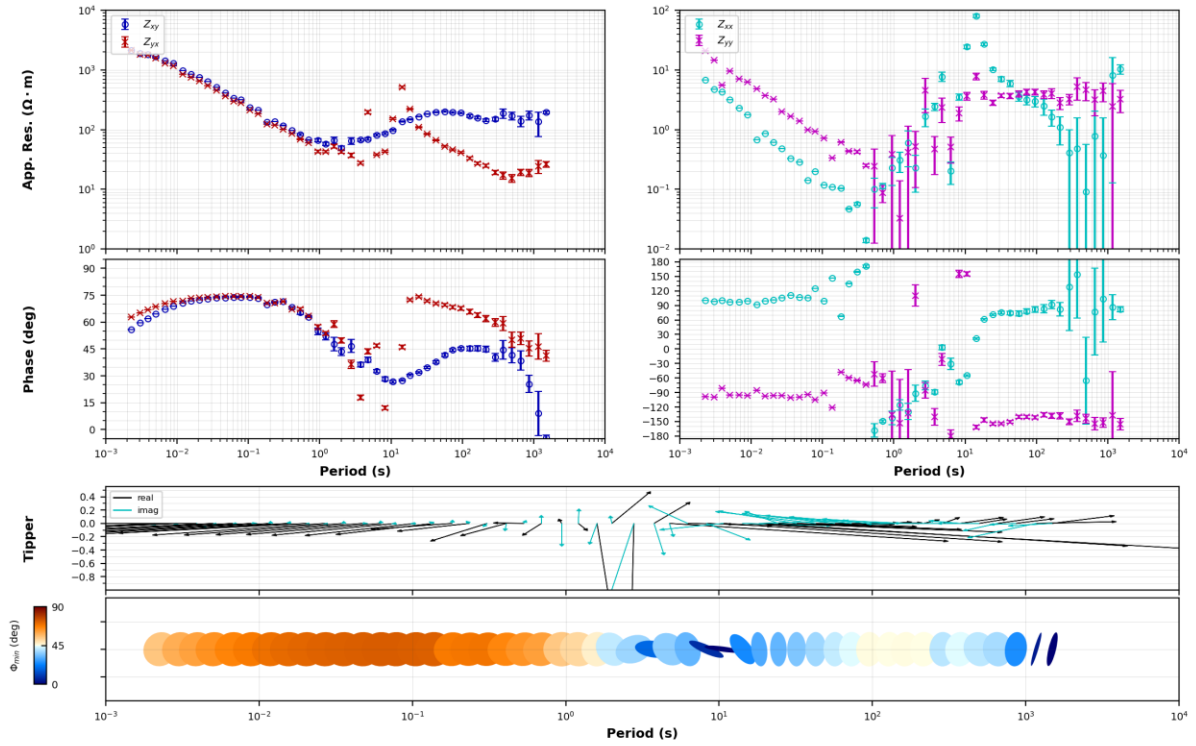


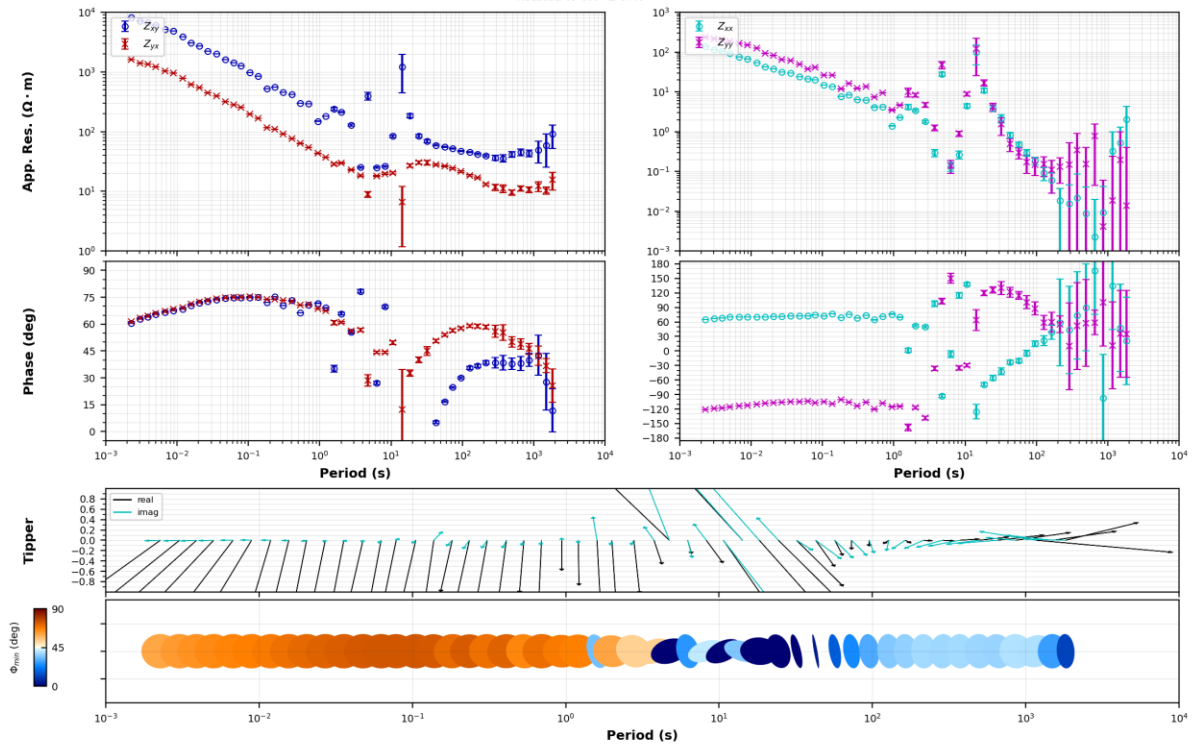
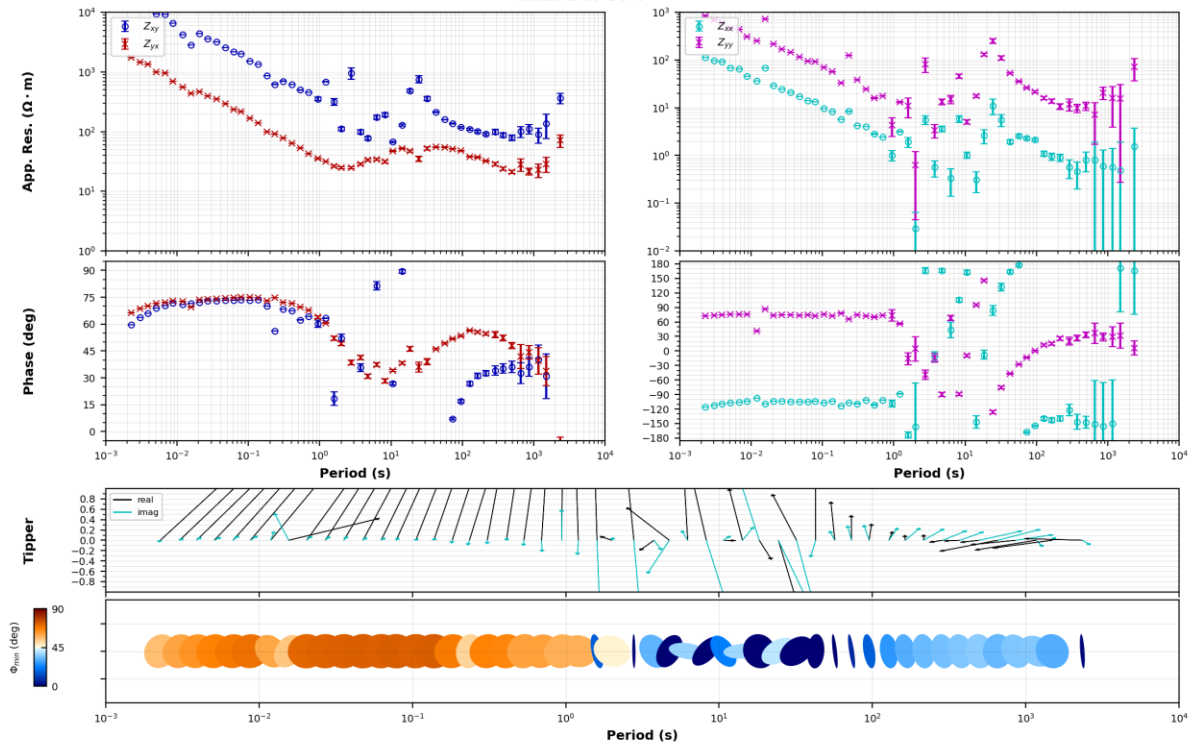
Oregon State University

**NV22061**  
Rotated to 0.0° E of N

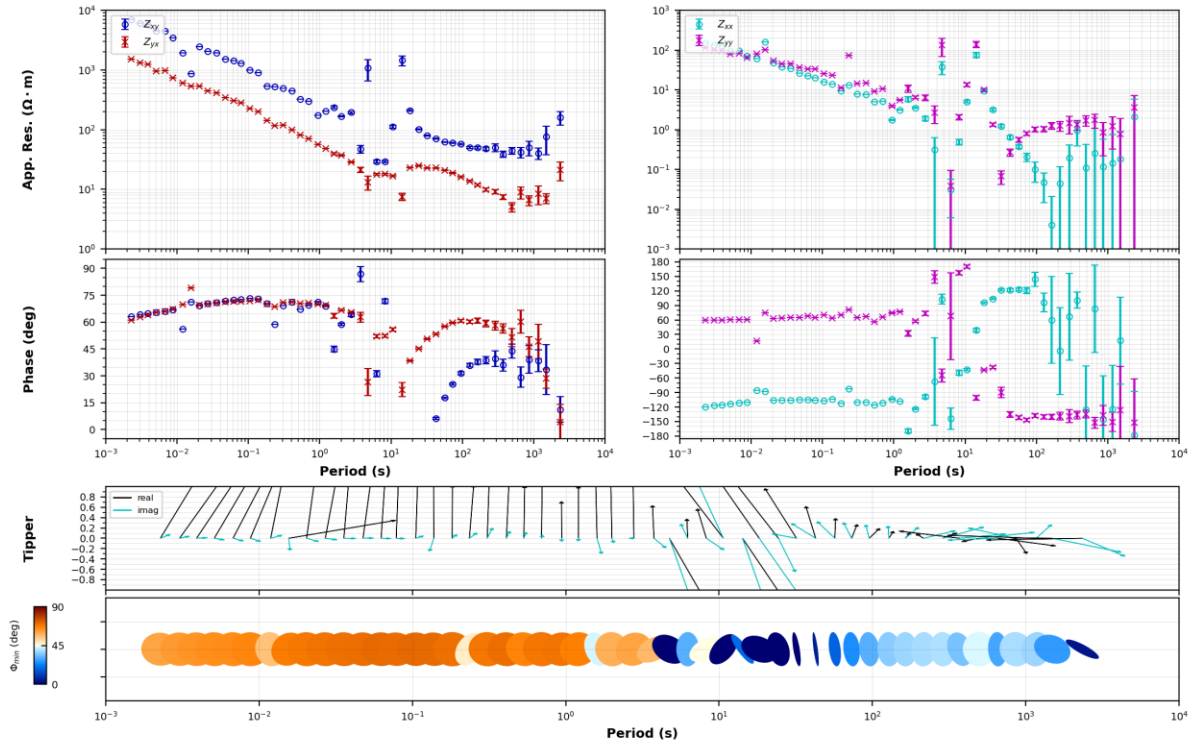
Enthalpion Energy LLC











## Augmented Survey Data Set

Prior to inversion for 3-D density structure, the Complete Bouger Anomaly data set was augmented by legacy data released by previous projects and available through the Geothermal Data Repository. This includes data released by Davenport Newberry, and by the 2012 and 2014 NETL-Oregon State University project to monitor the EGS Demonstrator Project carried out by AltaRock Energy and partners on the West Flank of Newberry Volcano. The station map is seen in Figure 7 on the following page.

The NV22 wideband MT data set was also augmented by a legacy data set obtained from Davenport Newberry, and from the NETL-Oregon State University-Zonge International project to monitor the AltaRock Energy EGS Demonstration Project at the west flank of Newberry Volcano in 2012 and 2014 (Figure 7).

## 3-D inversion of MT and Gravity data

Following the reduction of the gravity data to the CBA, band-pass filtered for antialiasing and to remove regional trends, the CBA data from 237 stations were inverted for 3-D density structure. Following processing of the MT time series data to full tensor impedance and induction vectors (tippers), the data were rotated into geographic coordinates and frequency resampled into 39 frequency bins. Selected frequency bins were notched out if data quality standards were not met, and the full tensor impedance MT data were then inverted for 3-D resistivity structure.

The MT response data as actually inverted is found in EDI format in the final data product release in the Final Product Release > MT Response Data > MT\_PickedForInversion folder.

Following the individual inversion of the gravity and MT data, joint inversion of these data was carried out to yield final 3-D density and resistivity structure models using a set of inverse modeling codes developed by Dr. Xiaolei Tu. The 3-D MT inversion employs an integral equation forward solver that allows for topography at the surface. The 3-D gravity inversion, also allowing for topography, solves for the variation in density around an average value (in this case 2.5 g/cc).

The geographic distribution of the NV22 gravity and MT data sets, augmented by legacy data, is seen in the Figure 7.

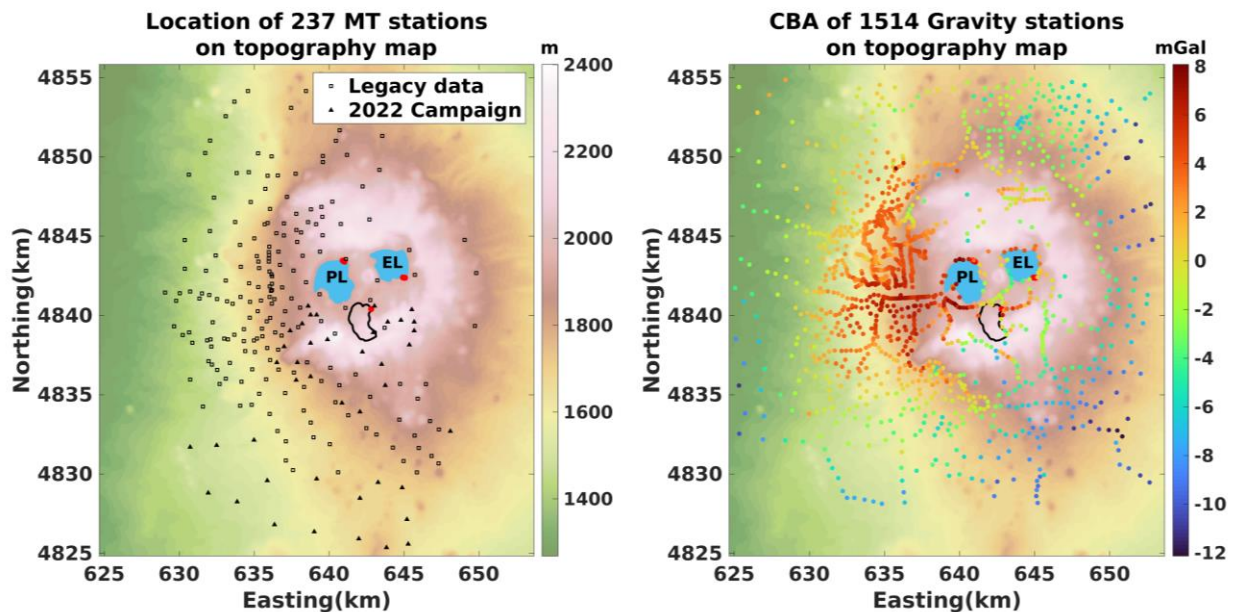


**Figure 7.** Maps showing the locations of the 237 legacy and NV22 wideband MT stations (left) and the Complete Bouguer Anomaly data from 1514 legacy and NV22 gravity stations (right). PL and EL represent Paulina Lake and East Lake, respectively. The polygonal shape outlined in black immediately SE of PL is the boundary of the Big Obsidian Flow (the most recently erupted feature of Newberry Volcano at 1300 ybp) adjacent to the inside of the south caldera rim. The red dots in the map on the left, above, of the CBA show the locations of hot springs at PL, EL, and near the Big Obsidian Flow.

For joint inversion, the following functional was minimized:

$$p(\mathbf{m}_s, \alpha, \beta) = \sum_{j=1}^2 \Phi^{(j)}(\mathbf{m}_s^{(j)}) + \sum_{j=1}^2 \alpha^{(j)} \Psi^{(j)}(\mathbf{m}_s^{(j)}) + \beta s(\mathbf{m}_s^{(1)}, \mathbf{m}_s^{(2)}) \rightarrow \min$$

where  $\alpha^{(j)}$  and  $\beta$  are regularization parameters. The misfit and stabilizer functionals are:

$$\begin{aligned} \Phi^{(j)}(\mathbf{m}_s^{(j)}) &= \left\| W_d^{(j)} \left[ A^{(j)}(\mathbf{m}_s^{(j)}) - d^{(j)} \right] \right\|_{\rho}^2 \\ \Psi^{(j)}(\mathbf{m}_s^{(j)}) &= \left\| W_m^{(j)} (\mathbf{m}_s^{(j)} - \mathbf{m}_{\text{apr}}^{(j)}) \right\|^2 \end{aligned}$$

where  $W_d^{(j)}$  and  $W_m^{(j)}$  denote the data and model weights;  $d^{(j)}$  is the observed data, i.e., gravity field or MT data.  $\| \cdot \|_{\rho}^2$  represents the robust norm.  $A^{(j)}$  represents the forward modeling operator for gravity field or MT impedance. The minimization problem is solved with the reweighted regularized conjugate gradient method (RRCG).

The joint inversion approach works to identify structural features that are in common between the density and electrical resistivity distributions in the models. The specific method employed is referred to as Gramian structural coupling.

Implementation of Gramian stabilizer:

$$s(\mathbf{m}_s^{(1)}, \mathbf{m}_s^{(2)}) = \iiint_D g(\nabla \mathbf{m}_s^{(1)}, \nabla \mathbf{m}_s^{(2)}) dv$$

where  $g(\cdot)$  is the Gramian of the gradient at the position  $\mathbf{r}$ ;  $D$  denotes the inversion domain (Tu & Zhdanov, 2021).

The stabilizer  $s(\mathbf{m}_s^{(1)}, \mathbf{m}_s^{(2)})$  is minimized if the gradients of the two model parameters are parallel at every point in the inversion domain. Minimizing of  $s$  will necessitate the coincidence of structural boundaries of different model parameters.

While there is no requirement, from the perspective of equations of state, for the variations in density and the variations in electrical resistivity to be strictly coincident, experience has shown that coupling the two solutions together through gradient-based approaches helps to stabilize the solutions and to identify real structural boundaries that might otherwise be poorly resolved or missed when inverted for single with only a single type of data set.

The joint and single (individual) inversion results are seen on the following pages. Please note that the models are displayed with depths referenced to mean sea level (MSL). An elevation of 2.4 km above MSL corresponds roughly to the altitude at the top of Paulina Peak, the highest point on the caldera rim, and to 0.5 km above the caldera floor, which is at an elevation of approximately 1.9 km above MSL.

# Resolution Analysis

Our resolution matrices are calculated based on the integrated sensitivity, derived from the Jacobian matrix calculated in the inversion, which contains elements  $\frac{\partial \|d\|}{\partial m}$ , each of which represents the change in the data vector  $d$  with respect to a change in a model element value  $m$ . This is similar to the derivative weight sum (DWS) routinely used by seismologists but more robust. The underlying concept is to measure how sensitive the data as a whole is to the value of physical property (i.e., density or electric resistivity) at each point in the subsurface, which is determined by the data coverage and also by the governing laws of physics.

The power to resolve finer-scale features in the density and resistivity model volumes is calculated from the Jacobian and is displayed in the figures below.

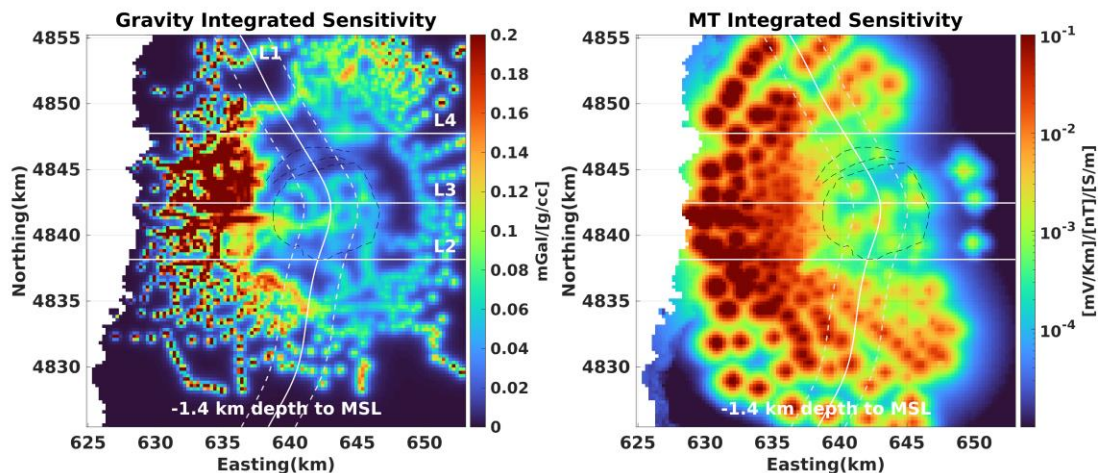


**Figure 8.** Horizontal sections of integrated sensitivity (resolution) matrices at a depth of 1.4 km above sealevel/1 km below Paulina Peak/0.5 km below the caldera floor.

**For Figure 8 and all map figures that follow,** the white curves L1, and white lines L2, L3 and L4 are respectively a broadly S-N arcuate section through the center of the caldera tracing the path of the Walker Rim Fault to the south and the Sisters Fault to the north, a W-E section through the south caldera rim, a W-E section through the center of the caldera, and a W-E section through the north caldera rim. Corresponding vertical sections through the 3-D models will be presented following the horizontal sections maps and discussion.

Referring to the gravity integrated sensitivity on the left-hand side of Figure 8, the cool/bluer colors indicate regions where features are more poorly resolved, and the hotter/red colors are where features are best resolved. The units of sensitivity are mGal per g/cc. Dark red colors indicate that a 1 g/cc change in the density of a feature at this depth will result in a 0.25 mGal gravity signal, while a dark blue region indicates that the same 1 g/cc change in the density of a model feature will produce a much weaker gravity signal with a change that may be near 0 mGal. A 1 g/cc change in the density of a model feature at this depth will therefore be most easily resolved beneath the densely instrumented west flank of the volcano where there are intense warmly colored zones. There is still resolving power along the southwest and southern flanks of



the volcano but diminished along the north and northwest rim at these depths. The situation is similar for the resolvability of resistivity features (units mv/km/nT per S/m change in the resistivity of a model feature at this depth), although the areas of best resolvability are broader given the different governing laws for MT to those of gravitation.

Resolution matrices for three other horizontal depth sections appear below.

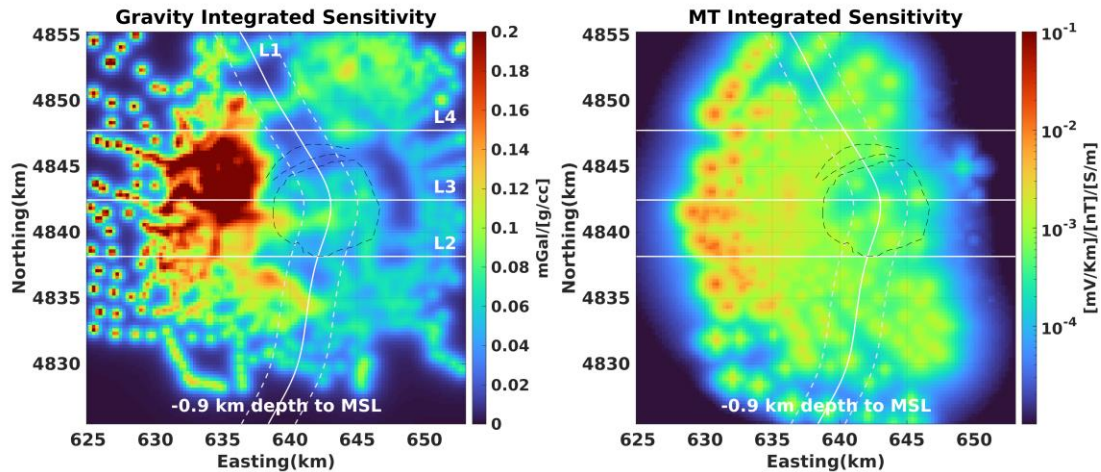


**Figure 9.** Horizontal sections of integrated sensitivity (resolution) matrices at a depth of 0.9 km above sea level/1.5 km below Paulina Peak/1.0 km below the caldera floor

At this somewhat greater depth, the ability to resolve finer scale features is diminished somewhat, but the area over which there is good resolving power is also broadened, to cover nearly all of the aperture of the survey arrays. This persists to greater depths as seen below.

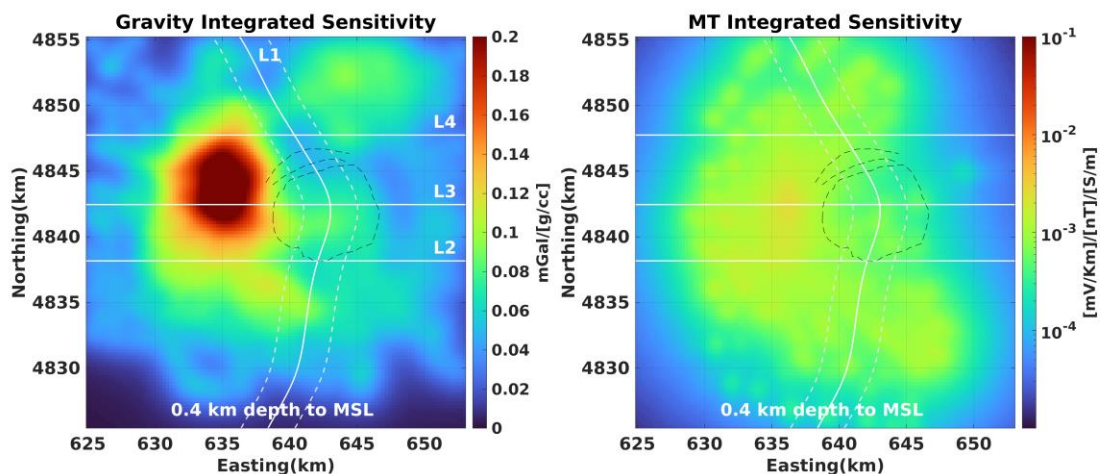


**Figure 10.** Horizontal sections of integrated sensitivity (resolution) matrices at a depth of 0.4 km above sea level/2.8 km below Paulina Peak/2.3 km below the caldera floor

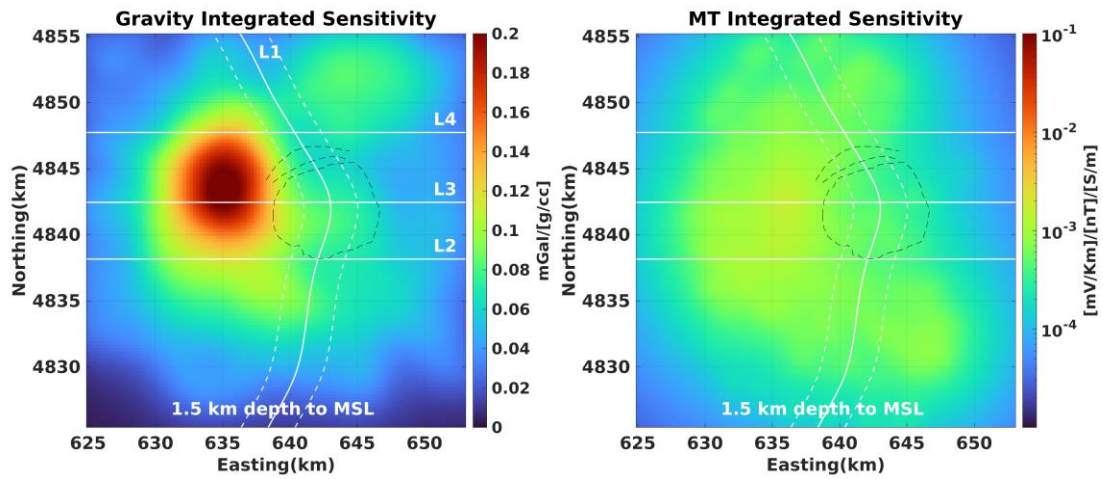


**Figure 11.** Horizontal sections of integrated sensitivity (resolution) matrices at a depth of 1.5 km above sea level/3.9 km below Paulina Peak/3.4 km below the caldera floor

## Horizontal sections of jointly inverted models

On the pages that follow we present horizontal sections of the resistivity and density models from the joint inversion. As repeated in the section below, for the models presented the grid-shaded areas in the model denote regions of the model with resolving power that falls below a minimum threshold.

For the density model a region of the model is considered adequately resolved if a 1 g/cc change in a model feature at a given depth produces a 0.01 mGal change in the gravity data. For the resistivity model that threshold is reached when a decade resistivity change (i.e., from 0.1 S/m to 1 S/m) in a model feature at a given depth produces a 0.001 mv/km/nT change in the MT data.

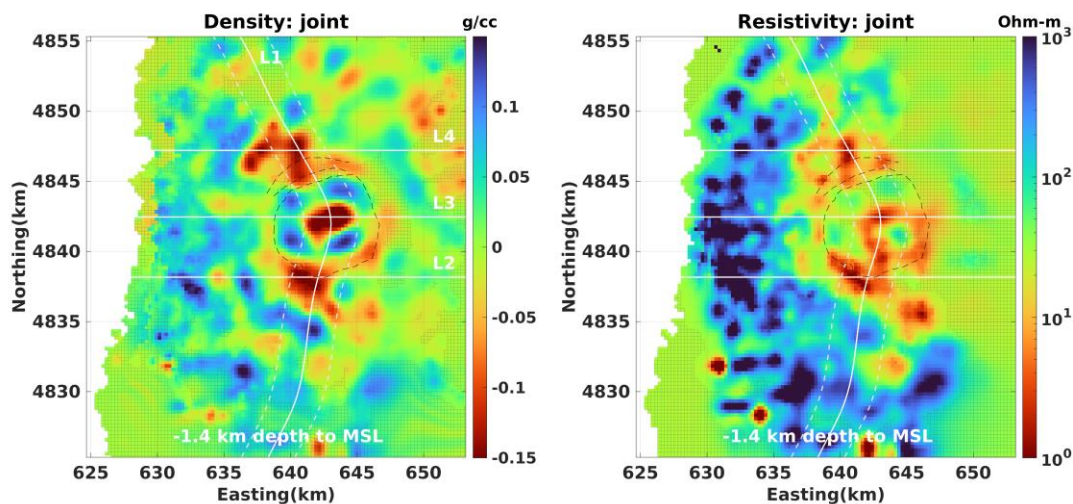


**Figure 12.** Horizontal sections of joint inverted models at a depth of 1.4 km above sea level/1 km below Paulina Peak/0.5 km below the caldera floor. Areas of low resolution are shaded with gray grids.

The irregular white area on the extreme left of each map in Figure 12 identifies parts of the surface of the volcanic edifice with elevations lower than the 1.4 km above MSL reference level for this map section. The grid-shaded areas found mainly on the periphery of each model section are areas of lower resolving power as revealed through analysis of the Jacobian matrix from the joint inversion.

Features within the caldera itself, the northwest rim and west flank and the south rim and south flank of the volcano are well resolved in both density and resistivity for this depth section.

The density scale from -0.15 to 0.15 g/cc is for density relative to the average of 2.5 g/cc. The electrical resistivity is shown on a  $\log_{10}$  color scale, with deep red areas being highly conductive, and deep blue areas highly resistive.

For this depth section the primary features seen are interpreted as surface rubble, brecciated material, caldera infill and surface volcanics. The prominent low relative density and low



resistivity feature near the center of the caldera is associated with caldera infill and shallow hydrothermal features. There are hot springs in the two caldera lakes, and temperature wells in the caldera show highly elevated temperatures at these depths near the low resistivity feature near the south caldera rim near the Big Obsidian Flow.

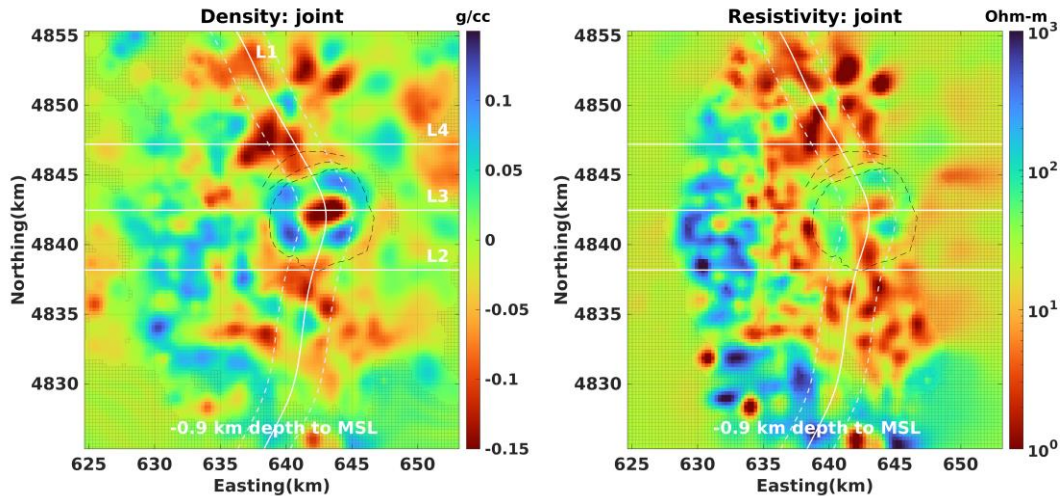


**Figure 13.** Horizontal sections of jointly inverted models at a depth of 0.9 km above sea level/1.5 km below Paulina Peak/1.0 km below the caldera floor. Areas of low resolution are shaded with gray grids. The roughly circular dashed curve represents the caldera rim.

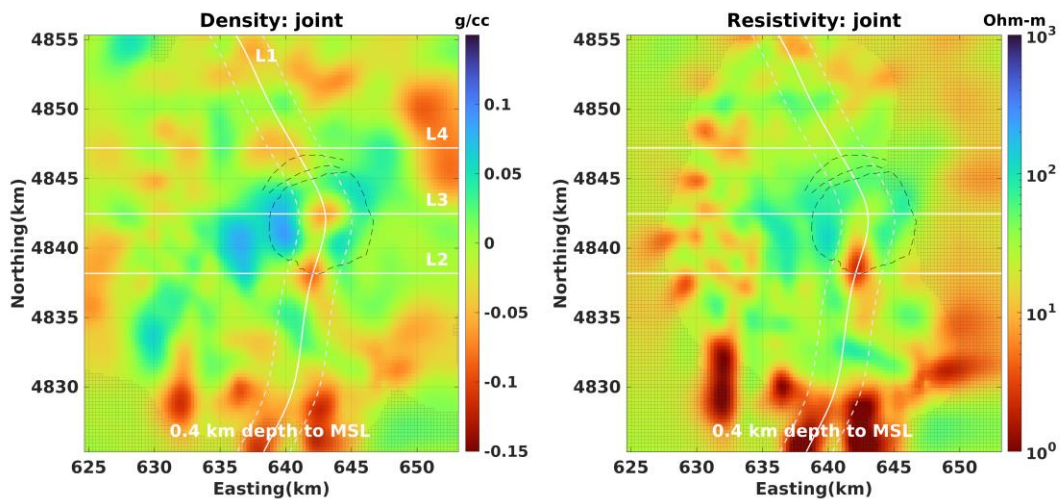


**Figure 14.** Horizontal sections of joint inverted models at a depth of 0.4 km above sea level/2.8 km below Paulina Peak/2.3 km below the caldera floor. Areas of low resolution are shaded with gray grids.

Here we see the complexity of the surface volcanics and alteration and deposition products (clays, chlorites) on the west flank giving way to the deeper, denser and more resistive transition to the underlying pluton. In the caldera the low-density feature associated with shallow collapse infill and hydrothermal systems is still present but less pronounced. The low resistivity feature corresponding to this has largely diminished. On the south rim a low density, low resistivity

feature beneath the Big Obsidian Flow and begins to show an association with an extension south along the south flank of the volcano.

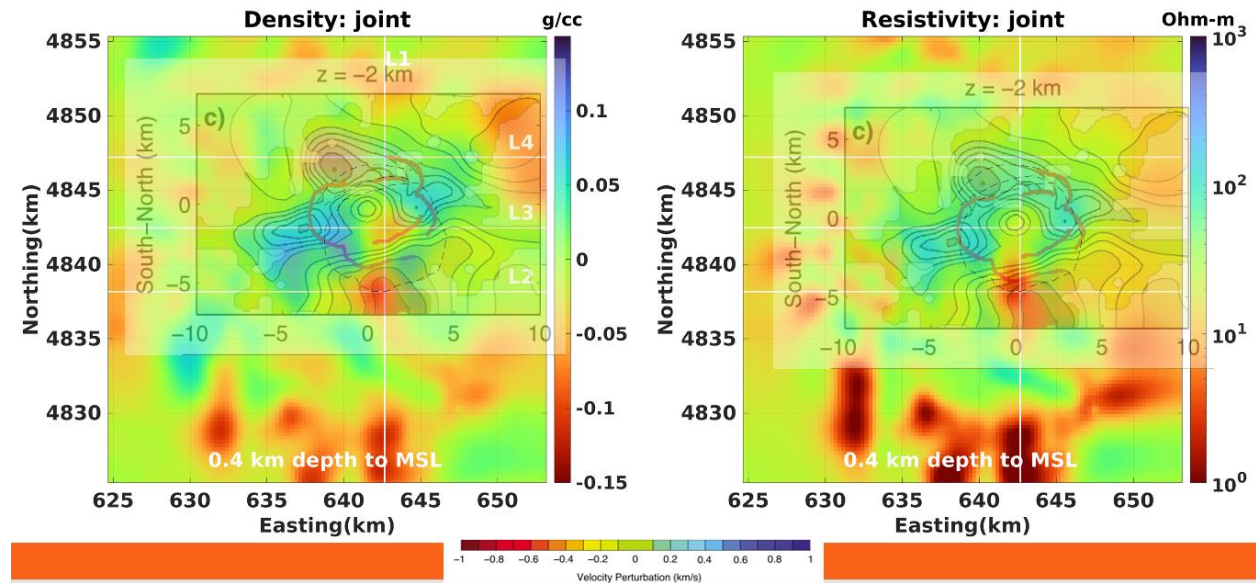


**Figure 15.** Overlay of seismic velocity model on jointly inverted density and resistivity models at a depth of 0.4 km above sea level. The Vp model is from Beachly et al., 2012 doi:10/1029/2012JB009458.

By referring to the density and resistivity maps without the P-wave velocity overlay in Figure 14, it is apparent that the low density, low resistivity feature that extends beneath the south flank of the volcano closely matches the footprint of the slow Vp feature in Beachly et al.'s seismic tomogram shown in Figure 15. The feature is seismically slow, lower than average density, and conductive at this depth of approximately 2.3 km below the caldera floor.

Also take note of the finger-like low relative density, low resistivity features along the southern margins of the models. One should view features at the edge of the data array from a 3-D MT inversion with caution, since edge effects related to whatever boundary conditions have been set on the forward solution can generate anomalous or poorly defined model features. What is striking here is that the same features are also seen in the density model. As seen later, this is also the case in the density model produced by inverting the gravity data alone with no constraints from the MT data. This coincidence of features – lower than average density, highly conductive is noted for discussion later.



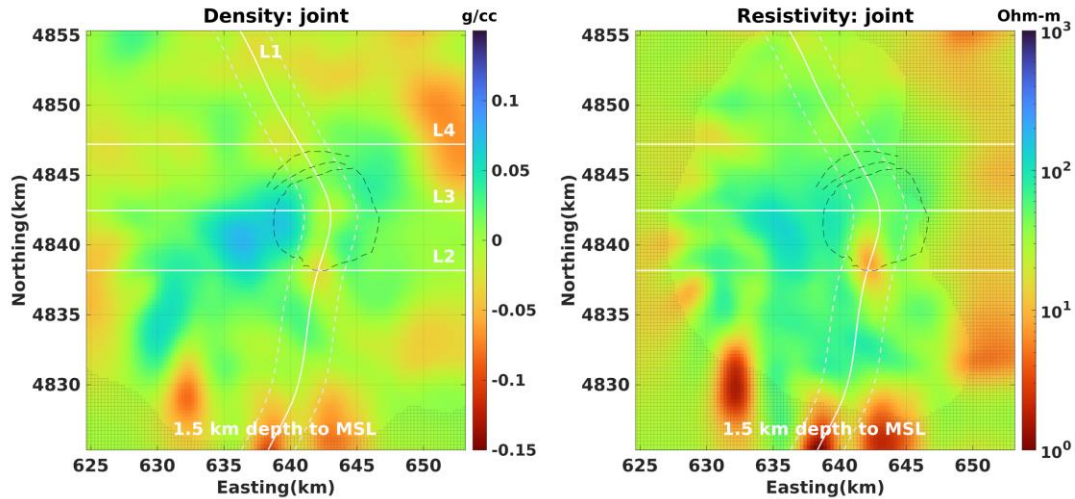


**Figure 16.** Horizontal sections of joint inverted models at a depth of 1.5 km above sea level/3.9 km below Paulina Peak/3.4 km below the caldera floor. Areas of low resolution are shaded with gray grids.

The denser than average, more resistive zone on the west flank, associated with the impermeable pluton underlying the EGS lease unit is evident from the caldera edge west to an easting of approximately 635 km, between northing 3838 km and 4844 km. The low-density zone beneath the caldera center associated with the seismic low velocity feature is barely detectible, and there is essentially no resistivity signature of the feature at these depths. Conversely, there is still a strong low resistivity and detectible low relative density zone associated with the south caldera rim/south flank anomaly. The low relative density, low resistivity finger-like features persist along the southern margins of the model. The resolution analysis of the Jacobian matrix indicates that the southern finger-like low density features are well resolved, and they are marginally resolved – primarily at their northernmost extent, as low resistivity zones.

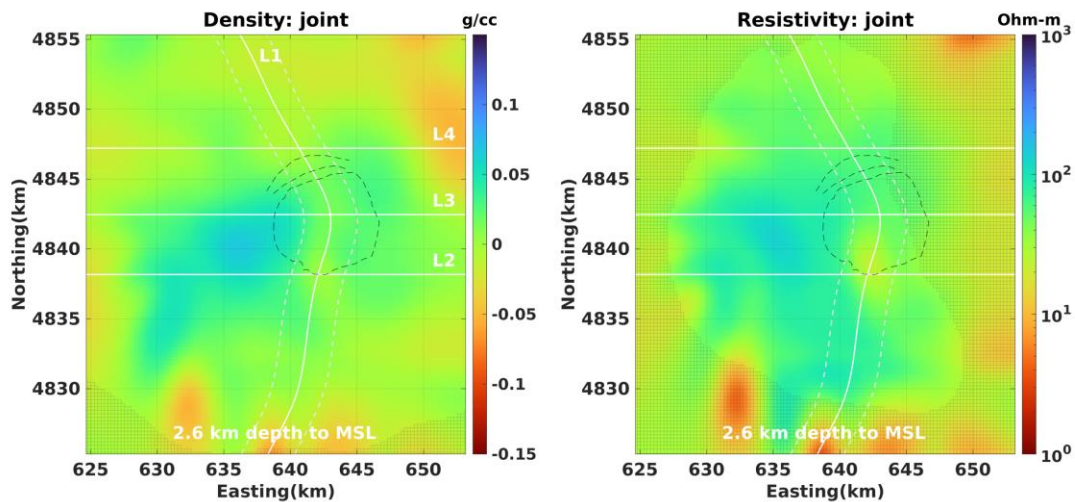


**Figure 17.** Horizontal sections of joint inverted models at a depth of 2.6 km above sea level/5.0 km below Paulina Peak/4.5 km below the caldera floor. Areas of low resolution are shaded with gray grids.

Figure 17 is similar to the previous depth section shown in Figure 16, but density and resistivity anomalies are nearly at background levels.

## Vertical sections of jointly inverted models

With reference to the horizontal model sections shown previously, the following plots are vertical sections through the 3-D density and resistivity model volumes. Immediately below we show the profiles along the L1 curve that arcs from southwest to northwest along the Walker Rim Fault, past the cinder cone in the caldera dividing the two caldera lakes, and then through the Sisters Fault along the north-northwest rift zone.

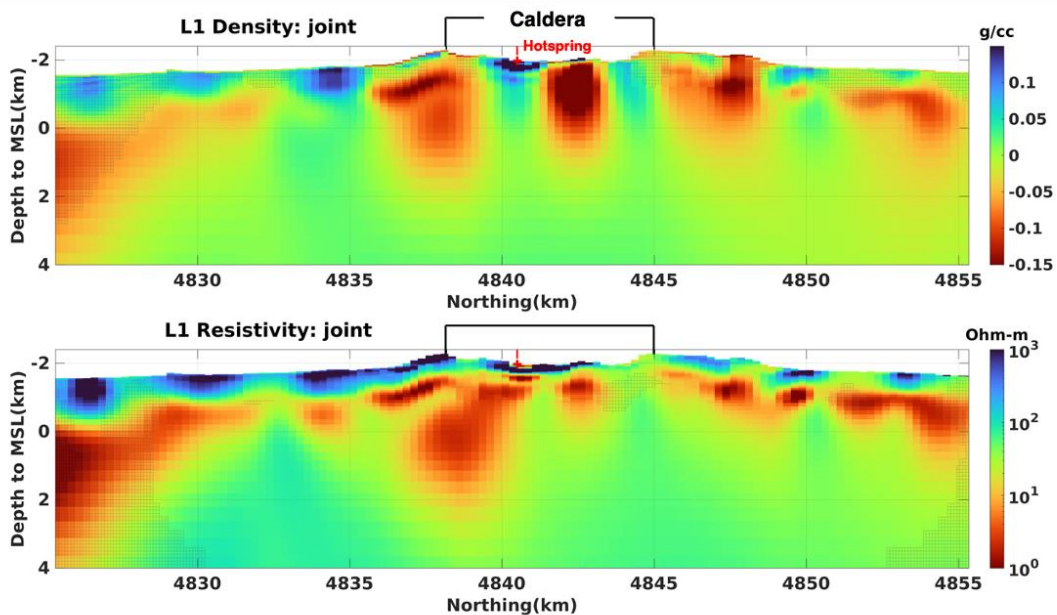


**Figure 18.** Vertical profiles of jointly inverted models along the L1 arc that runs from southwest to northwest through the center of the caldera. Areas of low resolution are shaded with gray grids. The red cross denotes the location of a hot spring adjacent to the Big Obsidian Flow.

The cinder cone separating East Lake from Paula Lake in the center of the caldera is located at approximately a northing of 4843 km; the south caldera rim at 4837.5 km, and the north caldera rim at 4845 km. Beneath the center of the caldera floor at shallow depth and extending to nearly 1 km MSL there is a prominent low relative density zone that we associate with caldera infill. This is surrounded by an annulus of higher relative density material that is likely associated with dacitic dike structures. A low relative density zone is found on both south and north flanks, although it is most pronounced beneath the south flank where it appears to be connected to a structure that continues to and deepens to the southern edge of the model.

The resistivity section shows a conductive zone at shallow depths beneath the center of the caldera, but extending only to ~-0.5 km MSL, or 1.5 km shallower than the low relative density

zone. This may be associated with caldera infill and the hydrothermal features seen in and below the caldera lakes. The resistivity section closely matches the density section on the south and north flanks, with a prominent conductive feature under the south rim that appears to shallow inside the caldera near the edge of the Big Obsidian Flow and that deepens to the south where it appears to be connected to the highly conductive, low relative density feature that extends to the edge of the model volume. The hachured areas indicating zones of relatively poor resolving power intrude on the southern edge of this feature, but it remains well resolved as far south as northing 4828 km in the resistivity section and northing 4824 km in the density section.

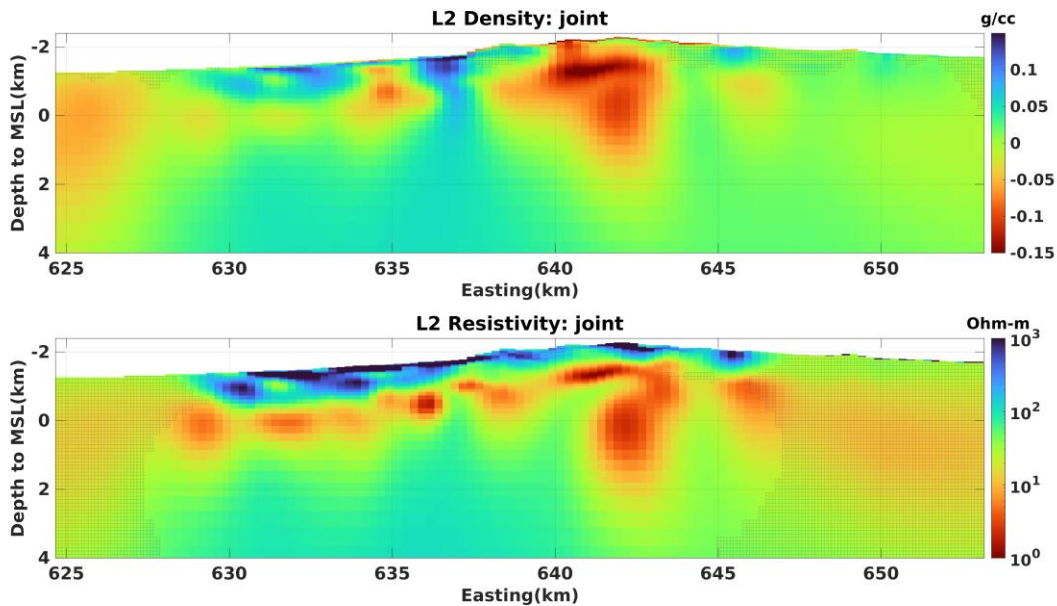


**Figure 19.** Vertical profiles of joint inverted models along the L2 line that runs from west to east crossing the south caldera rim. Areas of low resolution are shaded with gray grids.

In the west-to-east vertical section in Figure 19 that crosses the south caldera rim, the highest point along the south caldera rim is at easting 642 km. This is immediately east of the trace of the Walker Rim crustal fault that intersects the volcano from the southwest. The prominent low relative density, low resistivity feature is found adjacent to and in this area with the deepest part of the feature extending to a depth of 2 km MSL along this profile.



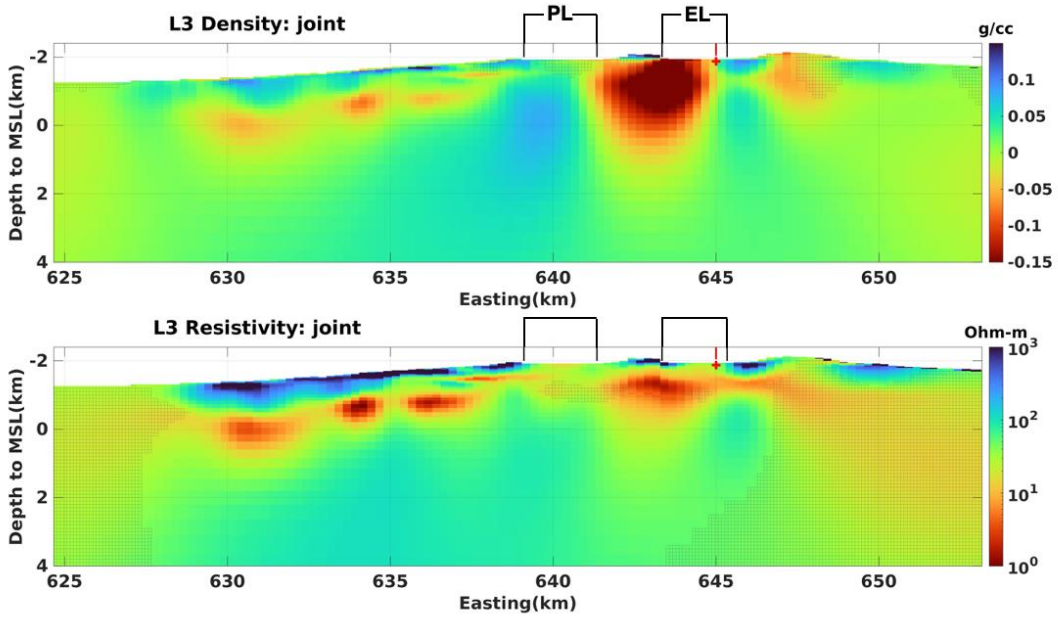


**Figure 20.** Vertical profiles of joint inverted models along the L3 line that runs from west to east through the caldera center. Areas of low resolution are shaded with gray grids.

In the section shown in Figure 20, a profile from west-to-east across the center of the caldera, the low relative density zone seen in the center of caldera in the horizontal map depth sections is evident, surrounded by higher density dike zones. The low resistivity zone is coregistered with this (at eastings of 642-645 km) although, as before, it doesn't extend to as great a depth and its horizontal boundaries are not too well resolved.

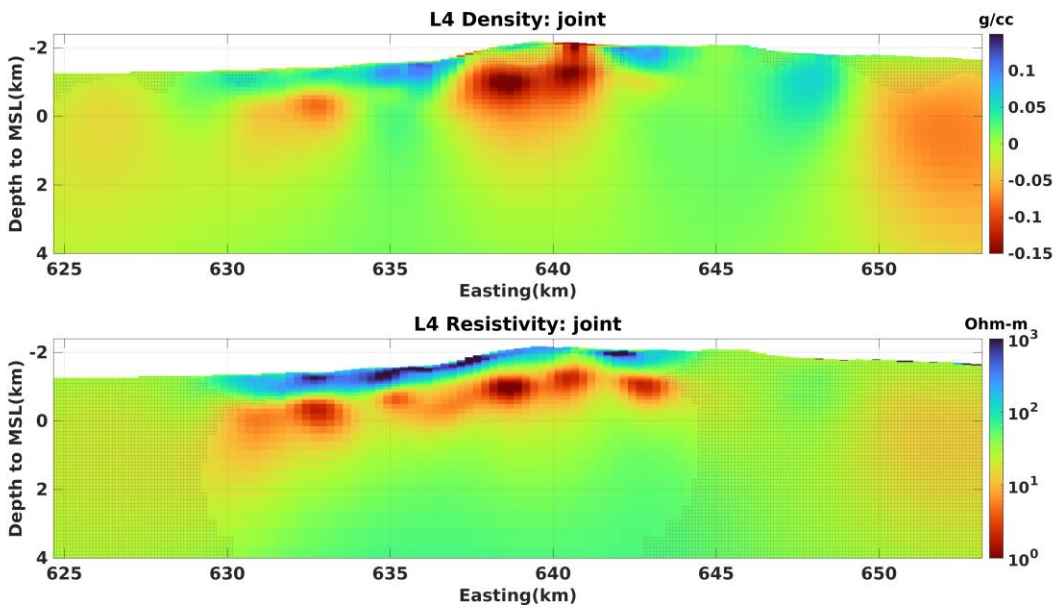


**Figure 21.** Vertical profiles of joint inverted models along the L4 line that runs from west to east through the north caldera rim. Areas of low resolution are shaded with gray grids.

The sections in Figure 21 run from west-to-east across the north caldera rim. Here we see the coincidence of well resolved low relative density, low resistivity zones at relatively shallow depths extending to ~0 km MSL. This area is in the transition between the caldera and the north rift zone with recently erupted features evident on the surface. In contrast to the south caldera rim profile, there are no deeper low density, low resistivity features in this section. Interpretation of the shallow features along the north rim profile is difficult in the absence of other data. These features may be associated with underlying melt, with hydrothermal systems or groundwater, and with hydrothermal alteration products.



## Comparison of separately and jointly inverted models

While the power of the joint inversion to identify common structures between the density and resistivity features in the data has proven informative, since gradient methods to find structural commonalities are ad hoc rather than driven by a requirement from underlying equations of state, the question is correctly asked if such a method introduces structural links that are not strictly required by the data.

To examine this question, we have also inverted the gravity (CBA) data singly, without reference to the MT data, and we have done the same for the MT data, and we've compared the single inversion to the joint inversions. A set of such comparisons follows immediately below.

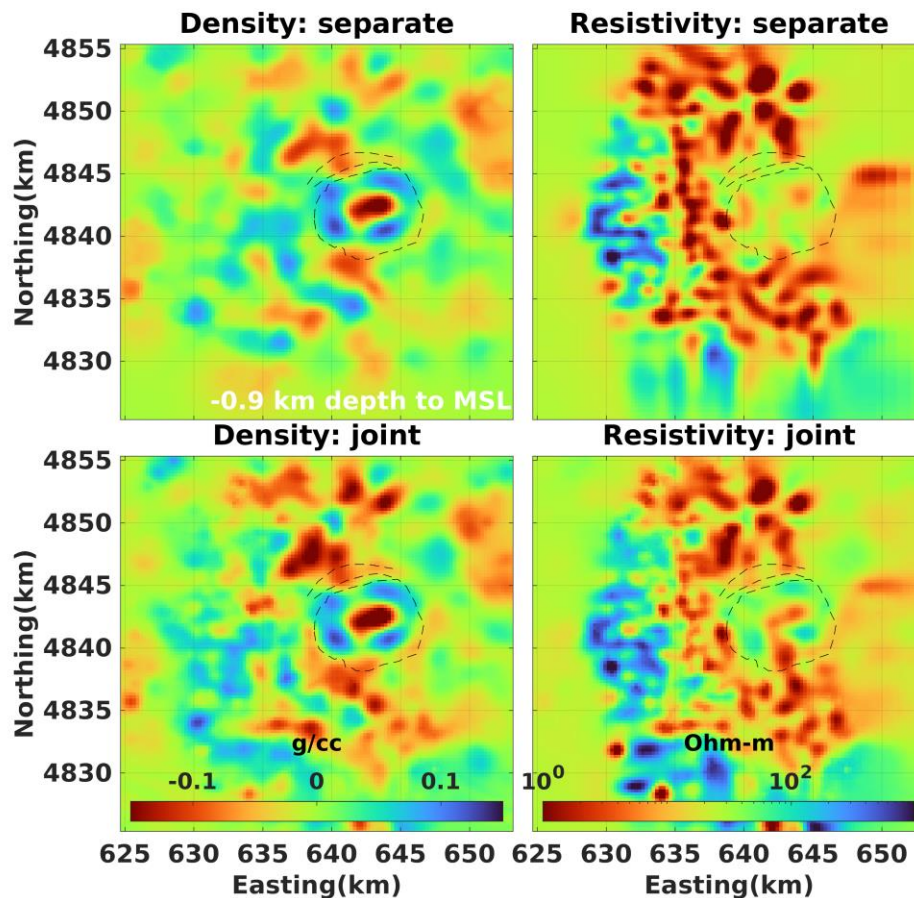


**Figure 22.** Horizontal sections of separately and jointly inverted models at a depth of 0.9 km above sea level/1.5 km below Paulina Peak/1.0 km below caldera floor

As is evident in Figure 22, there is modest impact of the joint inversion on the density and resistivity structures obtained by inverting the gravity and MT data separately. The conductive feature in the caldera in the separate resistivity model is better defined and localized in the jointly inverted model, with a clearer connection to the conductive feature extending south to and past the south caldera rim. There is only marginal impact on the density model.

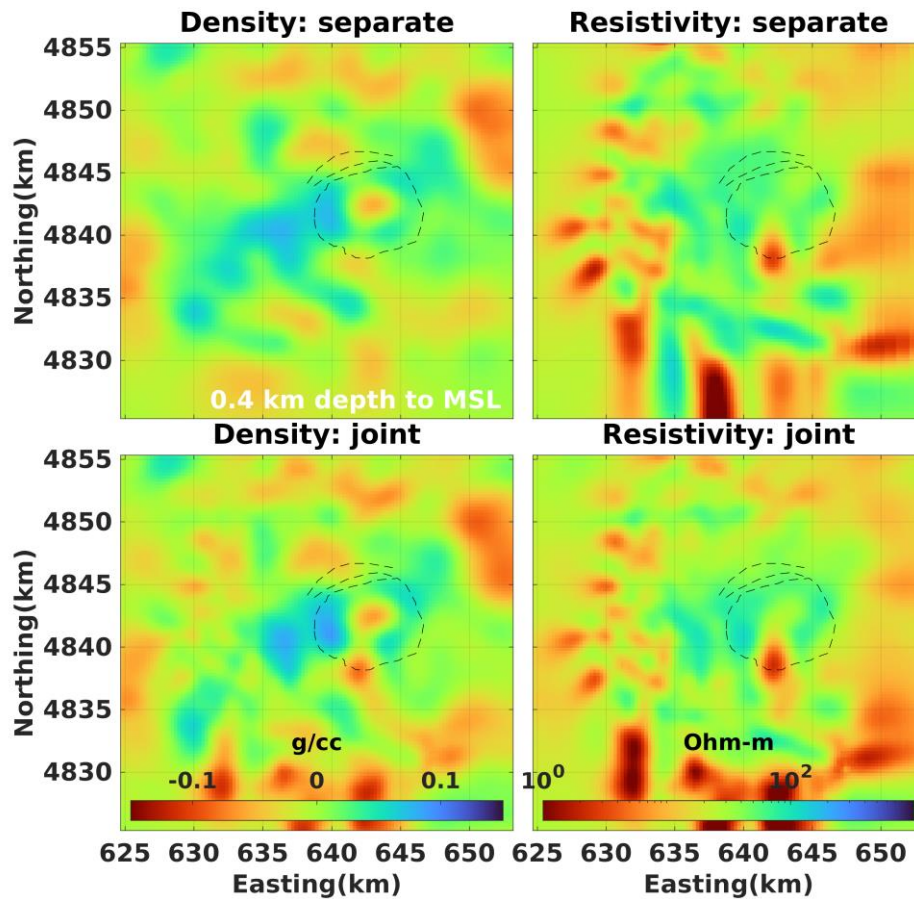


**Figure 23.** Horizontal sections of separately and jointly inverted models at a depth of 0.4 km above sea level/2.8 km below Paulina Peak/2.3 km below the caldera floor

In the example in Figure 23, the joint inversion has a marginal impact on the resistivity structure near the caldera and south caldera rim and flank, but on the southern margins of the model volume the N-S distinctly finger-like conductive structures in the separate inversion are seen to resemble the distinct but less vertically oriented, more lobate features seen in the density model. This likely results from the relatively poor resolving power of the MT data along the southern boundary of the model volume – the data are equally well fit by either version of the resistivity anomaly in that area. There is a small influence of the MT data on the resistivity volume in the joint inversion near the south caldera rim and flank, with the joint inversion improving the delineation of the low-density, low resistivity anomaly beneath that area at these depths.

Comparisons between the separate and joint inversions for the vertical model sections along the south caldera rim and through the center of the caldera are seen on the pages following.

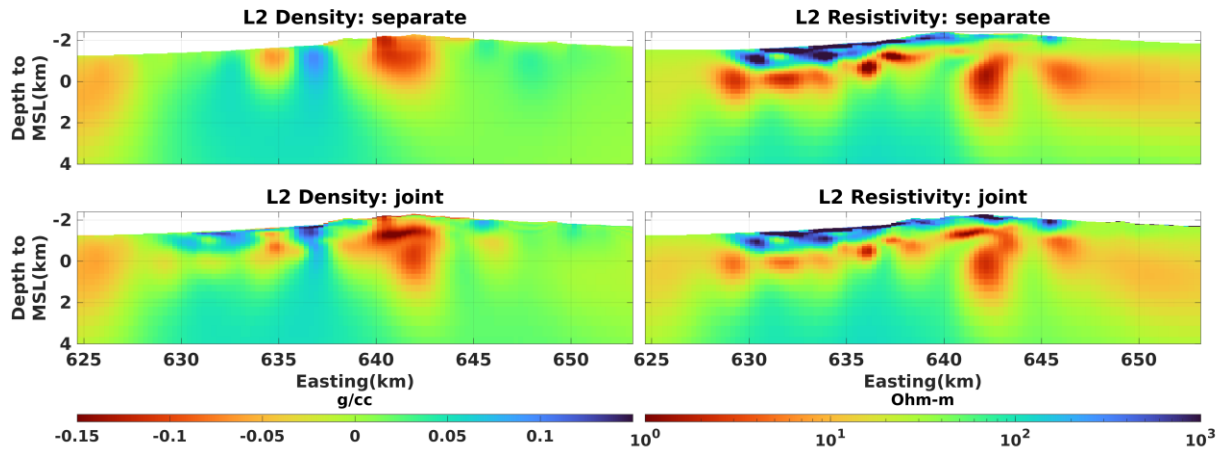


**Figure 24.** Vertical sections of separately and jointly inverted models along profile L2 running west to east across the south caldera rim

In Figure 24, the separately (top) and jointly (bottom) inverted model sections along the west-to-east profile intersect the south caldera rim. The main impact of the joint inversion is to extend the low-density anomaly beneath the south caldera rim to slightly greater depths.

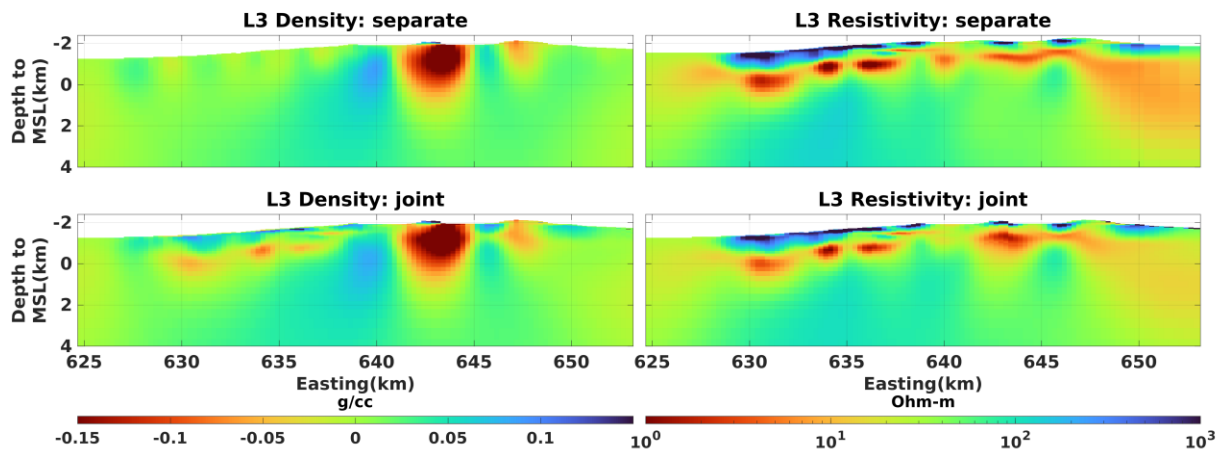


**Figure 25.** Vertical sections of separately and jointly inverted models along profile L3 running west to east across the caldera center

Along the west-to-east L3 profile in Figure 25 that intersects the center of the caldera, the main impact of joint inversion is to remove isolated pockets of somewhat lower than average density in the near surface on the western part of the west flank (Eastings between 630 and 639 km) and replace them with a nearly contiguous, thinner and better defined low relative density feature that deepens to the west.

# Fit of the jointly inverted models to the data

On the following pages, the fit of the jointly inverted models to the data is shown.

## Fit of the Gravity CBA data from joint inversion:

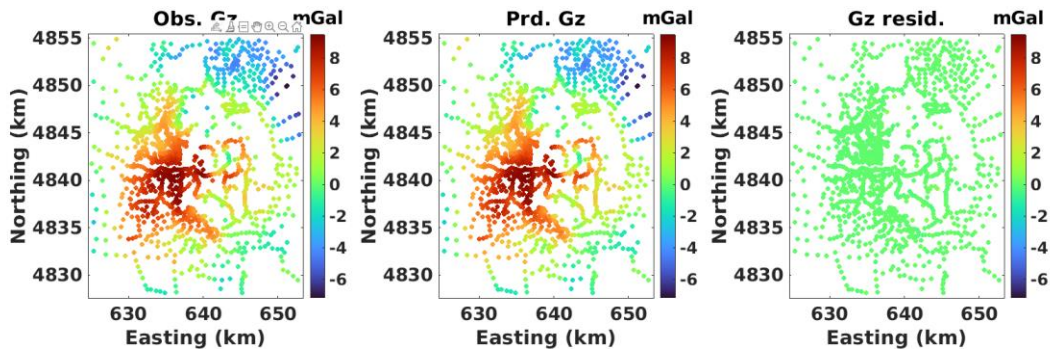


**Figure 26.** Data fit maps of the gravity CBA data from joint inversion. Observed (Obs.), predicted (Prd.) data and data residuals (resid.) are presented in the left, middle, and right panels respectively.

The 3-D density models produced by joint inversion have yielded data-model misfits (residuals) close to 0 mGal at all gravity stations, an excellent fit.

## Fit of the MT data from joint inversion:

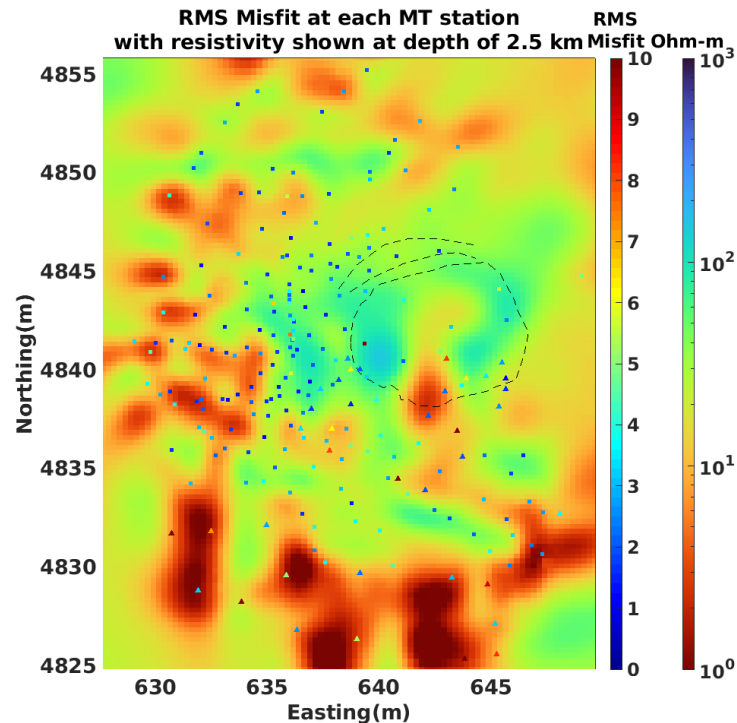


**Figure 27.** RMS maps of the MT data overlaid on a resistivity section at a depth of 2.5 km

The RMS misfit across all MT stations and frequencies is 1.7. Theoretically, the statistical expectation for MT data with completely unbiased confidence limits and no data contamination with non-plane wave MT signal sources, the expected RMS misfit would be 1.0. In practical applications where a 5% error floor to the data is applied (as is typically done), for 3-D MT inversions it is quite rare to achieve an RMS misfit, that approaches  $RMS=1.0$ . An RMS misfit of 1.7 is in practice an excellent misfit.

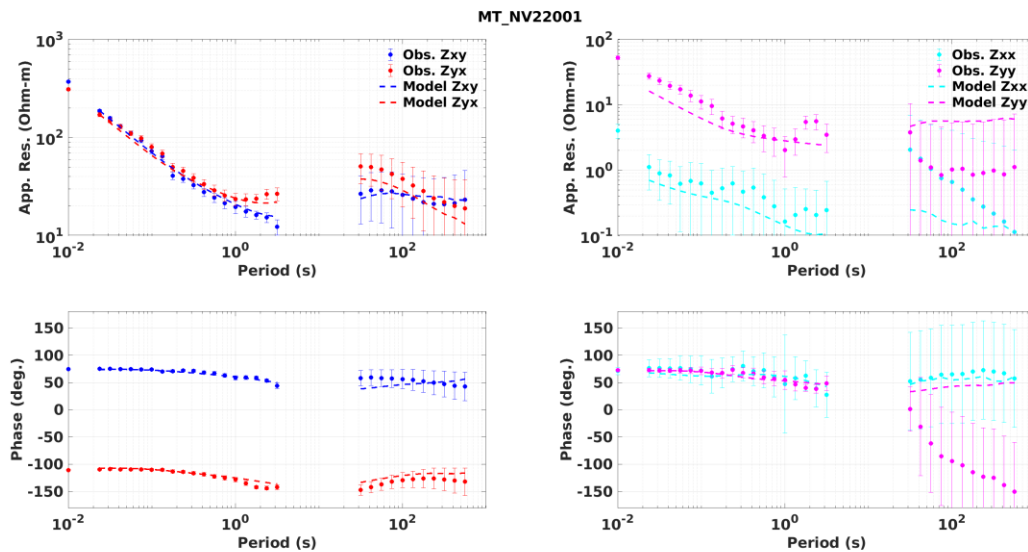
We have also calculated the RMS misfit locally, considering data individually at each station, where the misfit value is the RMS misfit between the joint inverse model's response and the observed data at the station across all frequencies, but only for that individual station rather than globally for all of the stations. We display the local RMS misfits in the map on the previous page as a series of triangles that are color coded. Dark blue triangles represent local RMS misfits near 1.0, pale blue RMS misfits from 3-4, and red RMS misfits of 7 and above. The local misfit triangles are displayed on a horizontal section map of the resistivity at a depth of 2.5 km MSL. The overwhelming majority of stations show low RMS misfits in the blue range, with only a handful of stations in the warmer, higher RMS misfit range. We find that larger local misfits can occur near very sharp changes in resistivity structure, particularly if there is insufficient station density or if the model discretization in the inversion is too coarse. At nearly every site we see good fits to the data.



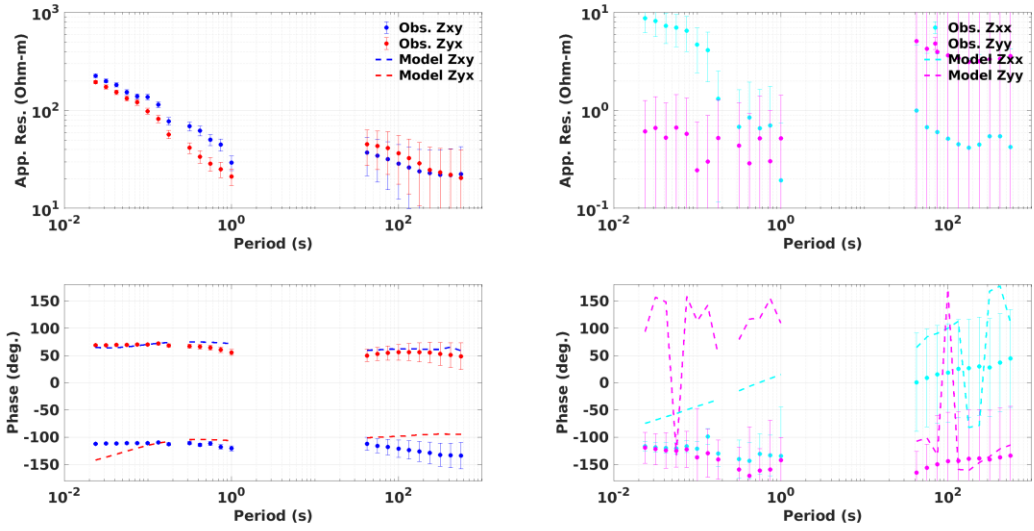
## Fit of the jointly inverted resistivity model response to the MT data

The fit of the MT inverse model to the data is displayed on the following pages showing the four complex, frequency dependent elements of the MT impedance tensor  $Z_{xx}$ ,  $Z_{xy}$ ,  $Z_{yx}$ ,  $Z_{yy}$  scaled into the real valued, frequency dependent apparent resistivity (units: Ohm-m) and phase (units: degrees). The observed apparent resistivity and phase is plotted with standard errors and the data have been resampled onto a uniform set of frequencies. Where data quality within a given frequency band falls below minimum standards (most typically within the long-period MT dead-band, but also near 8 s period where the plane wave assumption used for MT can be invalidated by ionospheric Schumann resonances, or in a limited number of cases at other frequencies), the data were omitted and not used in the inversion.

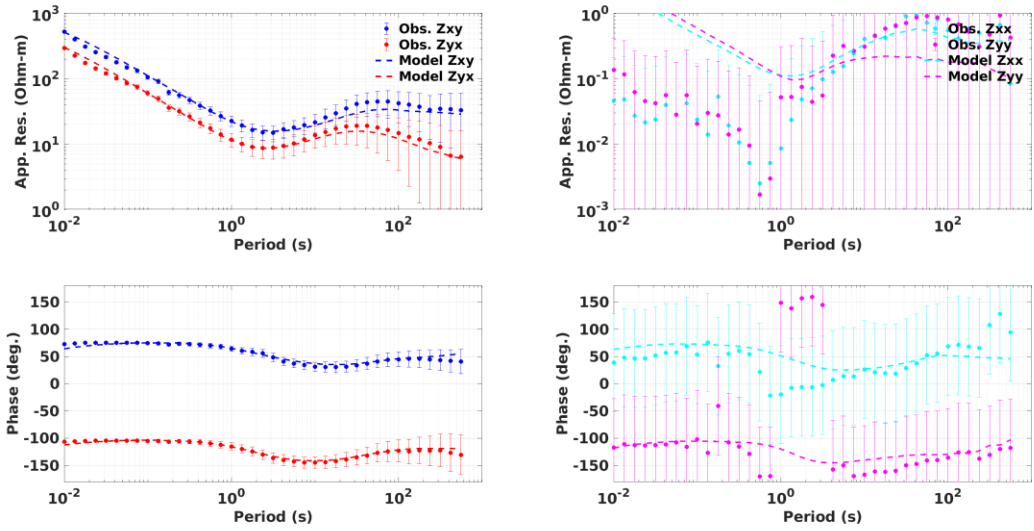
It should be noted that the  $Z_{xy}$  and  $Z_{yx}$  elements of the impedance tensor (also for the apparent resistivity and phase derived from the impedance) are considered the dominant elements. For electrical resistivity structure that varies with depth only (i.e. 1-D structure),  $Z_{xy} = -Z_{yx}$  and  $Z_{xx}$ ,  $Z_{yy}$  are undefined. For structure that varies with depth but also laterally, but that can be rotated into two principal geoelectric directions so that for any given station in one principal direction the geoelectric structure does not vary laterally and in the other direction it does (i.e. 2-D structure),  $Z_{xy} \neq Z_{yx}$  and  $Z_{xx}$ ,  $Z_{yy}$  are undefined.  $Z_{xx}$  and  $Z_{yy}$  are only defined when the geoelectric structure varies on all three dimensions. It is typically the case, even for 3-D structure, that the apparent resistivity and phase for  $Z_{xx}$  and  $Z_{yy}$  are less smooth and have larger confidence limits than those for  $Z_{xy}$  and  $Z_{yx}$  elements.



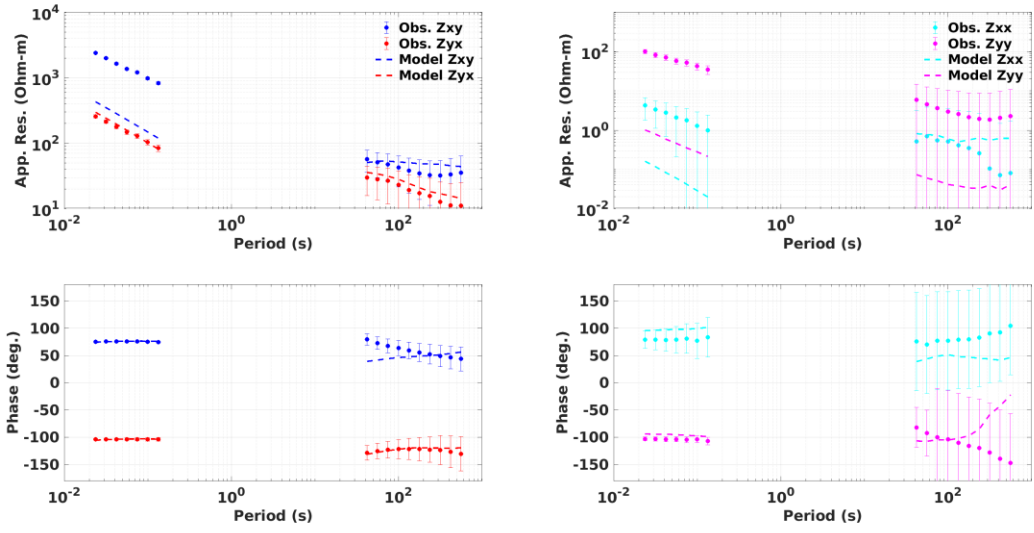
MT\_NV22002



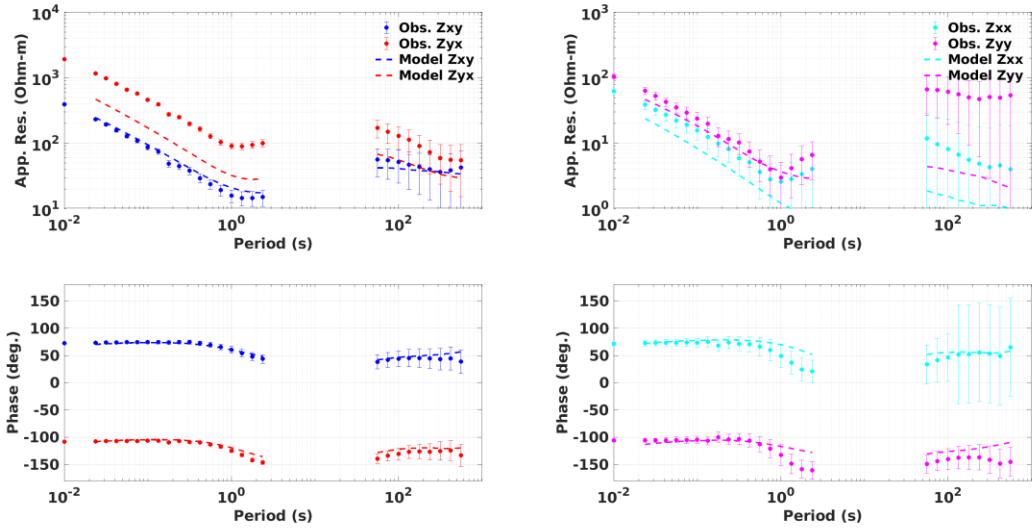
MT\_NV22003



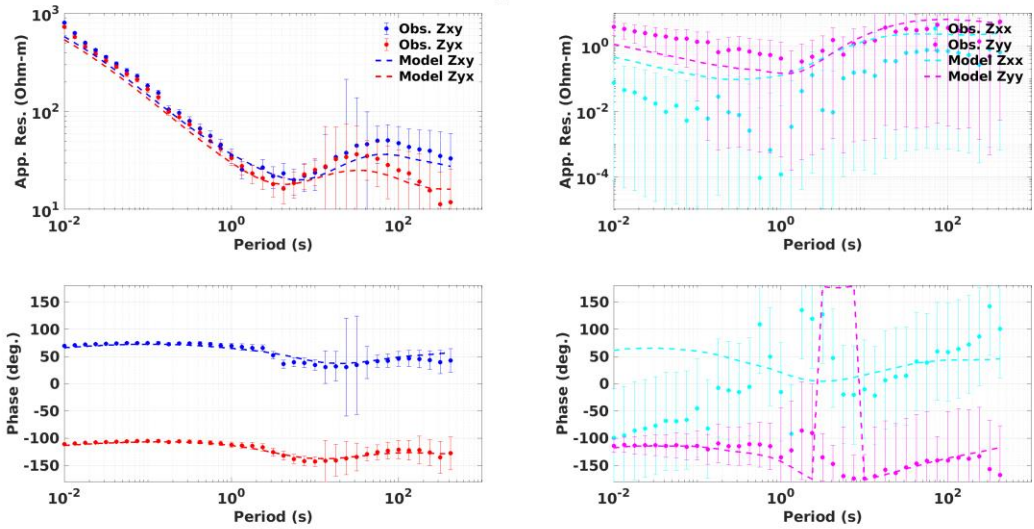
MT\_NV22004



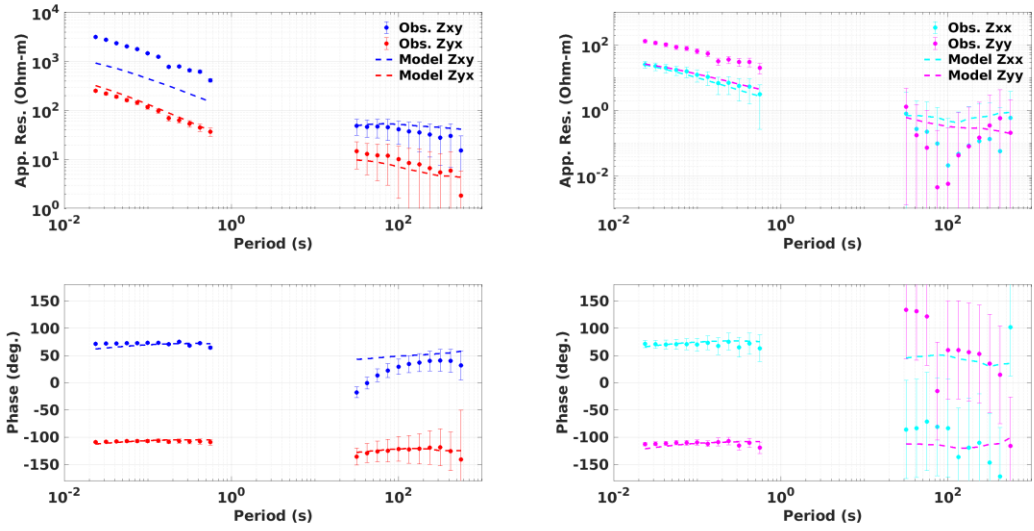
MT\_NV22011



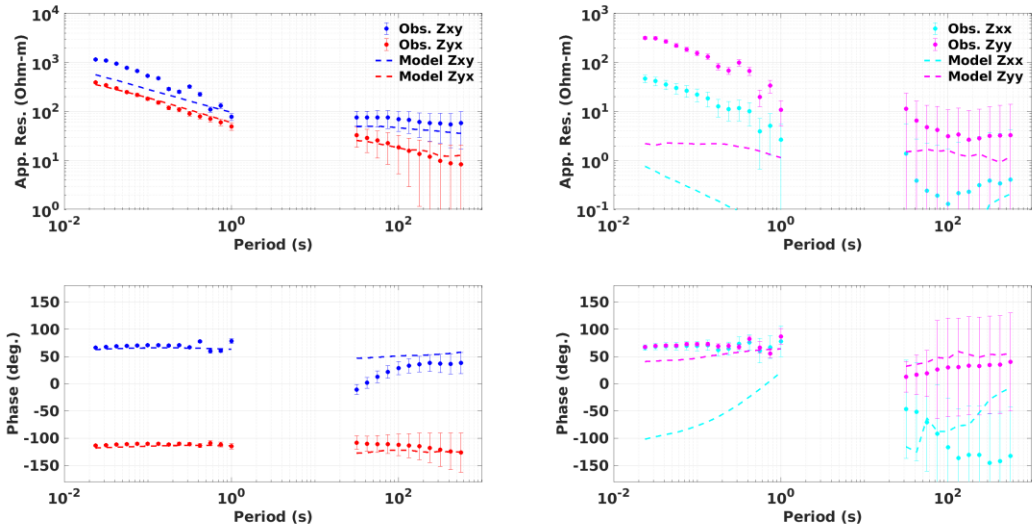
MT\_NV22059



MT\_NV22055

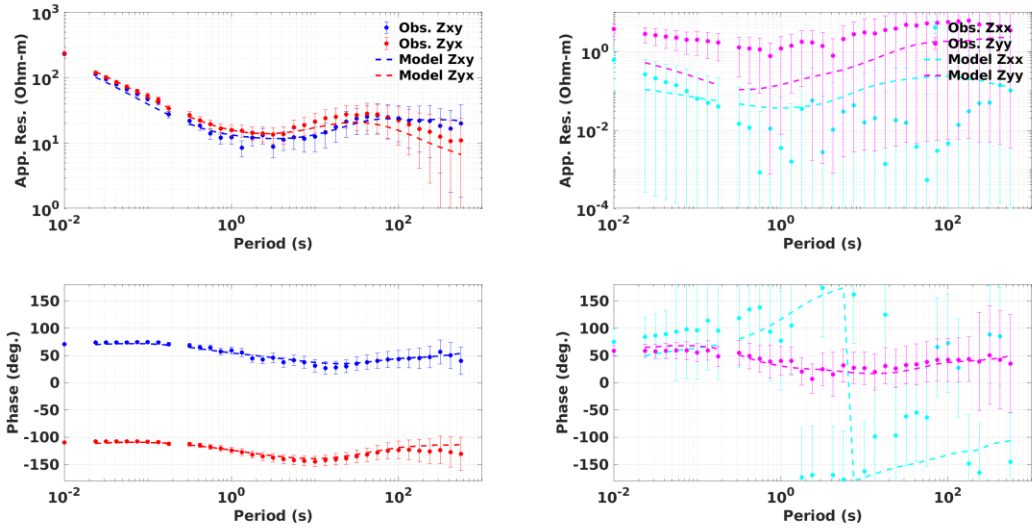


MT\_NV22051

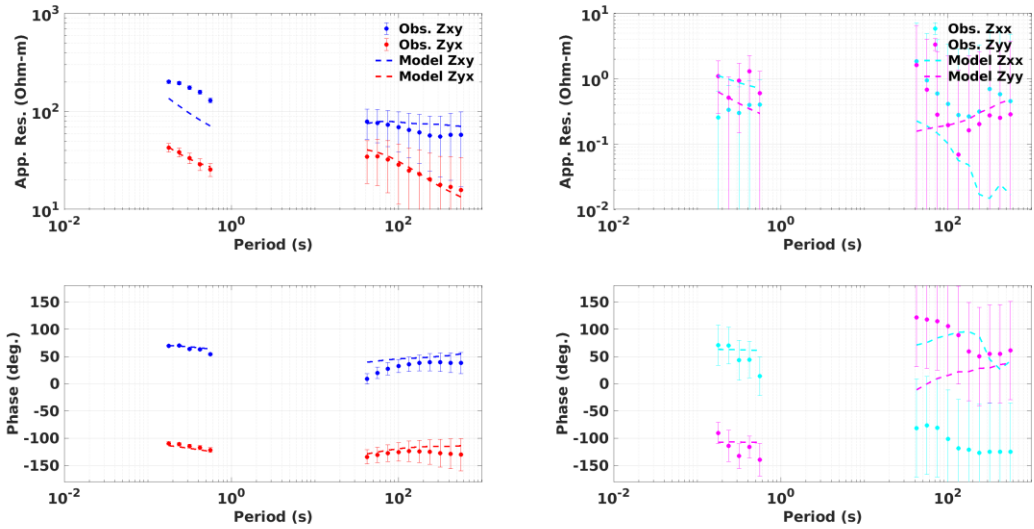




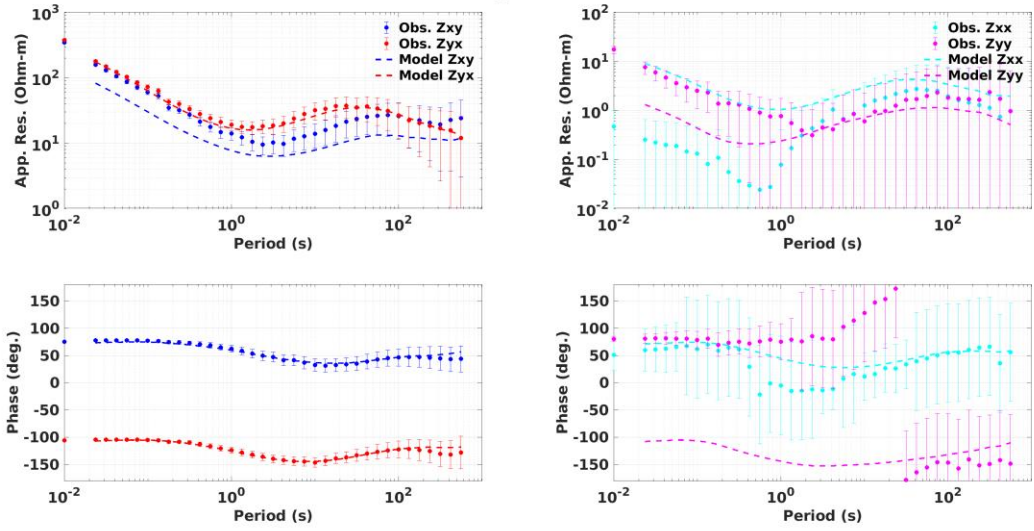
MT\_NV22036



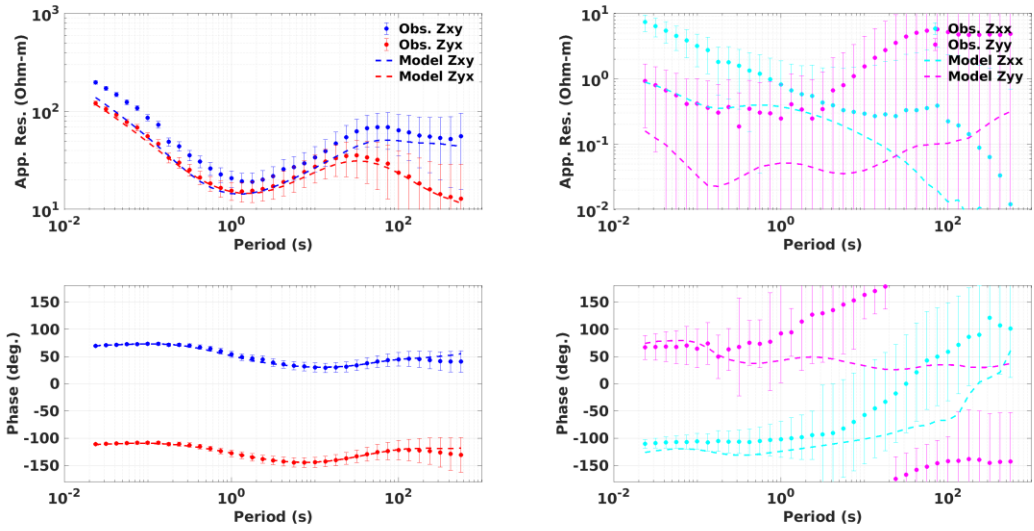
MT\_NV22030



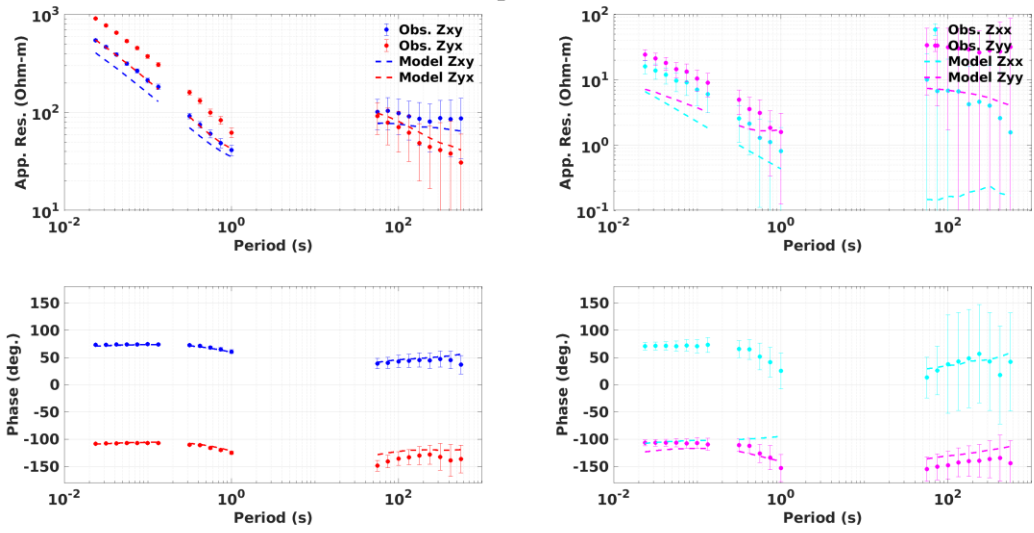
MT\_NV22024



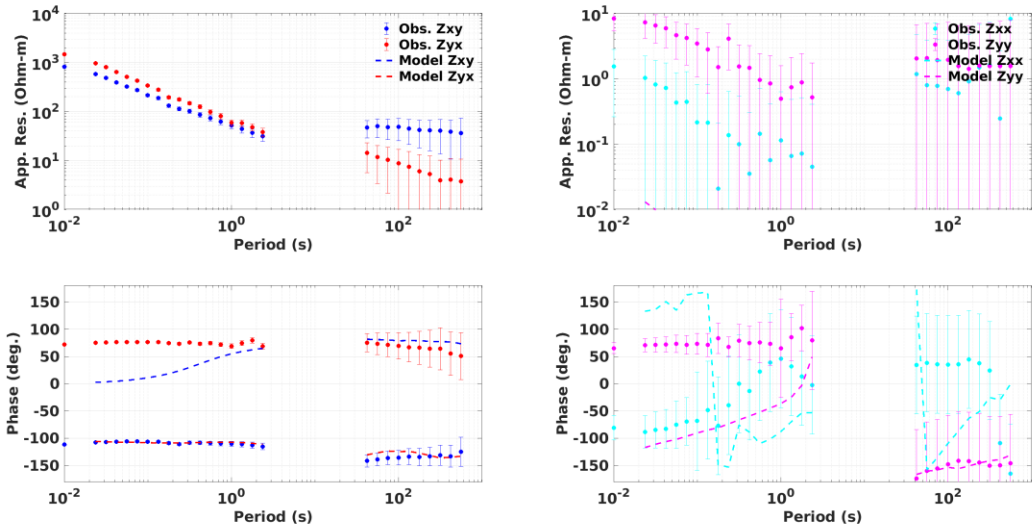
MT\_NV22018



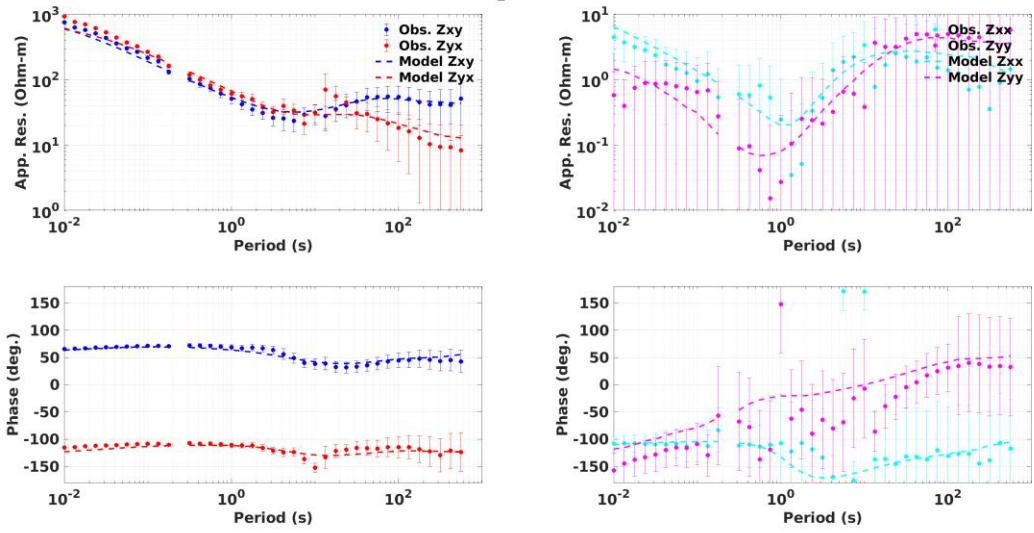
MT\_NV22013



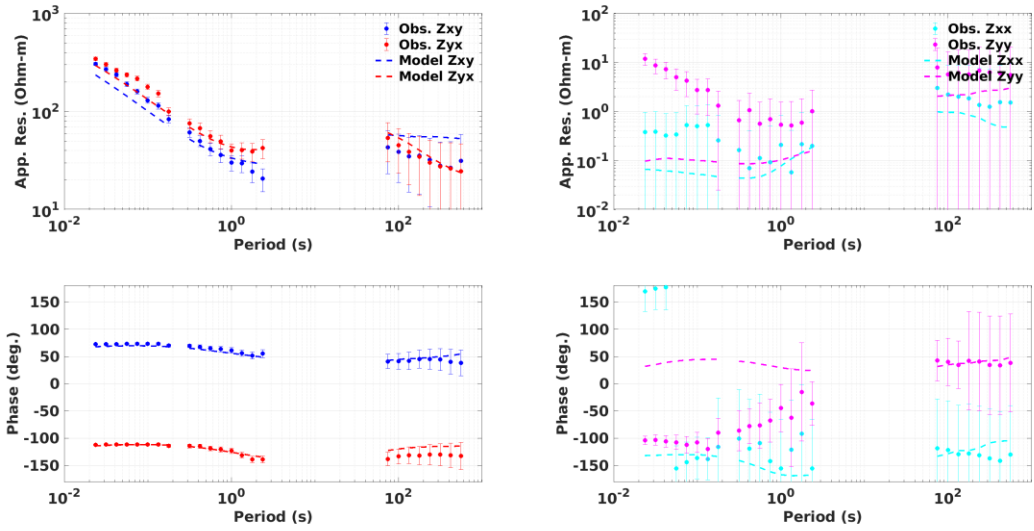
MT\_NV22056



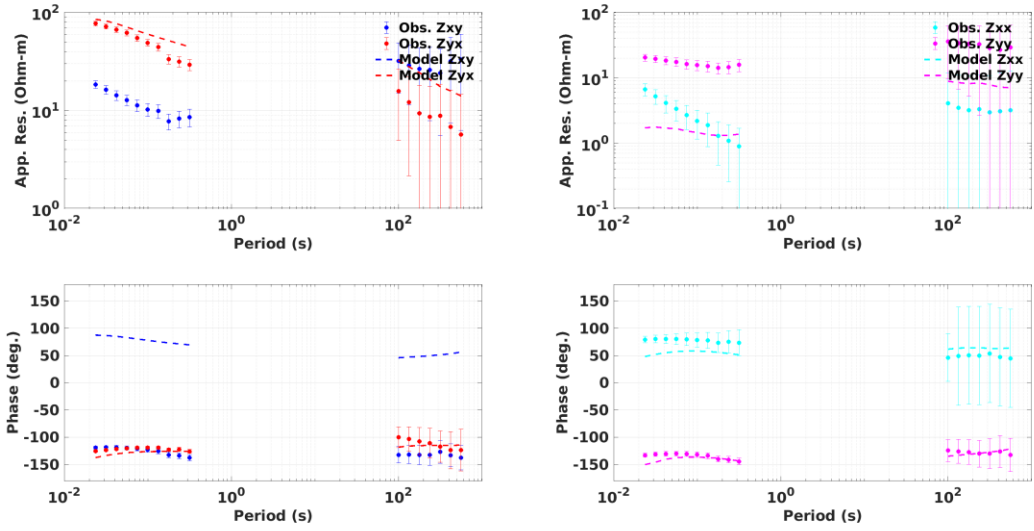
MT\_NV22052



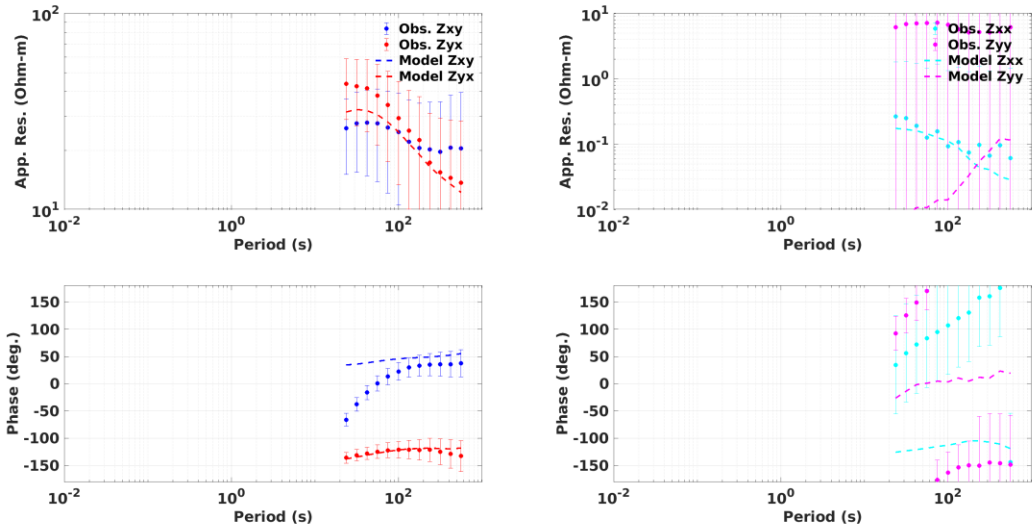
MT\_NV22038



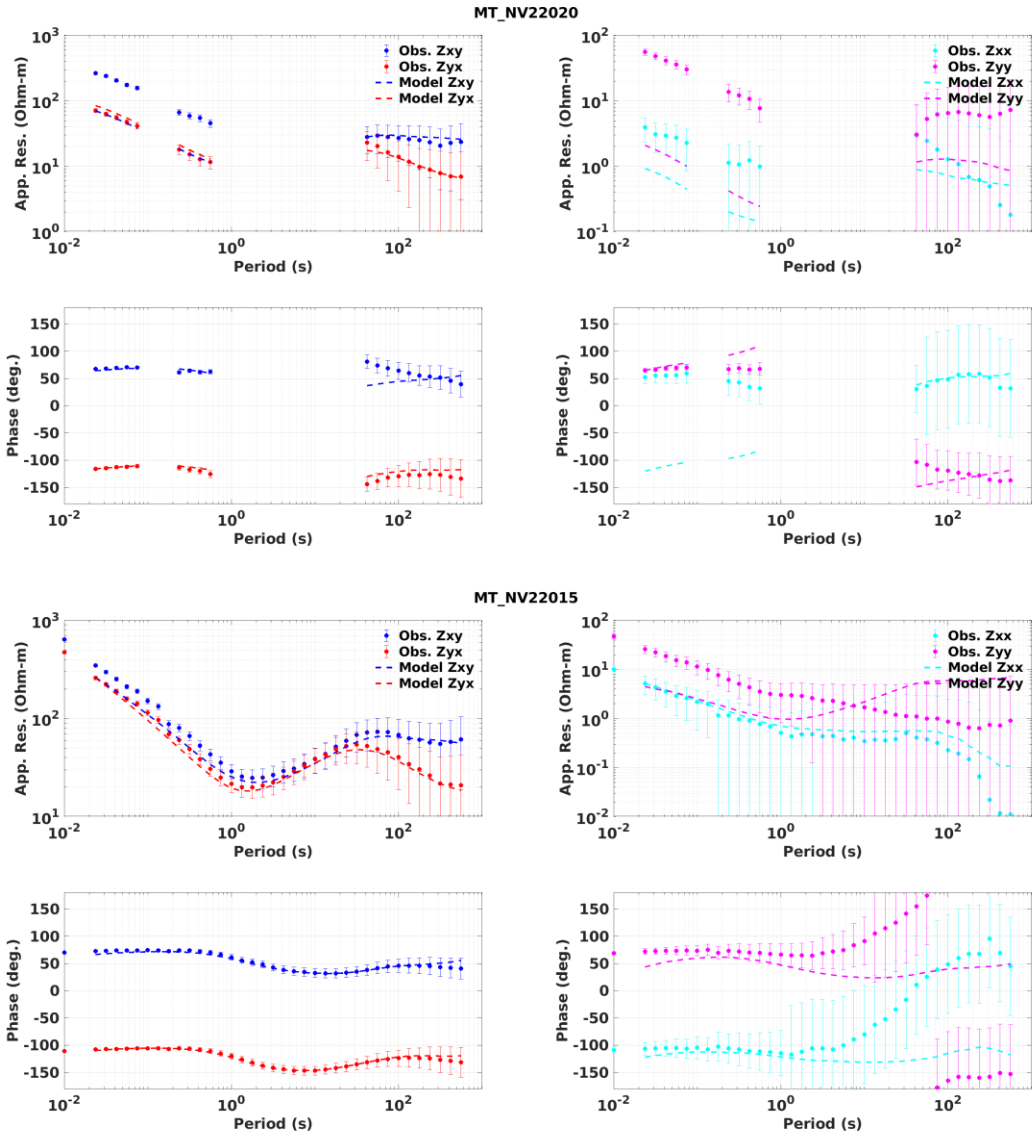
MT\_NV22033



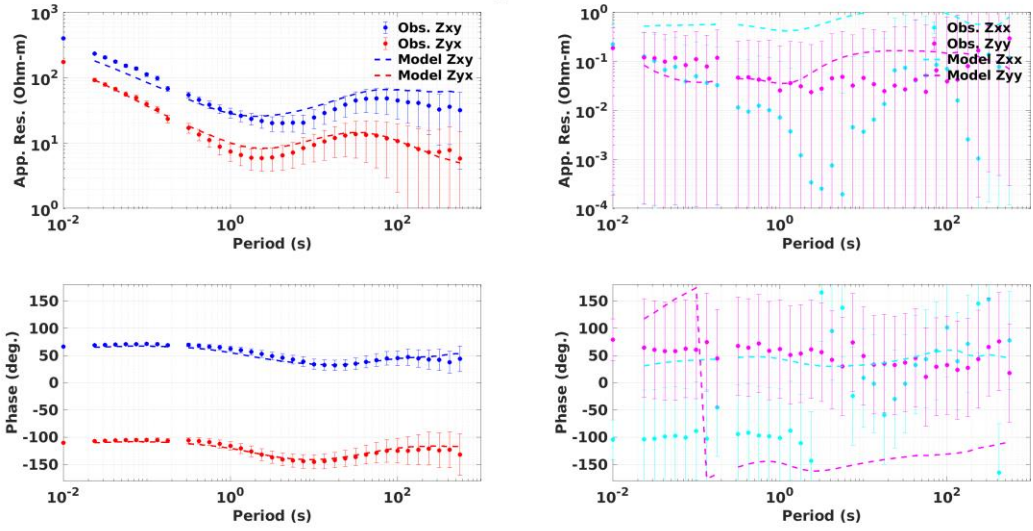
MT\_NV22026



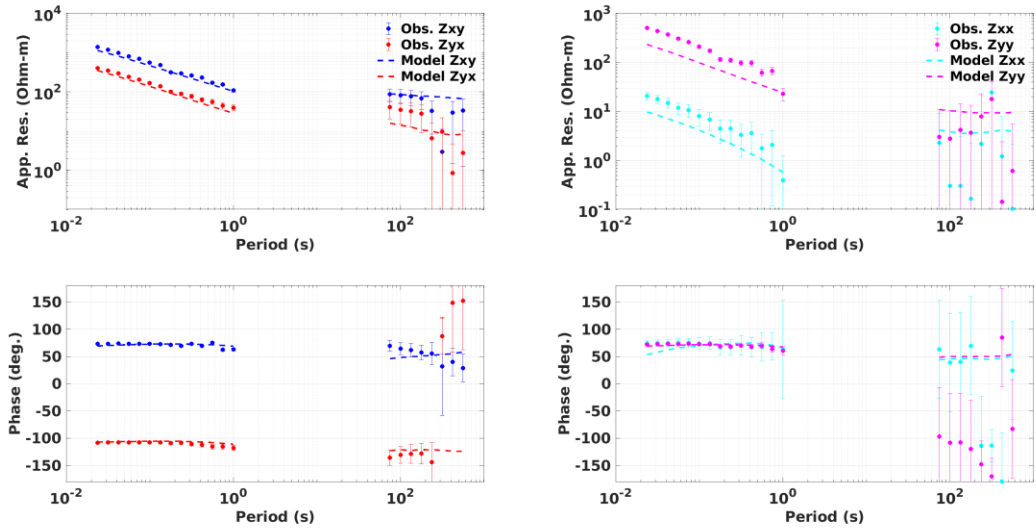




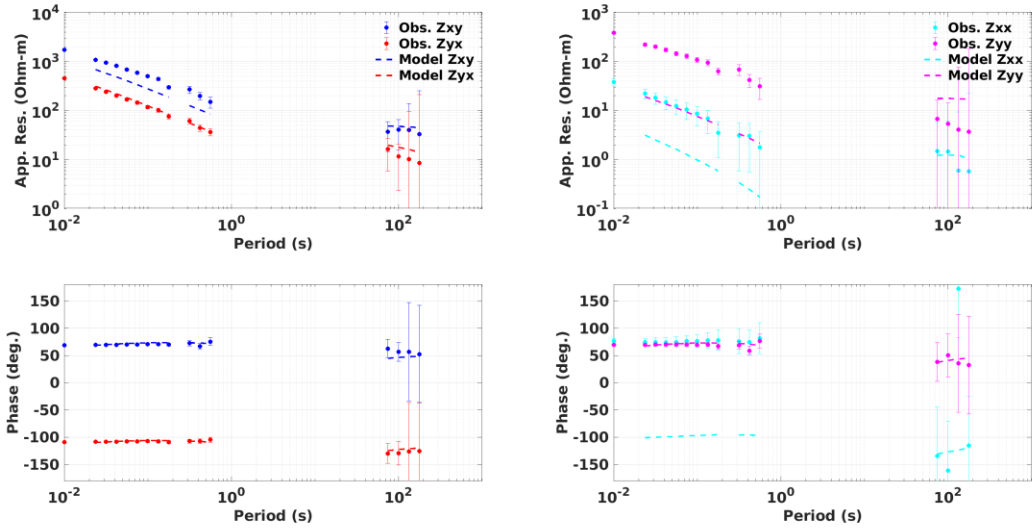
MT\_NV22005



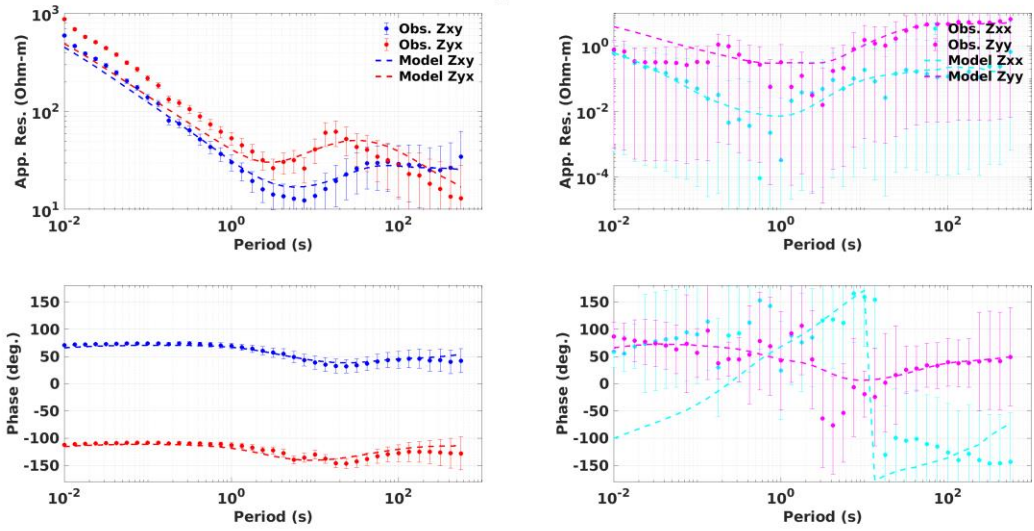
MT\_NV22057



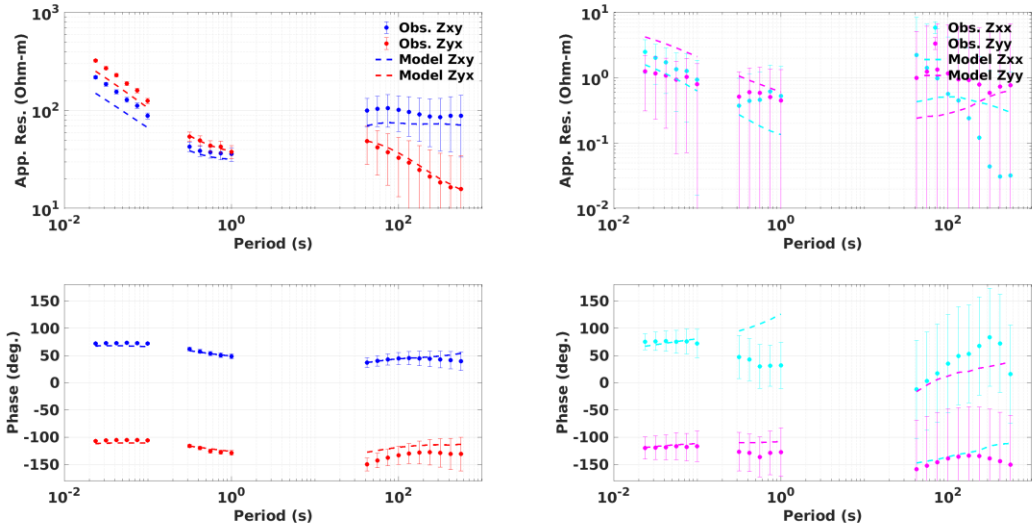
MT\_NV22053



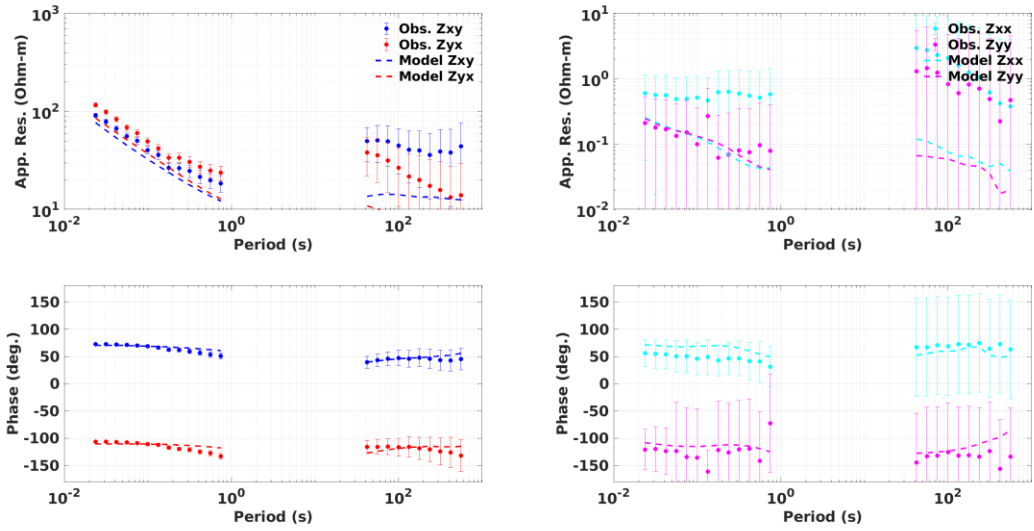
MT\_NV22047



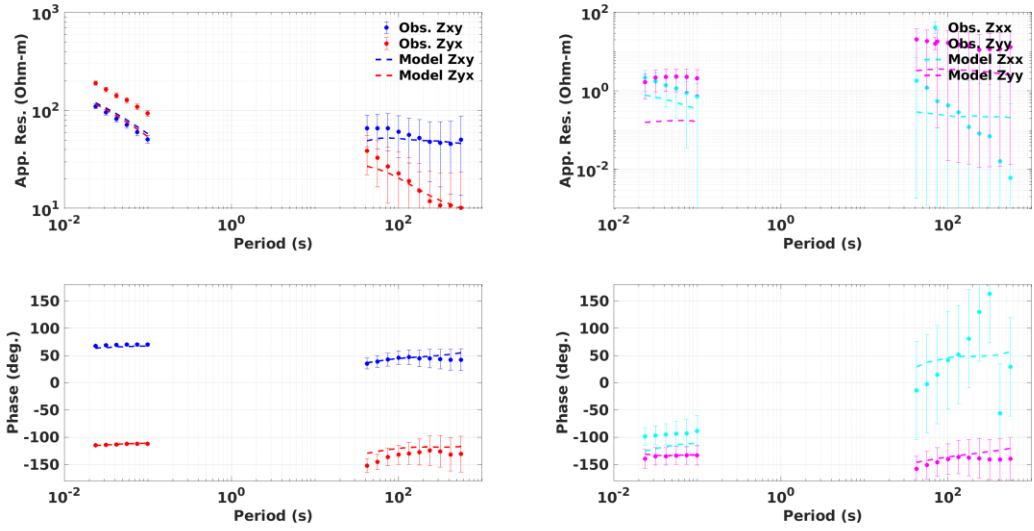
MT\_NV22034



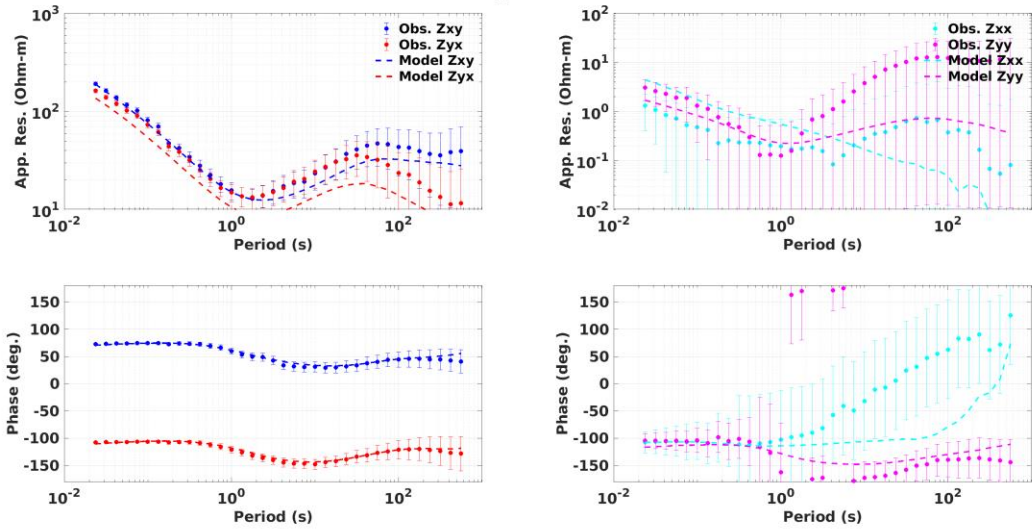
MT\_NV22028



MT\_NV22021

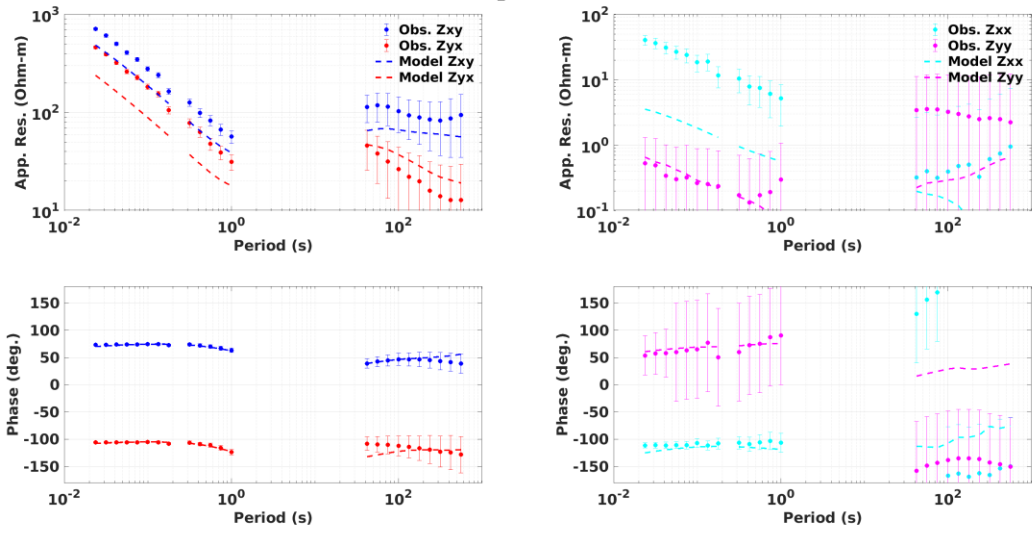


MT\_NV22016

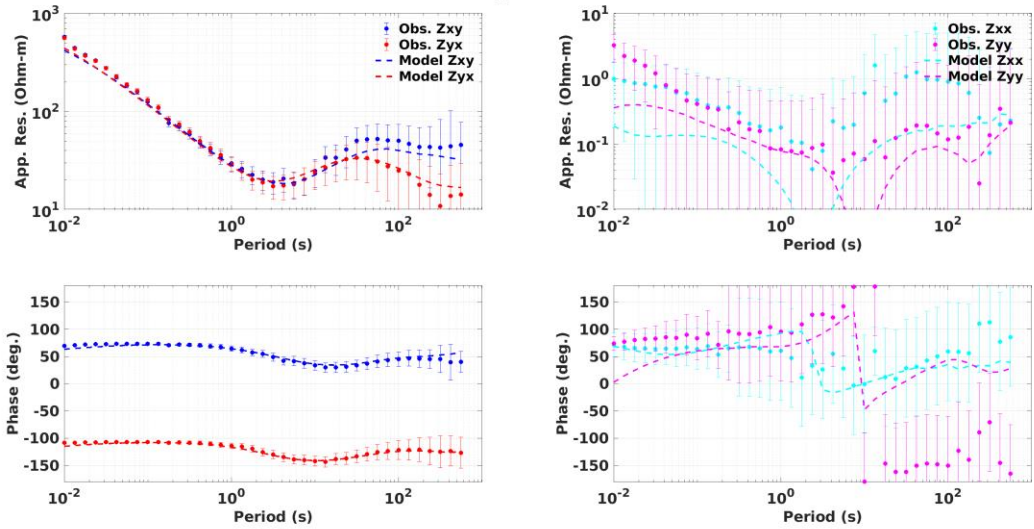




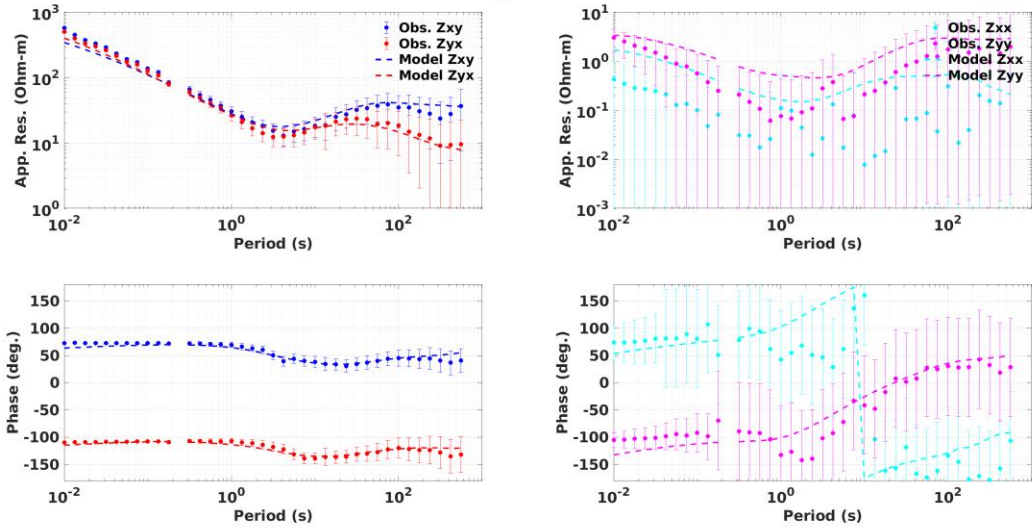
MT\_NV22009



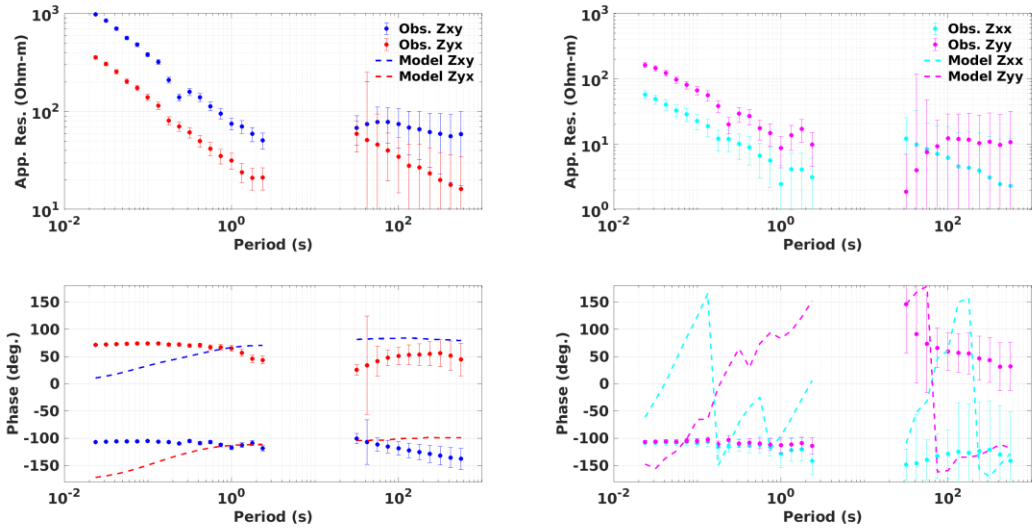
MT\_NV22058



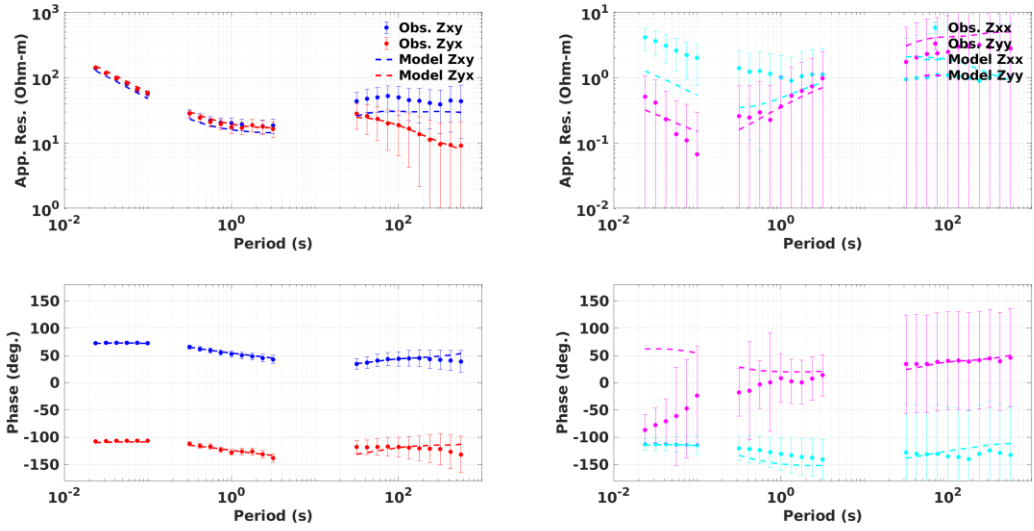
MT\_NV22054



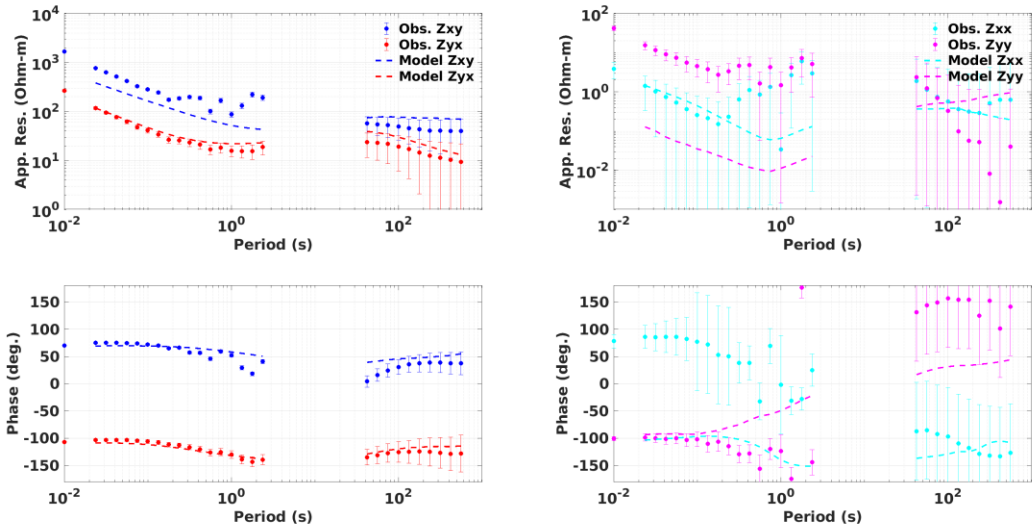
MT\_NV22050



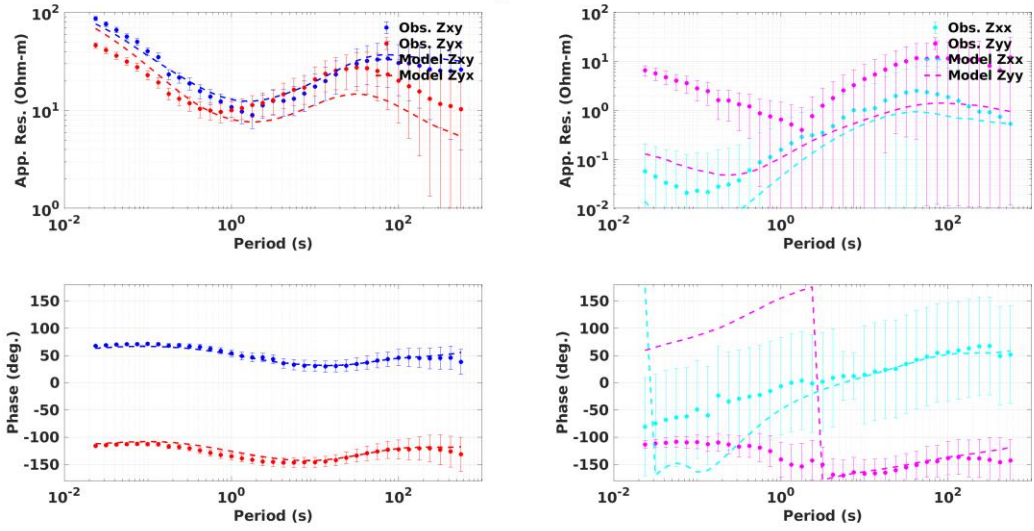
MT\_NV22035



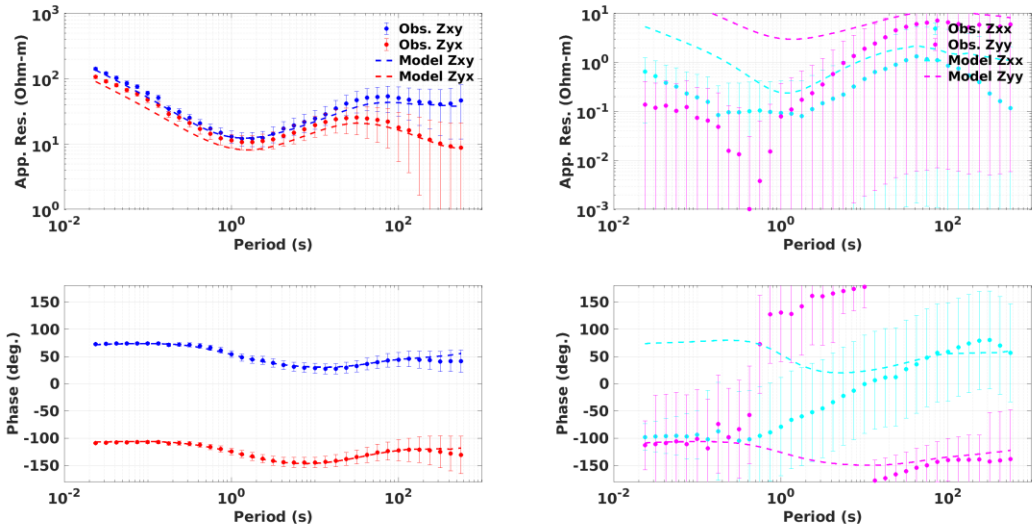
MT\_NV22029



MT\_NV22023



MT\_NV22017



# Comparison between jointly inverted models and seismic tomographic Vp model

Having established that the joint inverse model fits the data very well, and that by comparing the well resolved features from the joint inversion with the same features in the single inversions we see that the key features are robust, we return below to the vertical sections through the models, adding this time a comparison with the active+passive seismic tomography  $v_p$  model of Heath, et al., 2015 (an update from the Beachley, et al.  $v_p$  model we previously referred to in Figure 15).

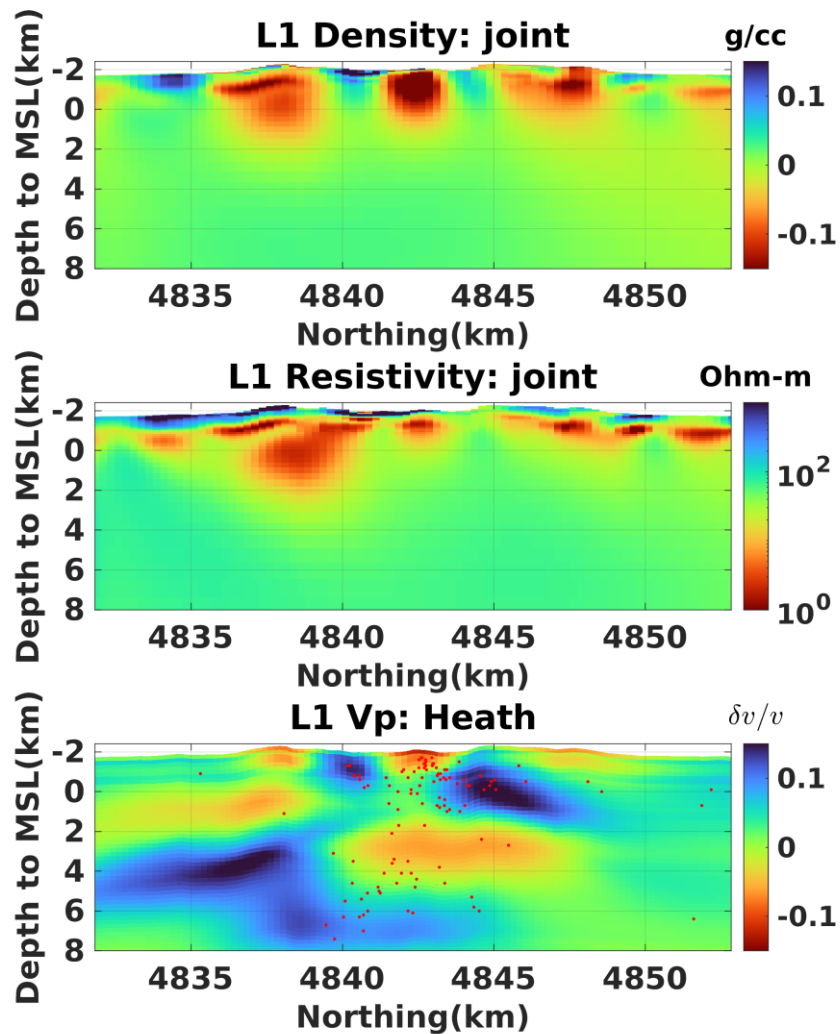


**Figure 28.** Comparison between jointly inverted models and seismic tomographic Vp model along the southwest-to-northwest profile L1 along the Walker Rim Fault to the southwest, through the center of the caldera, and along the Sisters Fault to the northwest along the rift zone. The red dots on the Vp profile are earthquake events with hypocenters less than 2 km away from the profile (i.e., earthquakes in the region bounded by the two white dashed lines shown on horizontal sections). The earthquakes are recorded by PNSN stations from 2012 to 2023.



In the upper 2 km along the L1 profile, the density, resistivity, and velocity models correlate with each other very well. The shallow red low-density, low-resistivity, low-velocity zones in the south rim may be associated with geothermal alteration. At depths of 2 km MSL, beneath this shallow anomaly, a larger low-velocity zone appears with no associated density or resistivity anomaly. The relationship of this feature with the shallow anomaly is unclear. If this is an accumulation melt that feeds the upper anomaly, the dry rhyolitic melt interpretation of Bowles-Martinez & Schultz (2020) may hold. While the absence of a density anomaly is somewhat perplexing, rhyolitic melt exhibits a smaller dependence of density on temperature than dacite, andesite and basalt melts (Leshner and Spera, 2015). Alternative interpretations may be that this deeper seismically slow region may be attributable to a thermal anomaly or an overpressured zone.

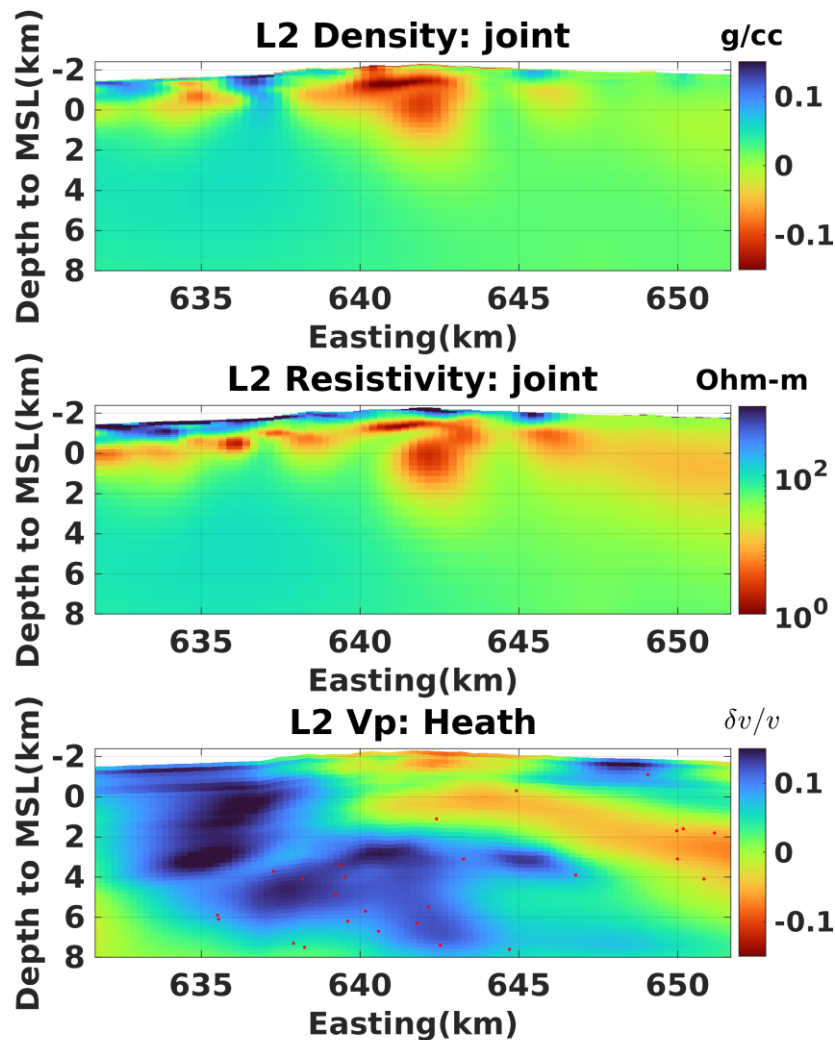


**Figure 29.** Comparison between jointly inverted models and seismic tomographic Vp model along a west-to-east profile L2 across the south caldera rim. The red dots on the Vp profile are earthquake events with hypocenters less than 2 km away from the profile.

The west-to-east profile across the south rim of the volcano shown in Figure 29 aligns the relatively low density, low resistivity feature along the south rim adjacent to the Big Obsidian Flow inside the south caldera wall with a shallow and a deeper low velocity feature that extends to the east as it deepens.

In the west-to-east profile across the center of the caldera (Figure 30 below), the tomography model reveals a low velocity zone at considerable depth beneath the caldera (at Easting 640 km – 644 km and Depth 2.5 – 5.9 km MSL) that is absent from the density and resistivity models.

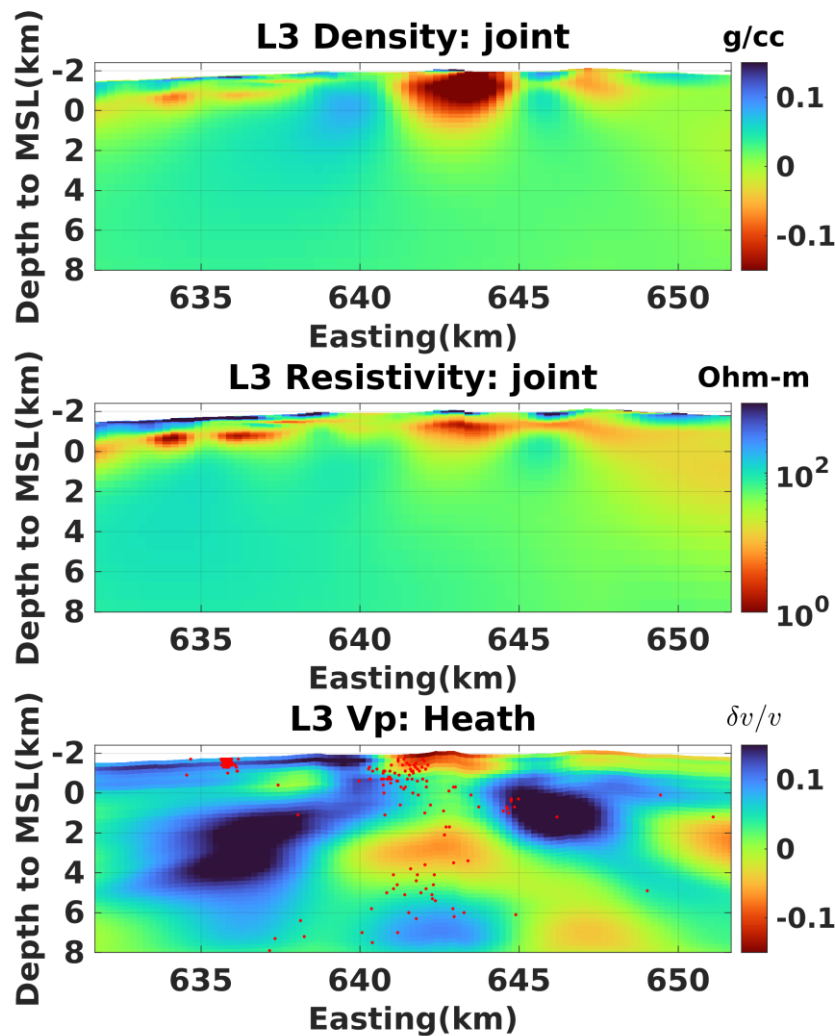


**Figure 30.** Comparison between jointly inverted models and seismic tomographic Vp model along a west-to-east profile L3 across caldera center. The red dots on the Vp profile are earthquake events with hypocenters less than 2 km away from the profile.

The previous 3-D resistivity model developed prior to the NV22 survey (Bowles-Martinez and Schultz, 2020) also failed to show a low resistivity feature at depth beneath the caldera that corresponded to the low velocity zone of Beachley, et al., (2012), and it was posited that this could be explained by the melt zone being dry and rhyolitic. While still plausible, the absence of a density anomaly within the sub-caldera low  $v_p$  zone of putative melt, with the density in the jointly inverted model of  $\sim 2.5$  g/cc at depths between 2.0 and 4.0 km msl beneath the center of the caldera bears further scrutiny. Leshner and Spera (2015) indicate that the density of dry rhyolite at 900°C and 1 bar ( $10^{-4}$  GPa) is 2.34 g/cc, with density decreasing with increasing hydration. In all cases the density of silicate melts decreases with increasing temperature. At 1 GPa pressure (equivalent to 30 km depth) this increases to 2.54 g/cc, but for these relatively shallow crustal depths of a few km beneath the caldera floor, pure dry rhyolitic melt density is

somewhat lower than the density in the joint inversion model. The density of both basaltic and dacitic melt exceeds that of rhyolitic melt, and while it may be that the a purely dacitic system is an oversimplification, these newer results remain consistent with a dry melt interpretation.

## Comparison between jointly inverted models and the surface geologic map

On the following pages, the comparison of the jointly inverted models with mapped geologic features is shown.

The geologic map of Newberry Volcano in Figure 31 (MacLeod, et.al, 1995) presents a clear north-northwest pattern in the distribution of Holocene mafic flows (in orange color). The dark red color of Holocene cinder cones and fissure events are distributed in a similar pattern in the north and run south-southwest in the south of the caldera following the distribution of Walker Rim fault zone.

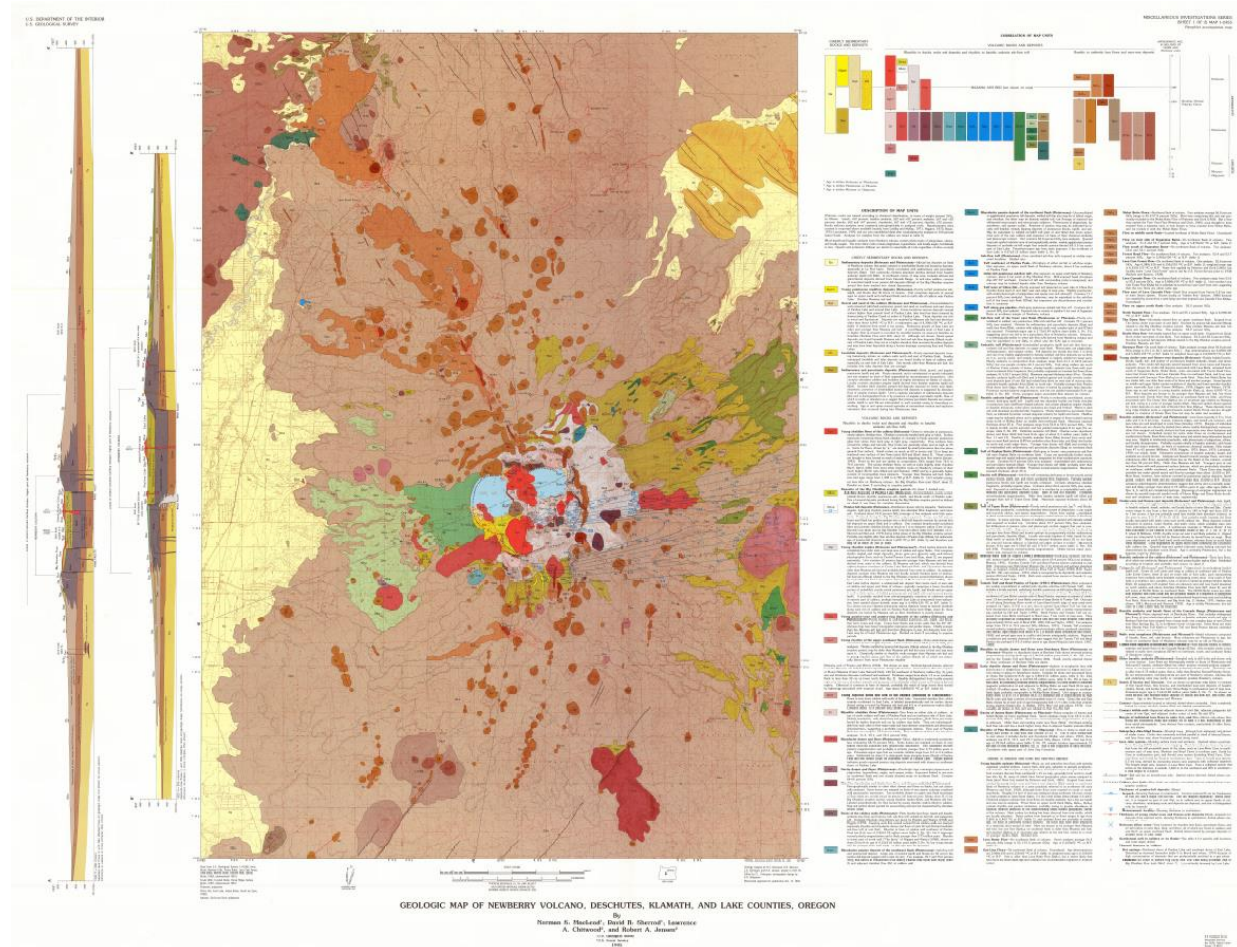


**Figure 31.** Geologic map of Newberry Volcano (MacLeod, et.al, 1995)



The distribution of Holocene mafic flows, cinder cones, and fissure vents from the geologic map is overlaid on the horizontal sections of the jointly inverted models. For a shallow depth of 1.4 km above MSL, the red zones of low density and low resistivity overlaps with the surface mafic flows in the caldera center and in the north and south rims. The fissure vents at the caldera ring in the east rim also has low density low resistivity signatures.

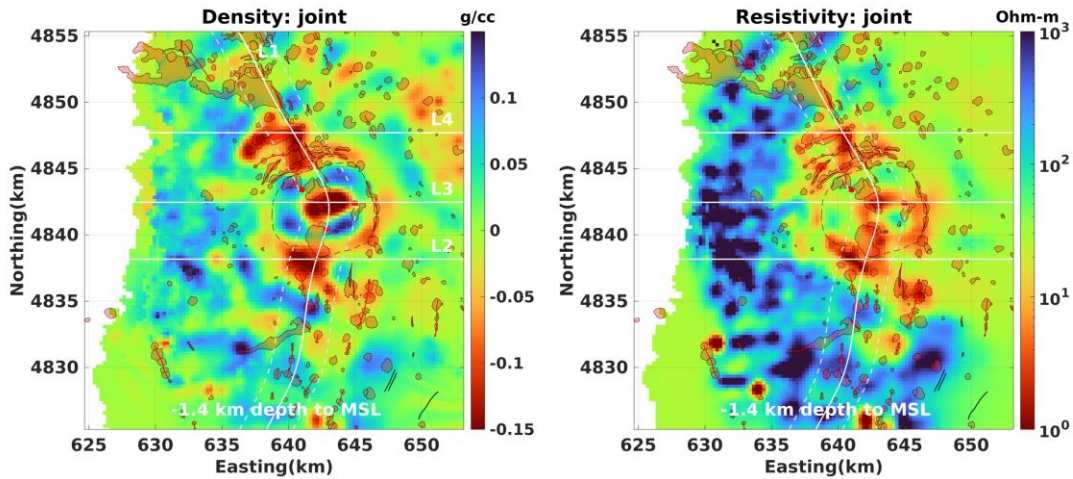


**Figure 32.** Overlays of geologic map on horizontal sections of jointly inverted models at a depth of 1.4 km above sea level/1 km below Paulina Peak/0.5 km below the caldera floor. The Holocene mafic flows, cinder cones, and fissure vents are shown as transparent red zones with black boundaries. The red solid lines denote fissure vents. Known faults are shown as black solid lines.

At a greater depth of 0.9 km above MSL, the correlation of mafic flows to the north and south of the caldera with low density and low resistivity zone is more significant.

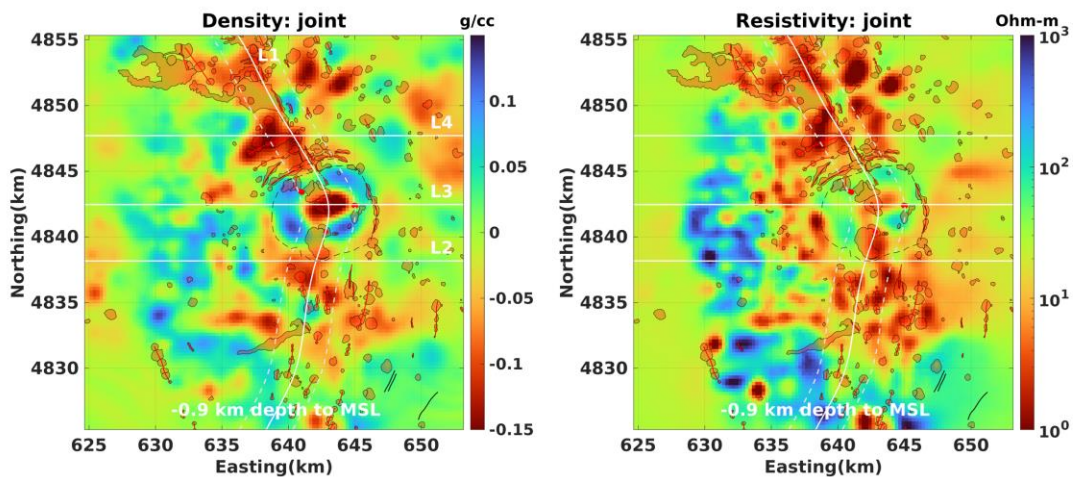


**Figure 33.** Overlays of geologic map on horizontal sections of jointly inverted models at a depth of 0.9 km above sea level/1.5 km below Paulina Peak/1.0 km below the caldera floor. The Holocene mafic flows, cinder cones, and fissure vents are shown as transparent red zones with black boundaries. The red solid lines denote fissure vents. Known faults are shown as black solid lines.



At even greater depths in Figures 34-36, the pronounced low density and low resistivity zone in the southeast part correlates with cinder cones and fissure events in those areas.

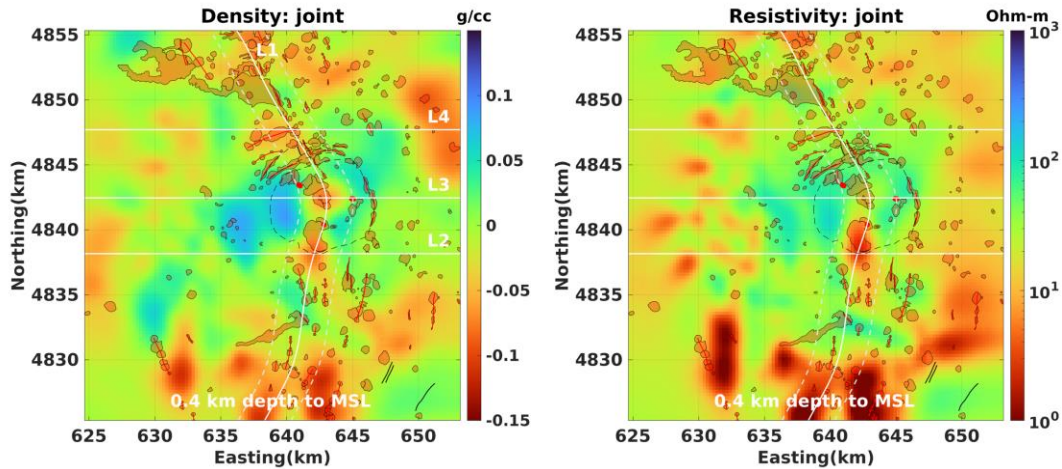


**Figure 34.** Overlays of geologic map on horizontal sections of jointly inverted models at a depth of 0.4 km below sea level/2.8 km below Paulina Peak/2.3 km below the caldera floor

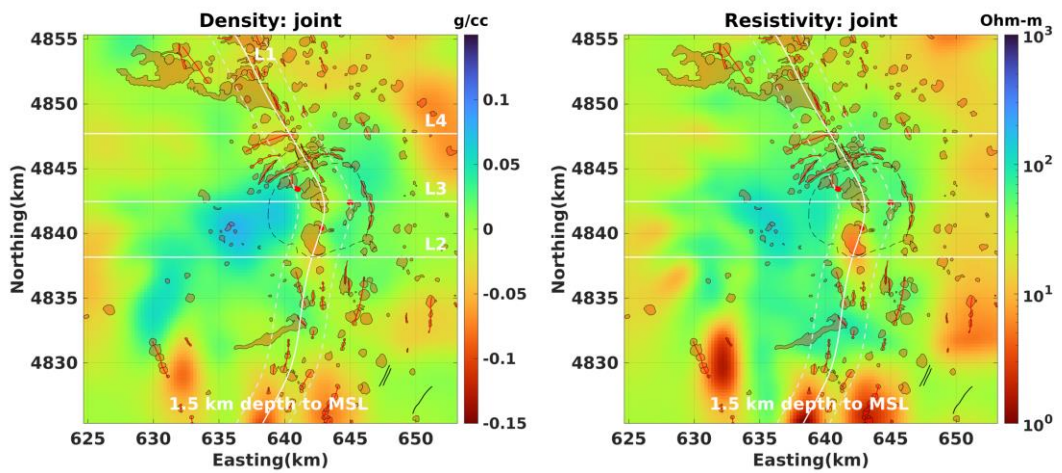


**Figure 35.** Overlays of geologic map on horizontal sections of joint inverted models at a depth of 1.5 km below sealevel/3.9 km below Paulina Peak/3.4 km below the caldera floor

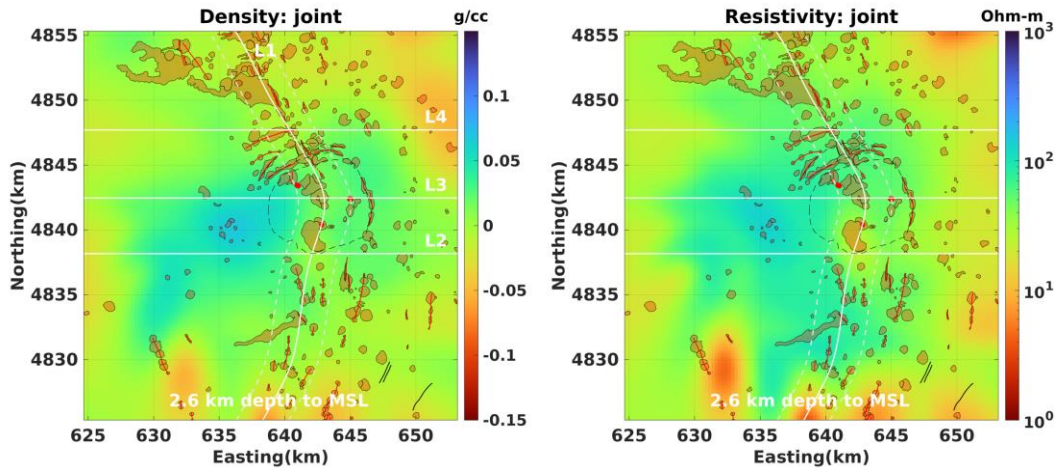


**Figure 36.** Overlays of geologic map on horizontal sections of jointly inverted models at a depth of 2.6 km above sea level/5.0 km below Paulina Peak/4.5 km below the caldera floor.

# Comments on the south rim and flank anomaly and nearby well data

Figure 37 below shows the location of the nearest exploration wells to the features in the jointly inverted electrical resistivity map at a depth of 2.3 km below the caldera floor. Since the south rim and flank anomaly described in previous sections of this report is the most prominent feature arising from the single and joint MT and gravity inversions and given the close co-registration of this feature with seismic tomography indications of a low velocity zone, we consider here existing well log, petrology and temperature profile data from adjoining exploration well GEO N-1.

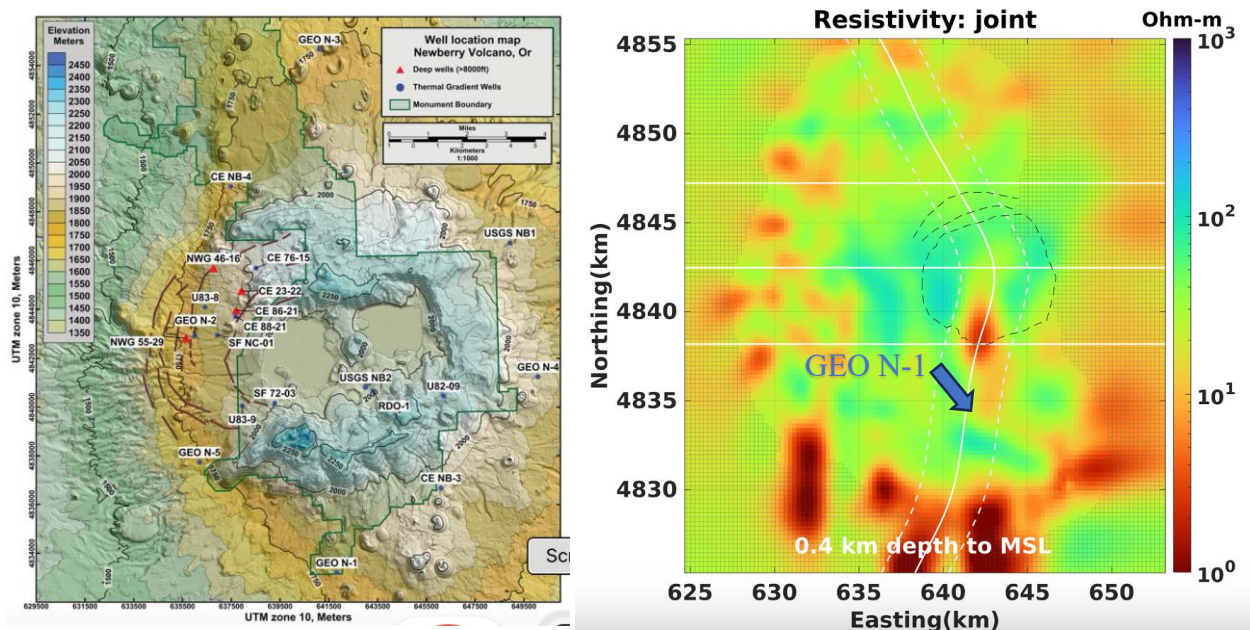


**Figure 37. (left)** Topographic map of Newberry Volcano with exploration well locations marked. Brown lines are inferred structures from lidar data (from Frone, 2015). **(right)** Horizontal map of electrical resistivity from the joint inversion, at a depth of 0.4 km below sea level/2.8 km below Paulina Peak/2.3 km below the caldera floor. The location of exploration well GEO N-1 is indicated by the tip of the blue arrow. Note that this well immediately adjoins the south flank extension of the low electrical resistivity, low relative density, slow seismic  $v_p$  feature that extends to considerable depth and that shallows in the south part of the caldera next to the Big Obsidian Flow.

Given its proximity to the Walker Rim fault and the association with faults as fluid migration pathways, the prominent low resistivity, low relative density, seismically slow south rim/flank feature likely represents the signature of hydrothermal fluids, partial melt and/or hydrothermal alteration products. We consider the temperature profile in well GEO N-1 in Figure 38 below.



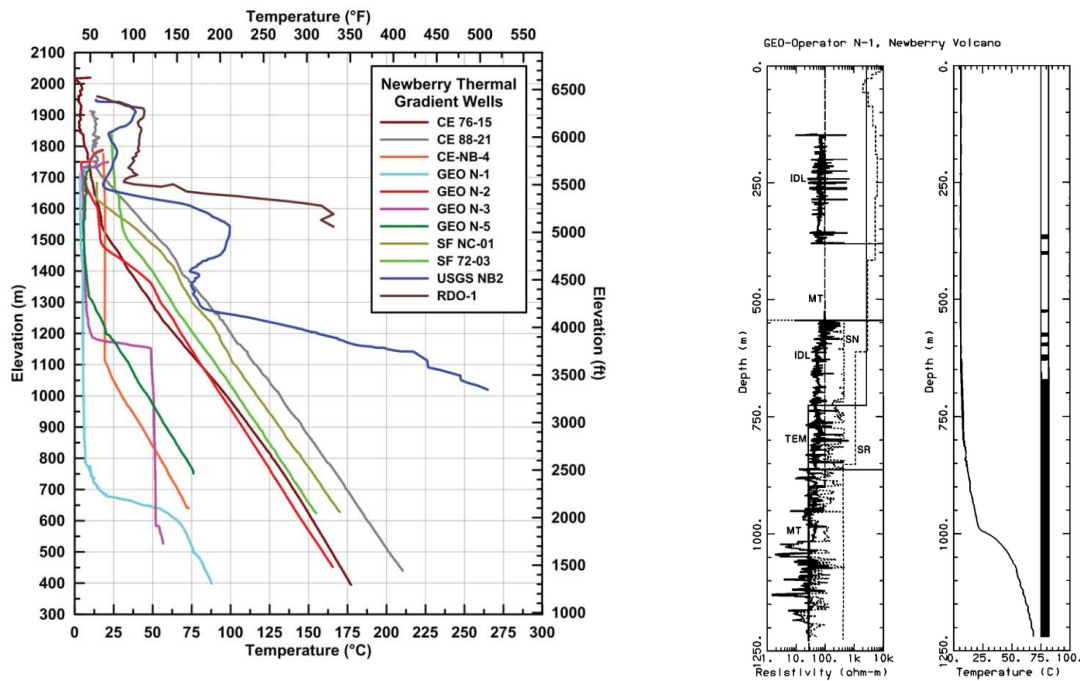


**Figure 38. (left)** Temperature profiles for Newberry Volcano gradient wells (well locations in Figure 37) (From Frone, 2015). The profile for well GEO N-1 is a light turquoise color. **(right)** Interpreted layer resistivity-depth functions for legacy 1-D DC Schlumberger array resistivity, transient electromagnetic and MT soundings elsewhere on the volcano for GEO N-1 well (from Fitterman et al., 1988). The deep induction (IDL) and short normal (SN) well logs from GEO N-1 are shown for comparison. Zones of inferred smectite alteration are shown by the bar on the temperature plot, which is the same temperature profile in the Frone figure reproduced on the left.

The most notable features of the downhole temperature profile for GEO N-1 are the suppressed temperature gradient in the upper ~800 m of the well, the transition from one linear temperature gradient to a somewhat sharper one from 800 m – 1000 m below the well head, and the sharp deviation from linear temperature gradient at depths below that. This is indicative of a transition from purely conductive heat flow in the upper sections with two zones of differing thermal properties, and advective/convective heat flow below presumably related to movement of hydrothermal fluids. The suppressed geothermal gradient above the zone of advective/convective heat flow may be a consequence of heat from below being transported laterally away from the area by the movement of fluids at depth.

The presence of smectite as an alteration product of basaltic ash and ash flow tuff has been associated with the top of the conductive zone 675 m below the GEO N-1 well head (Fitterman, et al, 1988). At the time this conclusion was drawn, there was little in the way of MT or gravity data for the area around GEO N-1, and the depth extent of the conductive zone was completely unknown.

As Fitterman, et al (1988) indicates: “Alteration minerals are commonly found in active and fossil hydrothermal systems [Steiner, 1968; Browne, 1970; Bailey et al., 1976; Keith and Muffler, 1978; Elders et al., 1979; Hulen and Nielson, 1986; Jakobsson and Moore, 1986]. While the minerals present are different for each system, commonly found minerals include smectite, illite, mixed layer illite- smectite, zeolite, calcite, chlorite, and epidote; there is usually a correlation between the minerals present and the temperature of the system [Kristrannsdottir, 1976]. Smectite is found at temperatures as high as 200°C. Mixed layer illite-smectite and illite are found at higher temperatures. Zeolites are found at slightly lower temperatures, with the maximum being around 150°C. Calcite is found over a very wide range of temperatures (50°-300°C). Epidote and chlorite are indicative of temperatures in excess of 200°C. The alteration minerals found in test holes Newberry 2 and GEO N-1 are among those commonly found in hydrothermal systems [Keith and Bargar, this issue].”, and

“The most direct evidence is given by Wright and Nielson [1986], who found that alteration zones in GEO N-1 core which were rich in smectite derived from ash flows had low resistivities (1.5-15 Ωm) on the induction logs.” Lévy et al. (2020) notes that the presence of smectite in such systems may indicate recent hydrothermal circulation. They note that “In active hydrothermal systems, the formation of smectite is not only controlled by the geothermal gradient, but also by the convective activity related to recent fault opening and causing boiling as well as chemical disequilibrium (Beaufort et al., 1995, Bril et al., 1996, Patrier et al., 1996). Compared to other clay minerals (e.g. illite, chlorite, kaolinite), smectite is much more conductive (e.g. Kaufhold et al., 2014; Kaufhold et al., 2015) and contributes significantly to the electrical conductivity of rocks, through Electrical Double Layer mechanisms (Flóvenz et al., 1985, Pezard, 1990, Revil and Glover, 1997, Waxman and Smits, 1968) and interfoliar conduction (Henry, 1997, Lévy et al., 2018, Maraqaq et al., 1990).”

Lévy, et al. (2018) note that “expandable minerals” that form clay caps in geothermal systems are thermodynamically stable from 80°C – 180°C, above which they are replaced progressively by chlorite and other minerals in the event thermodynamic equilibrium conditions exist. They note, however, in active volcanic systems smectite is observed at temperatures higher than 300°C, while in Icelandic volcanic systems discrete chlorite is found only above 270°C.

On the basis of density alone, distinguishing between mineralization products such as smectite, with a density of 2.39 g/cc or Illite at 2.63 g/cc (Sowers and Boyd, 2019) and igneous host rocks such as rhyolite (2.35 – 2.70 g/cc), granite (2.50 – 2.81 g/cc), basalt (2.70 – 3.30 g/cc), etc. without independent controls on the porosity of the formations is complicated since variations in bulk density due to variations in porosity alone can exceed the variations in the CBA gravity anomaly due to differences in rock composition. The relatively low density associated with the south rim/flank anomaly is consistent with elevated porosity and/or the presence of clays resulting from hydrothermal circulation, and/or the presence of hydrothermal fluids.

It is almost certainly the case that hydrothermal alteration products including clays such as smectite are a component of the conductive feature on the south rim and flank of Newberry volcano. The temperature gradient data from nearby well GEO N-1 suggests that this feature is likely the signature of recent, and possibly contemporary hydrothermal circulation. Given that the feature extends to considerable depth beneath the south flank/rim area of the volcano, to

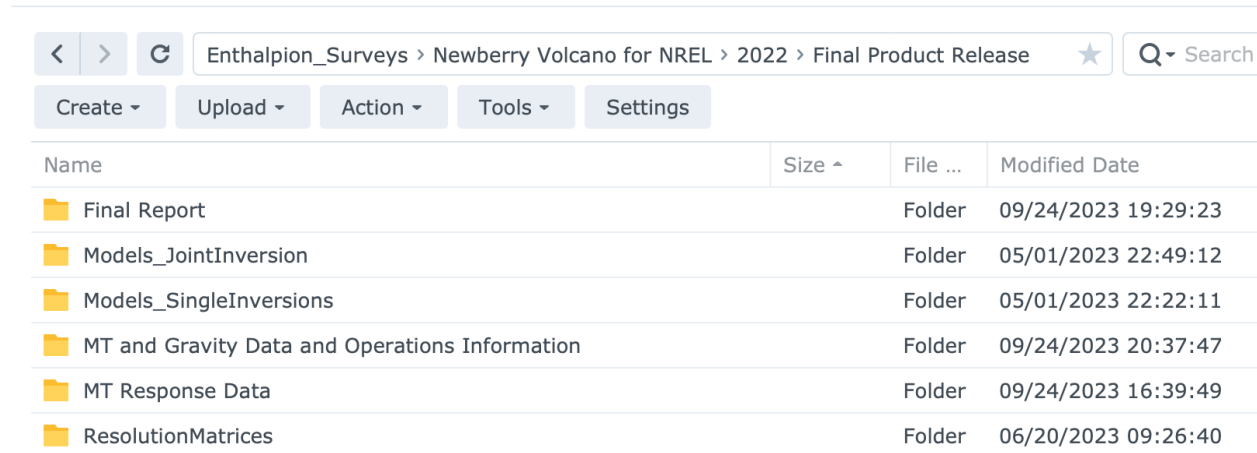


depths of at least 3.4 km and possibly to more than 4.5 km below the caldera floor – depths equivalent to the apparently unconnected (but seismically determined) melt zone beneath the center of the caldera; that it shallows next to the Big Obsidian Flow, the most recent eruptive feature on the volcano (1,300 ybp); and that it adjoins the Walker Rim crustal fault that provides a likely structural pathway for fluid migration, the south rim/flank feature is posited to be the trace of melt and hydrothermal fluid migration from great depths beneath the south flank, and likely the source of heat that powers the hydrothermal circulation that continues to the present day and that has left geochemical evidence in the form of hydrothermal mineralization products found in nearby well core samples. It appears that this deep source of heat and (at depth) melt is not directly connected to the seismic low velocity/melt body beneath the caldera, but rather is part of a south flank source that is most likely the feeder system for the Big Obsidian Flow.

Follow-on efforts to drill as close as possible to the feature, subject to restrictions against drilling within the boundary of the National Volcanic Monument, is a logical next step to validate this conceptual model. Cores, well logs and distributed temperature sensing data from a location immediately east of well GEO N-1, but outside and as close as possible to the Monument boundary would place such a well close to the center of the south flank electrical resistivity, density, seismic velocity anomaly.

# Folder Structure of Electronic Data Release Final Product

The final products of Enthalpion Survey NV22 are made available to NREL through the following folder structure.

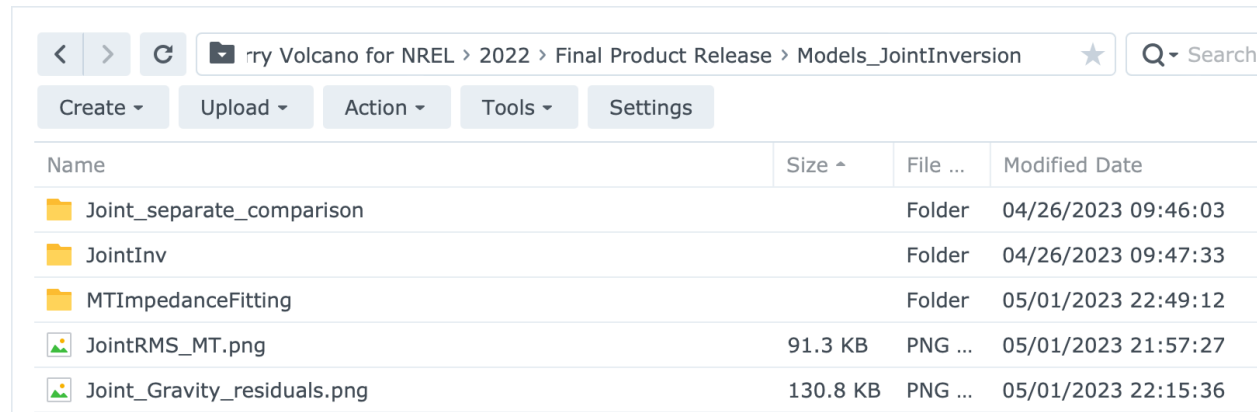


The screenshot shows a file explorer interface with the following table of folders:

Name	Size ^	File ...	Modified Date
Final Report		Folder	09/24/2023 19:29:23
Models_JointInversion		Folder	05/01/2023 22:49:12
Models_SingleInversions		Folder	05/01/2023 22:22:11
MT and Gravity Data and Operations Information		Folder	09/24/2023 20:37:47
MT Response Data		Folder	09/24/2023 16:39:49
ResolutionMatrices		Folder	06/20/2023 09:26:40

The **Final Report** folder contains this document in Word and PDF formats.

The **Models\_JointInversion** folder structure is as follows:



The screenshot shows a file explorer interface with the following table of folders and files:

Name	Size ^	File ...	Modified Date
Joint_separate_comparison		Folder	04/26/2023 09:46:03
JointInv		Folder	04/26/2023 09:47:33
MTImpedanceFitting		Folder	05/01/2023 22:49:12
JointRMS_MT.png	91.3 KB	PNG ...	05/01/2023 21:57:27
Joint_Gravity_residuals.png	130.8 KB	PNG ...	05/01/2023 22:15:36

The **Joint\_separate-comparison** subfolder contains four graphics files (.png format) showing both separate MT and gravity and joint MT and gravity inverse model results, in both vertical sections through the 3-D model, along the L2 and L3 lines, and horizontal map views of the same, for two different model depths.

The **JointInv** subfolder contains nine graphics files (.png format) showing the full set of vertical sections and horizontal map views at various model depths. The folder also contains two spreadsheets (.csv format) containing the joint inversion density and resistivity models in columnar format with each row containing model cell locations (easting, northing, depth to

MSL) and model parameter (density in g/cc for the gravity model and resistivity in Ohm-m for the MT model).

Note: resistivity model values of  $10^{10}$  Ohm-m (or in floating point format, 10000490713 Ohm-m) represent cells that are above ground level – i.e. up in the air layer.

The **MTImpedanceFitting** subfolder contains 36 graphics files (.png format), each showing the MT impedance data from a given Newberry wideband MT station actually used in the inversion, and the fit of the 3-D resistivity model to that data. These are displayed as apparent resistivity vs. period and phase vs. period for all four elements of the impedance tensor, with the principal (off-diagonal) elements xy and yz on the left side of the display and the diagonal elements xx, yy (defined for 3-D structure) on the right side of the display.

The two graphics files found directly in the **Models\_JointInversion** folder display the RMS misfits, at each station, between the MT impedances vs. period at each station and the calculated impedances from the inverted 3-D resistivity.

Back at the top level of the **Final Product Release**, the **Models\_SingleInversions** folder contains three subfolders, **Density**, **Resistivity**, **Tipper**, as well as several graphics files in .png format. The **Density** and **Resistivity** subfolders contain various views of the eponymous properties from, respectively, the non-joint gravity and MT inversions, respectively. The **Tipper** subfolder contains images in a map view overlaid on the resistivity volume at a depth of 2.5 km, showing the real and imaginary components of the induction vectors for each of a set of different periods (1/frequencies), serving as a proxy for depths of penetration below ground level. This subfolder also includes a movie in .mp4 format that sequentially displays these images as at each of the periods in ascending order, i.e. representing successively greater depths beneath ground level.

Also at the top level of the **Final Product Release**, the **MT and Gravity Data and Operations Information** folder contains the **daily reports** subfolder and the **MT-Gravity-Survey-Locations-and-Data** subfolder, where original and processed gravity data can be found, as well as maps showing the locations of the gravity and MT stations.

The **MT and Gravity Data and Operations Information > MT-Gravity-Survey-Locations-and-Data > NREL-Sharepoint-Gravity-Survey > Gravity > Gravity Data** subfolder folder contains spreadsheets of the raw measured gravity data (file: Grav\_Raw\_Data.xlsx), as well as the final processed data (file: Newberry\_Gravity\_2022\_Final.xlsx). The formats of these files are show below:

Format of Grav Raw Data.xlsx.

	A	B	C	D	E	F	G	H	I	J	K	L	M	N
1	Station	Date	Pacific Time	Longitude (X)	Latitude (Y)	Elevation (Z)	Grav. Reading	Notes						
2	B1	6/22/22	8:46	-121.273476	43.709687	1923	110.09							
3	B1	6/22/22	8:48	-121.273476	43.709687	1923	110.079							
4	B1	6/22/22	8:48	-121.273476	43.709687	1923	110.064							
5	50	6/22/22	9:27	-121.298671	43.689872	1810	125.807	Base for Western South Rim						
6	50	6/22/22	9:29	-121.298671	43.689872	1810	125.735							
7	50	6/22/22	9:31	-121.298671	43.689872	1810	125.835							
8	B1	6/22/22	9:50	-121.273476	43.709687	1923	110.029							
9	B1	6/22/22	9:54	-121.273476	43.709687	1923	110.134							
10	B1	6/22/22	10:02	-121.273476	43.709687	1923	110.103							
11	27	6/22/22	10:23	-121.293826	43.691892	1837	119.469							
12	27	6/22/22	10:24	-121.293826	43.691892	1837	119.487							
13	27	6/22/22	10:25	-121.293826	43.691892	1837	119.47							
14	26	6/22/22	10:40	-121.288281	43.694169	1894	112.292							
15	26	6/22/22	10:43	-121.288281	43.694169	1894	112.415							
16	26	6/22/22	10:45	-121.288281	43.694169	1894	112.382							

Note that this workbook contains numerous tabs, each containing one day of gravity survey data.

Newberry\_Gravity\_2022\_Final.xlsx

	A	B	C	D	E	F	G	H	I
1	Station	LON	LAT	NAD83_E	NAD83_N	NAVD88	Obs_grav	Free_air	CBA250
2	1	-121.274944	43.708130	638983.140	4840901.650	1947.000	979980.807	78.622	-122.276
3	2	-121.275278	43.706880	638959.120	4840762.260	1963.000	979977.186	80.051	-122.037
4	3	-121.275189	43.705129	638970.330	4840567.940	1980.000	979973.005	81.275	-121.766
5	4	-121.274321	43.703684	639043.610	4840408.900	1984.000	979970.224	79.859	-124.127
6	5	-121.273585	43.702412	639105.850	4840268.860	1985.000	979969.163	79.222	-124.964
7	6	-121.271200	43.699674	639304.370	4839968.770	2012.000	979963.920	82.559	-123.230
8	7	-121.270354	43.698844	639374.460	4839878.010	2021.000	979961.309	82.800	-124.250
9	8	-121.270942	43.697206	639330.870	4839695.100	2035.000	979957.997	83.957	-124.211
10	9	-121.269738	43.697206	639427.900	4839697.130	2058.000	979952.325	85.382	-123.321
11	10	-121.271676	43.708594	639245.360	4840958.670	1940.000	979983.757	79.370	-120.825
12	11	-121.269914	43.707729	639389.320	4840865.560	1938.000	979983.487	78.562	-121.401
13	12	-121.268179	43.707063	639530.650	4840794.510	1940.000	979983.418	79.170	-121.186
14	13	-121.266363	43.706468	639678.350	4840731.480	1942.000	979982.650	79.073	-120.317
15	14	-121.265118	43.705657	639780.540	4840643.510	1949.000	979980.613	79.269	-120.418
16	15	-121.262054	43.704321	640030.530	4840500.300	1967.000	979977.768	82.099	-120.702
17	16	-121.259235	43.704202	640257.940	4840491.850	1956.000	979979.108	80.055	-121.293
18	17	-121.256369	43.704112	640489.070	4840486.710	1950.000	979980.604	79.708	-121.098
19	18	-121.251784	43.704502	640857.590	4840537.800	1943.000	979980.281	77.190	-123.006
20	21	-121.278883	43.705836	638671.070	4840640.270	1917.000	979982.104	70.869	-124.783

This workbook contains a single tab containing reduced data from all stations. Column G is the average observed gravity measurement at each station (with outliers excluded), and columns H and I are the free-air anomaly and the complete Bouguer anomaly data for each station.

Within the same **MT and Gravity Data and Operations Information** folder, for the magnetotelluric survey, the **daily-reports** subfolder contains reports filed each day at the conclusion of that day's field activities, reporting on accomplishments and issues encountered and resolved. The reports contain standardized technical information about the operation of each wideband MT system such as the resistance between electrode pairs prior to installation and as installed, the self-potential between matched electrode pairs (in DCmV), the AC voltage between matched electrode pairs, which can be indicative of the quality of coupling to the ground and the general state of the electrodes as well as of proximity to 60 Hz noise sources, the serial numbers of the MT receivers and the coils, the electric dipole lengths and orientations for the two electric field channels, the inclinations of the three induction coil sensors, and the station locations are noted.

Next within the **Final Product Release**, the **MT Response Data** folder contains **MT\_Original** and **MT\_PickedForInversion** subfolders, containing EDI format files containing the MT responses (impedances and tippers) for each station. The second of these subfolders contains a subset of the impedance data, with the number of periods used in the inversions downselected for the full set of periods originally calculated as described elsewhere in this document.

Finally, the **ResolutionMatrices** folder in the **Final Product Release** contains images and .csv format files providing resolving power information for the resistivity and density models, described previously in this document.

The Data/MT\_Original folder contains the EDI files as well as the **images** subfolder that contains the plots of MT responses shown in the previous section of this report. The Data/MT\_PickedForInversion folder contains the EDI files of picked data used for inversions.

## Cloud Access to Final Electronic Data Release

The following non-expiring link has been set up on Enthalpion's Cloud Storage Server:

<https://gofile.me/74BE6/WKkUdcGIw>

This link is password protected, with password:

NREL-DEEPEN

The link provides access to the Final Electronic Data Release folder structure that authorized users are welcome to access and download.



## Archival Binary Data Available Upon Request

The links provided in the previous section of this final report provide access to the final derived data products of the NV22 survey as well as records of the field operations and geolocation information. Enthalpion Energy LLC maintains a permanent archive on its Cloud enabled, RAID Network Access Filestores of the raw, binary survey time series and related data as recorded by our MT instruments. The nature of our wideband surveys, recording 5 electric and magnetic field channels at 32-bit (4-byte) precision continuously at 1,024 samples per second for two days per station for 24 hours per day leads to necessarily large data sets.

The size of the raw binary data archive for NV22 is 337.3 GB of data.

Given the size of the binary data release, these data are not included in the **Final Product Release** folder containing this document and associated final report and data product files. Rather, the raw data are available through the following password protected link:

[hFps://gofile.me/74BE6/L17uSyiKi](https://gofile.me/74BE6/L17uSyiKi)

Password: contact [info@enthalpion.com](mailto:info@enthalpion.com) for password.

We advise end users not to download the data directly given its considerable size; rather Enthalpion Energy LLC will maintain the raw data on its secure redundant RAID network access file servers indefinitely, with access open through the link and password provided above. Enthalpion Energy LLC also maintains a library of software to read the data format and process it into the MT response files included in the final data release.

## References

Beachly, M. W., Hooft, E. E., Toomey, D. R., & Waite, G. P. (2012). Upper crustal structure of Newberry Volcano from P-wave tomography and finite difference waveform modeling. *Journal of Geophysical Research: Solid Earth*, 117(B10). <https://doi.org/10.1029/2012JB009458>.

Bowles-Martinez, E., & Schultz, A. (2020). Composition of magma and characteristics of the hydrothermal system of Newberry Volcano, Oregon, from magnetotellurics. *Geochemistry, Geophysics, Geosystems*, 21, e2019GC008831. <https://doi.org/10.1029/2019GC008831>.

Eisel, M., and G. D. Egbert (2001). On the stability of magnetotelluric transfer function estimates and the reliability of their variances, *Geophys. J. Intl.*, 144, 65-82, 2001.

Fitterman, D. V., W. D. Stanley and R. J. Bisdorf (1988). Electrical structure of Newberry Volcano, Oregon, *J. Geophys. Res.*, **93**, No. B9, 10,119-10,134.

Frone, Z. (2015). Heat flow, thermal modeling and whole rock geochemistry of Newberry Volcano, Oregon and heat flow modeling of the Appalachian Basin, West Virginia, Ph.D. Dissertation, Southern Methodist University.

Heath, B. A., Hooft, E. E. E., Toomey, D. R., and Bezada, M. J. (2015), Imaging the magmatic system of Newberry Volcano using joint active source and teleseismic tomography, *Geochem. Geophys. Geosyst.*, 16, 4433– 4448, doi:[10.1002/2015GC006129](https://doi.org/10.1002/2015GC006129).

MacLeod, N.S., Sherrod, D.R., Chitwood, L.A., and Jensen, R.A., 1995, Geologic map of Newberry Volcano, Deschutes, Klamath, and Lake Counties, Oregon: U.S. Geological Survey Miscellaneous Investigations Series Map I-2455, 2 sheets, scale 1:62,500, pamphlet, 23 p.

Leshner, C. E. and F. J. Spera, 2015. Thermodynamic and transport properties of silicate melts and magma, in *The Encyclopedia of Volcanoes*, <http://dx.doi.org/10.1016/B978-0-12-385938-9.00005-5>, published by Elsevier Inc.

Lévy, B. Gilbertt, F. Sigmundsson, Ø. G. Fløvenz, G. P. Hersir, P. Briole, P. A. Pezard, 2018. The role of smectites in the electric conductivity of active hydrothermal systems: electrical properties of core samples from Krafla volcano, Iceland, *Geophys. J. Intl.*, **215**, 3, 1558-1582, <https://doi.org/10.1093/gji/ggy342>.

Levy, L., T. Fridriksson, N. Findling, B. Lanson, B. Fraisse, N. Marino and B. Gilbert, 2020. Smectite quantification in hydrothermally altered volcanic rocks, *Geothermics*, **85**, <https://doi.org/10.1016/j.geothermics.2019.101748>.

Sowers, T. and O. S. Boyd, 2019. Petrologic and Mineral Physics Database for Use with the U.S. Geological Survey National Crustal Model: U.S. Geological Survey Open-File Report 2019-1035.

## Conclusion and Acknowledgements

The acquisition and analysis of the NV22 data set, combined with legacy MT and gravity data sets, and interpreted in combination with legacy seismic tomography and exploration well data provides new information that may lead to an improvement in our understanding of the structure of the western and southern parts of Newberry Volcano. The existing conceptual geological model for the volcano was developed over many years and in its current form also assimilated geophysical data collected under DOE support through NETL-Oregon State University-Zonge International MT and gravity monitoring surveys carried out before and during the AltaRock Energy EGS Demonstrator Project at Newberry in 2012 and 2014. That effort produced a model produced by the NETL-OSU team and released by the National Energy Technology Laboratory through the Energy Data Exchange and Geothermal Data Repository.

Consistent with that model, the existing geothermal lease unit on the west flank of the volcano was understood to sit atop a granite-bearing pluton located approximately 3 km in depth. The pluton was inferred to be a primary source of heat for EGS extraction, with the interpretation being this was likely the old volcanic center. Active and passive teleseismic tomography projects (Beachly, et al., 2012; Heath, et al., 2015) indicated that a melt body was found approximately 3-4 km beneath the caldera. While a low velocity zone at depth was also seen beneath the south rim and flank of the volcano, it was on the margins of resolvability in the Beachly, et al. study, and in both studies most of the interest was in the sub-caldera area.

Prior to the present NV22 survey, the 3-D resistivity model developed by inversion of legacy MT data and data collected by Oregon State University and Zonge International in 2012 and 2014 did not show a significant resistivity anomaly at depths below the caldera corresponding to the putative melt zone. It was inferred that either there was little interconnected melt (seemingly in opposition to the seismic interpretation), or that if there was interconnected melt it was likely dry and rhyolitic, yielding no significant resistivity contrast with the host rock. In contrast to the sub-caldera zone, the 3-D resistivity model suggested there was a highly conductive zone that shallowed near the Big Obsidian Flow along the southern caldera rim area, and that deepened to depths similar to those at the inferred melt zone below the caldera, i.e. to approximately 3 km. As the conductive zone deepened, rather than connecting with the seismic low velocity zone beneath the caldera to the north of the Big Obsidian Flow, it appeared to deepen to the south to the south flank of the volcano.

The single and joint inversions of the augmented legacy and NV22 wideband MT and gravity data sets has sharpened our focus on the south rim and flank anomaly. While we see an electrically conductive zone beneath the shallow region beneath the caldera, which we attribute to caldera in-fill and hydrothermal processes, as before we do not see a conducting anomaly at depth beneath the caldera that corresponds to the seismic low velocity zone. Rather, we see a well-defined, highly conductive feature that shallows immediately adjacent to the Big Obsidian Flow, and that deepens to the south that does not appear to connect with the seismic feature beneath the caldera.

This low-resistivity feature corresponds closely with the footprint of a seismic low velocity feature seen in Beachley, et al. (2012) and in Heath, et al. (2015), as well as a low-density feature of the same footprint. The proximity of this feature to the GEO N-1 well, which shows evidence for the existence of a hydrothermal system approximately 1 km below the well head, with high-temperature hydrothermal mineral alteration products ubiquitous in the lower well section, reinforces the view that the south rim/flank feature may represent a potential geothermal play.

Several km to the south near the edge of our survey array, roughly along and adjacent to the trace of the deep crustal Walker Rim Fault, another highly conductive, low relative density feature is seen that in the 3-D inversion models appears to have a connection with the south rim/flank low resistivity, low relative density, low seismic velocity feature. Examination of surface geology including the location of faults, the distribution of lava flows and of volcanic vents supports the view that the south rim/flank feature may have a connection to a recently active volcanic system to the south. This poses the question – has the current volcanic center of the volcano migrated south of the caldera and is it currently beneath the south rim or south flank? Further work is needed to resolve this question.

Enthalpion Energy LLC recognizes the vital contributions of the NV22 field crew, comprised of independent contractors, service providers and NREL staff and interns. We thank Amanda Kolker at NREL for leading the project, supported by Hannah Pauling (NREL) and Rachel King (NREL Intern) for the hard work in the field and for the post-survey interpretation effort. Adam Schultz oversaw and coordinated the project for Enthalpion Energy, as well as participating in the initial stage of fieldwork. Esteban Bowles-Martinez led the MT field program with support from Taylor Viti and Xiaolei Tu and the participation of the NREL personnel. Alain Bonneville designed the gravity survey, led the initial phase of gravity fieldwork supported by and continued to completion by the other crew members, and he carried out the gravity data reduction to the Complete Bouguer Anomaly. Xiaolei Tu carried out the post data reduction analysis and inversion of the gravity data, as well as the inversion of the MT data, and he devised the joint inversion code for 3-D density and electrical resistivity structure. Enthalpion subcontractor Brady Fry provided assistance with algorithm support and database management.